Design and Experimental Evaluation of Robust Controllers for Electro-Hydraulic Actuators

by

Navid Niksefat

A thesis

presented to the University of Manitoba

in fulfillment of the

thesis requirement for the degree of

Doctor of Philosophy

in

Mechanical and Industrial Engineering

Winnipeg, Manitoba, Canada, 2002

THE UNIVERSITY OF MANITOBA

FACULTY OF GRADUATE STUDIES

*****

COPYRIGHT PERMISSION PAGE

DESIGN AND EXPERIMENTAL EVALUATION OF ROBUST CONTROLLERS FOR ELECTRO-HYDRAULIC ACTUATORS

BY

NAVID NIKSEFAT

A Thesis/Practicum submitted to the Faculty of Graduate Studies of The University

of Manitoba in partial fulfillment of the requirements of the degree

of

DOCTOR OF PHILOSOPHY

Abstract

This thesis presents the design and experimental evaluation of robust controllers for an electrohydraulic actuator that operates under significant system uncertainties and nonlinearities. The designed controllers allow the actuator (*i*) to follow a free space trajectory (motion control), (*ii*) to exert a desired force while in contact with an uncertain environment (force control), and (*iii*) to pass through the transition phase from free space to constrained space successfully and stably exert force on the environment (contact task control).

Firstly, a robust force controller is designed using linear and nonlinear approaches within the framework of Quantitative Feedback Theory (QFT). In the linear approach, the effects of nonlinearities and uncertainties, such as environmental stiffness and operating points, are accounted for by describing the linearized model parameters as structured uncertainties. The nonlinear approach is based on linear time-invariant equivalent models of the system that can precisely represent the nonlinear plant over a wide range of operation. The equivalent models can be generated by the nonlinear mathematical equations of the hydraulic actuator, or be obtained directly from input-output measurements of the actual system. Given the equivalent models/linearized model, a controller is designed to satisfy *a priori* specified stability, tracking and disturbance rejection specifications.

Secondly, the nonlinear QFT approach is used to design an explicit position controller to regulate the actuator in free space.

Finally, for contact task control, a simple switching condition is proposed based on robust position and force controllers, to make the transition from free space to a

constrained one. The stability of the contact controller is shown using an extended version of Lyapunov's second method under the condition of existence and uniqueness of Filippov's solution.

The developed controllers enjoy the simplicity of fixed-gain controllers, are easy to implement, and at the same time are robust to the variation of hydraulic functions as well as environmental stiffness. Numerous experimental tests are performed on an industrial hydraulic actuator equipped with a servovalve and include motion through free space, contact with the environment and the transition between the two.

Acknowledgements

I would like to thank all of those who have supported me throughout the course of this project. Without their time and effort, this endeavor would not have been possible.

First of all, I would like to express my sincere thanks and appreciation to my supervisor, Dr. Nariman Sepehri, for guidance, and for providing me with excellent facilities to pursue my work, and for ensuring financial support throughout my studies. His help, stimulating suggestions and encouragement helped me in all the time of research and writing of this thesis.

My appreciation goes to other members of my PhD committee who monitored my work and took effort in reading and providing me with valuable comments on earlier versions of this thesis: Dr. Subramaniam Balakrishnan, Dr. Waldemar H. Lehn and Dr. Christine Wu. I would particularly like to thank Dr. Wu for many of her relevant advice and steady discussions on the theoretical aspects of Chapter 6 of this thesis. Thanks also to external member of the thesis examination committee: Dr. Clarence W. de Silva of the University of British Columbia.

I would like to thank several of my friends for helping with the preparation of this thesis. Dr. Amir Ali-Akbar-Khayyat, who provided me with crucial support during my first years. I am grateful to my friend Kamyar Ziaei for helping me with experimental setup and general advice. I would also like to thank Pooya Sekhavat who has been a great company and assisted me with several tasks in the preparation of the thesis.

In addition, I am grateful to Rob Rostecki for proofreading this manuscript. I am also thankful to Al Lohse who provided technical assistance during the control implementation and experiments throughout the course of this research.

The grant provided by the Natural Sciences and Engineering Research Council of Canada (NSERC), and the fellowship awarded by the University of Manitoba, were instrumental in the success of my studies.

I also wish to thank my parents for their love and encouragement, without whom I would never have enjoyed so many opportunities. I am also indebted to my uncle, Dr. Ali Hariri, for his moral support especially during my stay in Canada.

At last, thank God for the wisdom and perseverance that he has been bestowed upon me during this research project, and indeed, throughout my life.

Table of Contents

Abstract ii

Acknowledgments iv

Table of Contents vi

List of Figures ix

List of Tables xii

Nomenclature xiii

Chapter 1

Introduction 1

1.1 Preliminary Remarks 1

1.2 Relevant Background 3

1.2.1 Contact Task Control 3

1.2.2 Force and Motion Control in Hydraulic Systems 4

1.3 Objectives and Scope of this Thesis 7

Chapter 2

Description of Hydraulic Actuator 9

2.1 Experimental Test Station 9

2.2 Modeling 12

2.2.1 Actuator Dynamic Equations 12

2.2.2 Servovalve Flow and Dynamic Equations 16

2.2.3 Cylinder Flow Equations 19

Chapter 3

Controller Design Using Quantitative Feedback Theory 21

3.1 QFT Configuration 22

3.2 QFT Design Problem 23

3.3 QFT Design Procedure 26

Chapter 4

Design of the QFT Force Controller 28

4.1 Linear Approach 29

4.1.1 Linearized Model 29

4.1.2 Controller Synthesis 35

4.1.3 Experimental Results 41

4.2 Nonlinear Approach 45

4.2.1 Controller Design 46

4.2.2 Derivation of Linear Time-Invariant Equivalent Models 49

4.2.3 Controller Synthesis 59

4.2.4 Experimental Results 63

4.3 Summary and Comparison 64

Chapter 5

Design of the QFT Position Controller 72

5.1 Derivation of the Linear Time-Invariant Equivalent Models 72

5.2 Controller Design 78

5.3 Experimental Results 83

Chapter 6

QFT Contact Task Controller **89**

6.1 Construction of the Contact Controller **89**

6.2 Stability Analysis of the Contact Controller **91**

6.2.1 State Space Equations 92

6.2.2 Existence, Continuity and Uniqueness of Filippov's Solution 95

6.2.3 Stability Proof 98

6.3 Experimental Results **101**

Chapter 7

Concluding Remarks **107**

References **112**

List of Figures

Fig. 2.1 Experimental test station 10

Fig. 2.2 Schematic diagram of the experimental test station 11

Fig. 2.3 Schematic of the hydraulic actuator interacting with the environment 13

Fig. 2.4 Steady-state piston velocity versus input current 14

Fig. 2.5 Experimental and simulation plots of friction force versus piston velocity 15

Fig. 2.6 Frequency response for two-stage servovalve 18

Fig. 2.7 Valve orifice area versus input current 19

Fig. 2.8 Drop in supply pressure caused by a sinusoidal input 20

Fig. 3.1 Diagram of a two-degree-of-freedom QFT control system 22

Fig. 3.2 Typical frequency and time domain tracking bounds 25

Fig. 3.3 Typical bounds and nominal loop function in Nichols chart 27

Fig. 4.1 Bode plot of open-loop transfer functions 34

Fig. 4.2 QFT bounds on Nichols chart with: **(a)** uncompensated plant; **(b)** nominal loop 38

Fig. 4.3 Closed-loop frequency responses over range of parametric uncertainty: **(a)** without prefilter; **(b)** with prefilter 39

Fig. 4.4 System responses over range of parametric uncertainty: **(a)** step input; **(b)** step disturbance 40

Fig. 4.5 Step force responses with different environmental stiffnesses 42

Fig. 4.6 Pump pressure pertaining to experiment in Fig. 4.5 42

Fig. 4.7 Step force responses for different reference forces 43

Fig. 4.8 Step force responses for different supply pressures 43

Fig. 4.9 Control signal pertaining to experiment in Fig. 4.8 44

Fig. 4.10 Two-degree-of-freedom QFT control system 46

Fig. 4.11 Experimental input-output responses 51

Fig. 4.12 Plant frequency responses obtained from experimental approach 52

Fig. 4.13 Acceptable plant input-output histories 53

Fig. 4.14 Plant frequency responses obtained from model-based approach 57
Fig. 4.15 Acceptable responses for disturbance rejection 57
Fig. 4.16 QFT bounds on Nichols chart and nominal loop 61
Fig. 4.17 Closed-loop frequency responses over a range of parameter uncertainties ... 61
Fig. 4.18 Closed-loop disturbance transfer function and bound, D_2 62
Fig. 4.19 Closed-loop disturbance transfer function and bound, D_1 62
Fig. 4.20 Step responses with different environmental stiffnesses 66
Fig. 4.21 Actuator position pertaining to experiment in Fig. 4.20 66
Fig. 4.22 Control signal pertaining to experiment in Fig. 4.20 67
Fig. 4.23 Step force responses for different reference forces 67
Fig. 4.24 Step force responses for different supply pressures 68
Fig. 4.25 Control signal pertaining to experiment in Fig. 4.24 68
Fig. 4.26 Repeatability test 69
Fig. 4.27 Control signal pertaining to experiment in Fig. 4.26 69
Fig. 4.28 System response to square wave force set-point 70
Fig. 4.29 Control signal pertaining to experiment in Fig. 4.28 70
Fig. 4.30 Bode plots of the designed controllers 71

Fig. 5.1 Acceptable plant input-output histories for position controller design 75
Fig. 5.2 Plant frequency domain responses 76
Fig. 5.3 QFT bounds on Nichols chart and nominal loop 81
Fig. 5.4 Closed-loop frequency responses over range of parameter uncertainties 81
Fig. 5.5 Closed-loop disturbance transfer function and bound, D_2 82
Fig. 5.6 Closed-loop disturbance transfer function and bound, D_1 82
Fig. 5.7 Step response of QFT position controller 84
Fig. 5.8 Actuator velocity pertaining to experiment in Fig. 5.7 84
Fig. 5.9 Control signal pertaining to experiment in Fig. 5.7 85
Fig. 5.10 Pump pressure pertaining to experiment in Fig. 5.7 85
Fig. 5.11 Step responses with different command inputs 86
Fig. 5.12 Step responses when pump pressure variations exist 86
Fig. 5.13 Control signal pertaining to experiment in Fig. 5.12 87

Fig. 5.14 System response under disturbance load 87
Fig. 5.15 Disturbance force pertaining to experiment in Fig. 5.14 88
Fig. 5.16 Control signal pertaining to experiment in Fig. 5.14 88

Fig. 6.1 Block diagram of QFT contact controller 91
Fig. 6.2 Contact response: **(a)** force; **(b)** position; **(c)** velocity; **(d)** control signal 103
Fig. 6.3 Contact response (high stiffness): **(a)** force: **(b)** position 105
Fig. 6.4 Multi-step contact response test: **(a)** force; **(b)** position 106

List of Tables

Table 4.1: Operating values and parameter ranges pertaining to the linear transfer function 34
Table 4.2: Operating values and parameter ranges pertaining to the nonlinear model ...55

Table 5.1: Operating values and parameter ranges 76

Table 6.1: Controller set-point adjustment in a multi-step contact response test 102

Nomenclature

Variables

Δ	servovalve orifice area (m^2)
f_f	actuator dry friction force (N)
f_d	external force on actuator (N)
i	servovalve input current (A)
p_i, p_o	line pressures (Pa)-(psi)
q_i, q_o	control flows (m^3/sec)
τ_f	servovalve flapper torque (Nm)
u	input signal to the servovalve (V)
V_i, V_o	trapped fluid volumes at the sides of actuator (m^3)
x	actuator displacement (m)
x_f	servovalve flapper displacement (m)
x_s	sensor displacement (m)
x_{sp}	servovalve spool displacement (m)

Parameters

A_i, A_o	piston effective areas (m^2)
A_{sp}	servovalve spool area (m^2)
β	effective bulk modulus (Pa)
c_d	servovalve coefficient of discharge
d	actuator damping coefficient (Nsec/m)
d_e	environment damping coefficient (Nsec/m)
d_s	sensor damping coefficient (Nsec/m)
f_c	Coulomb friction (N)
f_s	actuator stiction force (N)
k_2	hydraulic amplifier flow gain (m^2/sec)
k_a	servovalve power amplifier gain (V/A)
k_e	environment stiffness (N/m)
k_f	servovalve flapper stiffness (Nm/m)
k_l	servovalve torque motor current gain (Nm/A)
k_s	sensor stiffness (N/m)
k_w	servovalve feedback wire stiffness (Nm/m)
K_p^i, K_p^o	servovalve pressure gains (m^3/Pa·sec)
K_s^i, K_s^o	servovalve flow gains (m^2/sec)
m_a	total mass of actuator piston and rod (kg)
m_e	mass of environment (kg)

ω_n	servovalve natural frequency (Hz)
p_e	return pressure (Pa)-(psi)
p_s	supply pressure (Pa)-(psi)
ξ	servovalve flapper damping ratio
ρ	hydraulic fluid density (kg/m^3)
V	cylinder volume (m^3)
$\overline{V}_i$, $\overline{V}_o$	initial fluid volumes at the sides of actuator (m^3)
w	servovalve orifice area gradient (m^2/m)
x^*	initial location of environment (m)

Chapter 1

Introduction

1.1 Preliminary Remarks

Hydraulic actuators are potential choices for many industries due to their stiffness, compactness and high payload capacity. These features make them appropriate for high power industrial equipment such as machine tools, aircrafts, material handling devices, construction, mining and agricultural machines. Hydraulic actuators are able to maintain their loading capacity indefinitely, something that would usually cause excessive heat generation in electrical components (Alleyne, 1996). They are also advantageous for applications requiring environmental interactions because of their high force-to-weight ratio and fast response time. However, the utilization of hydraulic actuators interacting with an environment presents many difficulties to overcome.

Firstly, they have a relatively high degree of nonlinearity (as compared to other systems like DC servo motors) resulting from servovalve flow-pressure characteristics,

unequal piston cross-sectional areas acting in the two directions of motion, orifice area openings and, in part, to the variations of fluid volume under compression.

Secondly, hydraulic systems contain a large extent of model uncertainties (Yao et al., 1999). For example, the supply pump pressure is subject to variation that may be generated by the operation of other actuators in a multi-user environment (Pannett et al., 1999). The flow and pressure coefficients, characterizing fluid flow into and out of the valve, are functions of load and supply pressure and could vary under different operating conditions (Watton, 1990). Also, the effective bulk modulus in hydraulic systems could significantly change under various load conditions, oil temperature and air content in the hydraulic fluid (Yu et al., 1994).

Thirdly, unlike electrical actuators, force control of hydraulic actuators is a difficult problem. In a hydraulic actuator, the control signal acts to activate a spool valve that controls the flow of hydraulic fluid into and out of the actuator. This flow in turn causes a pressure differential build-up that is proportional to the actuator force/torque. Even if the spool valve dynamics are ignored, the control signal fundamentally controls the derivative of the actuator force and not force itself (Heinrichs et al., 1997). Finally, the force control problem becomes more challenging when the actuator task also includes contact. A contact task is generally defined as the ability of the actuator to follow a free space trajectory and then make and maintain contact with the environment for exerting a desired force. Usually, stability is a crucial issue, especially during the inevitable phase transition. The natural elasticity of impact or the response of the controller to the transient can cause the manipulator to rebound from the environment and may drive the manipulator into instability (Volpe and Khosla, 1993).

1.2 Relevant Background

In this section some recent works on the development of methods for force and motion control for hydraulic actuators are presented.

1.2.1 Contact Task Control

Various initiatives have been focused on the development of control laws, which can result in a stable controller for manipulators during the transition from free motion to constrained motion. Some strategies, like impedance control, use a unified control structure for both free and constrained motion (Mason, 1981; Hogan, 1987). These approaches, however, show good performance only under restrictive assumptions such as an accurate model of the environment, or the maintenance of contact after impact. Stability is also a major problem and has not yet been clearly addressed (Wu et al., 1996). Poor performance of these approaches can be attributed to some degree to use of a unified control law in spite of high changes of the system dynamics due to contact. Therefore, it seems attractive to use different control laws for different phases of motion to get the best possible performance from the system. Other methodologies use different controller structures or a controller with different gains to cope with different phases. In these methods, the discontinuities arising from the control law switching and/or changes of the system dynamics due to contact are major issues in their stability analysis. For example, Mills and Lokhorst (1993) proposed a discontinuous controller and discussed its performance based on the notion of the generalized dynamical system. A practical approach for controlling the contact transition was also proposed by Payandeh (1996). The gains of the controller are switched during different phases of motion to achieve stable contact force regulation. Marth et al. (1993) proposed a model based algorithm

combined with an explicit force controller for regulating the phase transition. The force controller is switched on when contact is established.

In all the literature reviewed so far, the actuator dynamics were assumed to be ideal and capable of producing the necessary force instantaneously, or the controller law was derived assuming an electrical actuator. No published work exists, prior to this work, that includes contact task control for hydraulic actuators.

1.2.2 Force and Motion Control in Hydraulic Systems

In the literature several motion control strategies can be found for hydraulic actuators. To name a few, Vossoughi and Donath (1992) formulated a feedback linearization method for the control of a single-rod electrohydraulic actuator. The dynamic model of the system was inverted to cancel the system's nonlinearities. The method, however, relies on measurements of at least the load's position, velocity and the hydraulic line pressures. This makes their method not suitable for industrial implementation due to its complexity. Yao et al. (1999) applied adaptive robust control to improve the performance of hydraulic positioning systems. They took into account some nonlinearities and model uncertainties such as inertial load and friction of the electrohydraulic system and designed a discontinuous projection-based adaptive controller. The experimental results showed that the controller could reduce tracking errors as compared to a PID feedback controller with velocity and acceleration feedforward terms. Ziaei and Sepehri (2001) implemented an indirect model reference adaptive (MRA) control scheme for the positioning of hydraulic actuators that operate low-cost proportional valves. The robustness of the parameter adaptation is achieved by employing the recursive least-square algorithm in combination with dead-zone in the adaptive law. A more

computationally efficient method, time delay control, was applied by Chin et al. (1994) for the positioning of an electrohydraulic servo system under external disturbances. The experimental results showed that the time delay controller is robust to inertia variations, external loads as well as the level and type of command inputs.

Robust control methodologies are also used for control of hydraulic systems. Pachter et al. (1997) designed a QFT controller for an electrohydrostatic actuator as part of a flight control system. The QFT controller nominally was able to track the unit step command even in the presence of random sensor noise. Thompson and Kremer (1997) developed a QFT controller for a variable displacement pump system based on a linearized model with parametric uncertainty. The closed-loop frequency domain specifications were satisfied, and the corresponding step responses were found to be reasonable. The validity of the controller was shown through simulations. An overview of QFT method will be presented in the chapter 3 of this thesis.

Regarding force control of hydraulic actuators, there is a relatively scarce amount of research results presented in the literature. Conrad and Jensen (1987) used combinations of velocity feedforward, control signal feedback and a Luenberger observer with state estimate feedback for the force control of a double-rod hydraulic actuator. The simulation and experimental results, for a constant set-point force, showed over-performance of the proposed method over conventional (P or PI) force feedback controllers. However, the variations of load and supply pressures were not considered in their study. Chen et al. (1990) designed a sliding mode controller for a single-rod hydraulic actuator interacting with a spring as an environment. Using position, velocity, acceleration, force and pressure feedbacks, the variable structure controller proved to be capable in both static

and dynamic force control tasks. The effect of servo-amplifier gain variation was also examined; however, the variation of environmental stiffness was overlooked in their study. Sun et al. (1999) employed a sliding mode controller with a perturbation observer for a single-rod electrohydraulic system. The effect of cylinder position and velocity on the pressure dynamics was considered as perturbation to the control model, which was estimated by the observer. Experimental results verified improved steady-state and transient performances as compared with traditional PID controllers.

Adaptive control strategies have also been considered for hydraulic force control. Liu and Alleyne (1999) developed a switching control scheme using a Lyapunov-based adaptive law to reduce parametric uncertainties. The implementation of the controller, which was based on the measurements of position, velocity, acceleration, pressure and spool displacement, showed good performance for force/pressure high frequency tracking. Wu et al. (1998) applied a generalized predictive control algorithm to a hydraulic force control system. The controller was experimentally evaluated for various environmental stiffnesses and set-points. The method, however, relies heavily on on-line parameter estimation and consequently demands large computational time. Ziaei and Sepehri (2001) proposed an adaptive controller that handles hydraulic valve nonlinearities by incorporating a simple Hammerstein model. Laval et al. (1996) used an H_∞ approach to robustly control the force exerted by a double-acting symmetric hydraulic cylinder with a servovalve. The importance of uncertainties in the environment, measurement noise and nonlinearities on the performance of hydraulic force control system were highlighted. Limited test results, demonstrating the achievement of a stability/performance trade-off when utilizing an H_∞ approach, were presented.

Even though a great number of force control concepts, methods and algorithms have been developed, there is still a big gap between theory and industrial practice. The reasons have been ascribed to the poor industrial control architecture, which does not allow the implementation of sophisticated algorithms. Furthermore, no comprehensive control algorithm dealing with a wide range of uncertainties in hydraulic systems exists.

1.3 Objectives and Scope of this Thesis

The general objective of this research is to contribute to the development of appropriate controls for industrial hydraulic manipulators interacting with uncertain environments. Examples of such manipulators are hydraulic robots used in under-water exploration/inspection and excavators used in mining and construction. The demanding performance specifications for these applications have motivated researchers to examine how to improve controllers applied to hydraulic actuators.

More specifically, the goal of this research is to design a robust controller for a hydraulic actuator to regulate a reference position and a reference force in free space and constrained environment, respectively, and guarantee stability, particularly during the transition phase from free space to constrained environment. The designed controller is expected to satisfy the following requirements:

(*i*) be of low-order and easy to implement.

(*ii*) be able to deal with the nonlinear characteristics of a rugged hydraulic actuator.

(*iii*) be able to maintain satisfactory performance despite system variations including up to 300% in environmental stiffness, 300% in pump pressure increase and 100% in reference inputs.

The quantitative feedback theory (QFT) technique is considered in this research for designing a robust controller. The QFT technique is a frequency domain method for control design of systems with large plant uncertainties and performance specifications. QFT is applicable to both linear and nonlinear systems. Part of the objective of this thesis is to, for the first time, evaluate and document the application of the QFT technique to contact tasks control of hydraulic systems especially during force control task.

Chapter 2

Description of Hydraulic Actuator

2.1 Experimental Test Station

An experimental test rig was designed and constructed at the Experimental Robotics and Teleoperation Laboratory, the University of Manitoba, for contact investigation in hydraulic actuators. The stiff structure of the test rig allows for large contact force experimentation with high accuracy. The test rig is instrumented with different sensors for the measurement of hydraulic pressure, actuator position and actuator ram force. With reference to Figs. 2.1 and 2.2, the test rig, on which all the experiments have been performed, consists of a hydraulic power unit, a hydraulic cylinder, a Moog A076-585 servovalve and a 586/350 personal computer. A hydrodynamic, internal-tooth gear pump, immersed in hydraulic fluid in the reservoir, provides hydraulic fluid at a rate of 5 gallons per minute (19 L/min) under 3000 psi. The pump is driven through a direct-drive, flexible coupling by a 10 hp electric motor. The output pressure is adjustable from 100 to

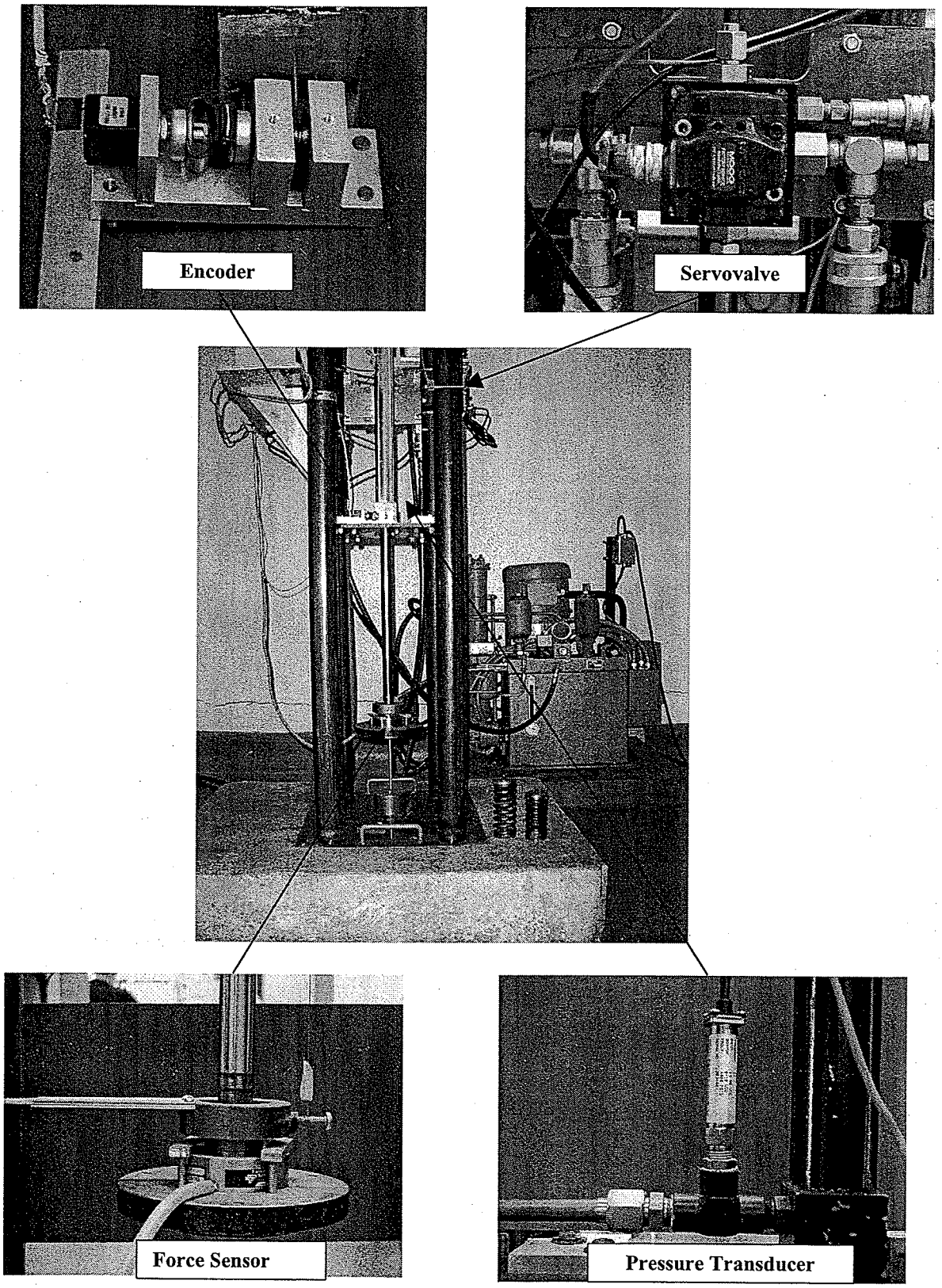

Fig. 2.1: Experimental test station.

3000 psi through an adjustable relief valve mounted on the pump manifold. The Moog two-stage servovalve, with a maximum flow of 5 gpm (19 L/min) at 1000 psi, controls the oil flow from the hydraulic supply unit to the hydraulic cylinder. The output stage of the servovalve is a closed center, four-way sliding spool. The pilot stage is a symmetrical double air gap dry torque motor. Mechanical feedback of spool position is provided by a cantilever spring. The valve operated within the range of ±3 V input signal and has a dead-band of ~0.05 V within which the actuator does not move. The cylinder of the actuator (with annulus area of 1140 mm^2) is fixed on a frame and the ram (with area of

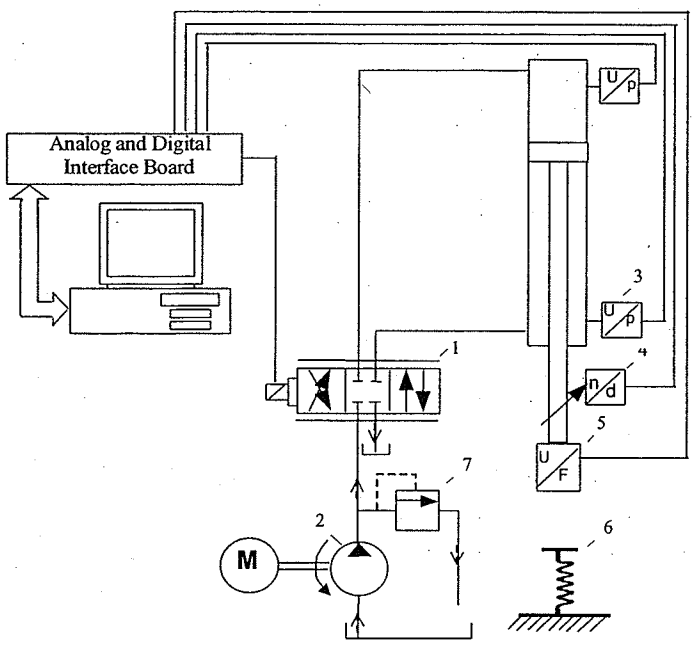

1- Servovalve	5- Force Sensor
2- Pump with Pressure Regulator	6- Environment
3- Pressure Transducer	7- Relief Valve
4- Incremental Encoder	

Fig. 2.2: Schematic diagram of the experimental test station.

630 mm^2) is equipped with a force transducer and an optical encoder position transducer with a resolution of ~40 counts per millimeter. The force transducer has a capacity of 45 kN and is fixed onto the end of the cylinder. The 12 bit analog-to-digital conversion allows a force resolution of 10 N when the full range is used. The hydraulic system is instrumented with three pressure transducers to measure supply, extend and retract pressures. The computer is equipped with a Metrabyte M5312 quadrature encoder counter card and a DAS-16 data acquisition card. The DAS-16 card is used for analog-to-digital conversion of the analog transducer signals (force and pressure transducers). It is also used to supply the servovalve with a control signal through its digital-to-analog outputs. Springs are used to represent the environment; replacing the spring changes the stiffness of the environment.

2.2 Modeling

In this section the mathematical model for a hydraulic actuator interacting with the environment is derived. This model will be used later for controller design. Here, the well-known model of manipulator-sensor-environment by Volpe and Khosla (1990) is coupled with the nonlinear hydraulic actuator dynamics.

2.2.1 Actuator Dynamic Equations

With reference to Fig 2.3, the force sensor, with stiffness k_s and damping d_s, is attached to the actuator piston, represented by the mass m_a. The environment is represented by mass m_e, damping d_e and stiffness k_e. The dynamic equations describing the dynamics of this system are:

$$m_a\ddot{x} + d\dot{x} = p_i A_i - p_o A_o - f - f_d \tag{2.1}$$

$$f = k_s(x - x_s) + d_s(\dot{x} - \dot{x}_s) \tag{2.2}$$

$$f = \begin{cases} 0 & \text{Non - Contact} \\ m_e\ddot{x}_s + d_e\dot{x}_s + k_e(x_s - x^*) & \text{Contact} \end{cases} \tag{2.3}$$

where x, x_s and x^* are the actuator displacement, sensor displacement and the initial location of the environment with respect to the actuator, respectively. d is the equivalent

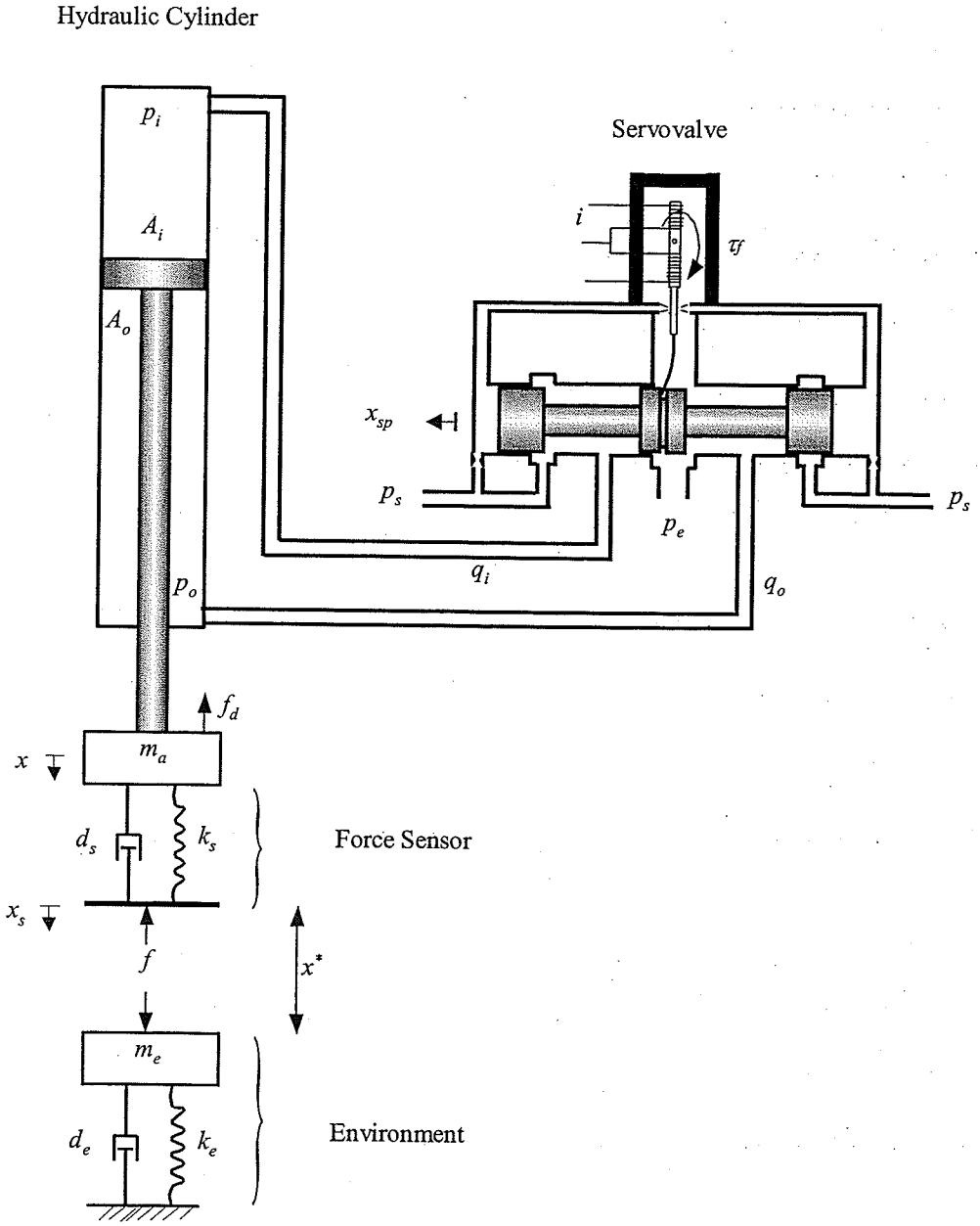

Fig. 2.3: Schematic of the hydraulic actuator interacting with the environment.

viscous damping coefficient of hydraulic actuator. A_i and A_o are the effective piston areas. p_i and p_o are the input and output line pressures, respectively. f_d is the external force on the actuator including gravitational force, $m_a g$, and dry friction, f_f, which combines two major effects namely Coulomb friction and stiction.

Experiments were conducted to study the friction force in the hydraulic actuator. With the actuator not in contact with the environment, the actuator was run at various velocities and the steady-state velocities were computed off-line by differentiating the measurements obtained from the linear displacement transducer. The plot of the actuator velocity versus input signal is shown in Fig. 2.4. The friction force was calculated from the following equation, which represents the dynamics of the actuator moving at a constant velocity in free space,

$$Friction\ Force = f_f + d\dot{x} = p_i A_i - p_o A_o + m_a g \tag{2.4}$$

As is shown in Fig. 2.5, the friction is particularly noticeable at low velocities, and

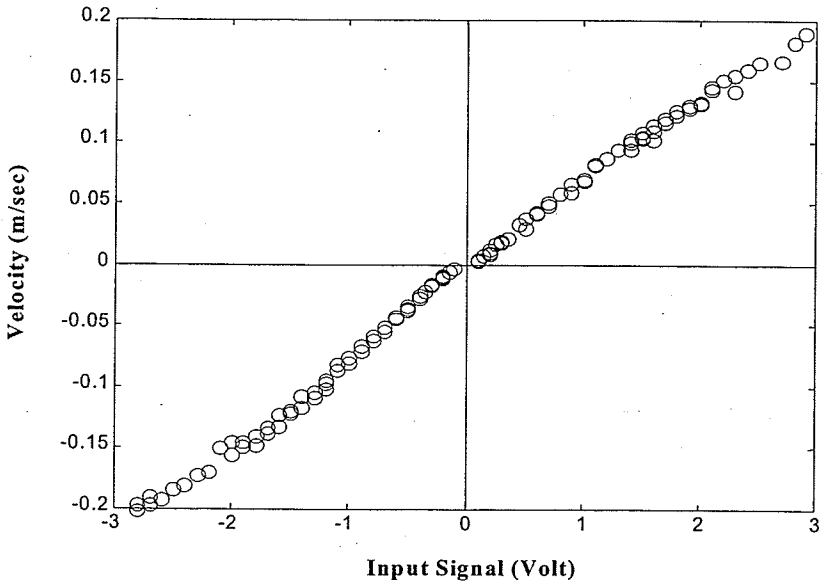

Fig. 2.4: Steady-state piston velocity versus input current.

then smoothly descends when the piston velocity increases. A Tustin model for friction has been used by Laval et al. (1996) for friction identification in hydraulic actuators. The model is expressed as:

$$Friction\ Force = [f_c + f_s e^{-C_l|\dot{x}|}]sign(\dot{x}) + d\dot{x} \tag{2.5}$$

where

$$sign(\dot{x}) = \begin{cases} 1 & \dot{x} > 0 \\ \alpha & \dot{x} = 0, \quad \text{where} \quad -1 < \alpha < 1 \\ -1 & \dot{x} < 0 \end{cases}$$

f_c denotes the Coulomb friction assumed to be constant (invariant with pressure), f_s defines the stiction force and C_l is the lubrication coefficient. The identification of these model parameters (f_c, f_s, d and C_l) were performed using a Recursive Least Mean Square identification with Matlab software. The coefficients were determined numerically and the friction estimate based on the Tustin model is shown in Fig. 2.5. As is seen from the

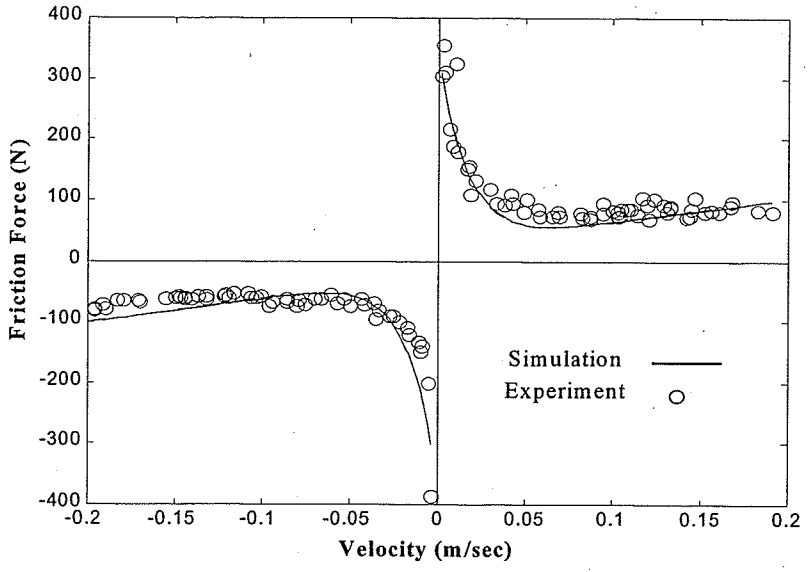

Fig. 2.5: Experimental and simulation plots of friction force versus piston velocity.

results, the parameter estimation (f_c=23 N, f_s=327 N, d=400 N/(m/sec), C_l=60 1/(m/sec)) and the choice of the mathematical model is emphasized by good comparisons between experimental and simulation results.

2.2.2 Servovalve Flow and Dynamic Equations

The servovalve is a typical two-stage type with force feedback. An input current to the torque motor causes the flapper to change its position. This results in a pressure differential across the spool forcing it to move from the center position between the two nozzles. This displacement causes a pressure difference between the two ends of a spool valve. The pressure difference provides a force on the spool, which causes it to change its displacement. A cantilever leaf spring provides a force feedback on the flapper as a function of spool position.

The relationship between the input current and the spool position of the servovalve is now derived. The resultant torque on the flapper is given by Watton (1989) and FitzSimons and Palazzolo (1996),

$$k_I i - k_w x_{sp} = \tau_f \tag{2.6}$$

where i is the current, k_I is the torque motor current gain, k_w is the feedback wire stiffness, x_{sp} is the spool displacement, and τ_f is the resultant flapper torque. The equation of motion for the flapper can be written in the following form:

$$\ddot{x}_f + 2\xi\omega_n\dot{x}_f + \omega_n^2 x_f = \frac{\omega_n^2}{k_f}\tau_f \tag{2.7}$$

where k_f is the net stiffness of the flapper, x_f is the displacement of the flapper, ω_n is the natural frequency of the flapper, and ξ is the damping ratio of the flapper. The

relationship between the position of the flapper and the velocity of the spool is defined by,

$$k_2 x_f = A_{sp}\dot{x}_{sp} \tag{2.8}$$

where A_{sp} is the spool end area and k_2 is the hydraulic amplifier flow gain.

Equations (2.6), (2.7) and (2.8) are combined in the Laplace domain to determine the transfer function between the spool position and the input current. The resulting transfer function is

$$\frac{X_{sp}(s)}{I(s)} = \frac{\dfrac{k_1 k_2}{k_f A_{sp}}}{s\left(\dfrac{s^2}{\omega_n^2} + \dfrac{2\xi}{\omega_n}s + 1\right) + \dfrac{k_1 k_w}{k_f A_{sp}}} \tag{2.9}$$

The third order system given by (2.9) gives a very good representation of the actual valve up to very high frequencies. However, the high frequency dynamics of the servovalve can be ignored in a reduced order model, provided the desired closed loop bandwidth is low enough. Experimental and simulation studies have revealed that the real pole of the two-stage servovalve model dominates the servovalve response and can be used as an approximation of the servovalve dynamics (Alleyne, 1996; Merritt, 1967, pp. 212-217). The experimental result of frequency response of the servovalve under consideration (courtesy of Moog Inc.) is shown in Fig. 2.6. The result verifies that the first order model gives a very good approximation of the actual valve up to frequencies of approximately 200 rad/sec. Therefore, the reduced-order model is a first order system with the same real pole and low frequency gain as the third order model, as follows,

$$\frac{X_{sp}(s)}{I(s)} = \frac{k_2 / k_w}{(1+\tau s)}. \tag{2.10}$$

Adding the power amplifier gain, the transfer function relating the spool displacement to the control voltage can be written as:

$$\frac{X_{sp}(s)}{U(s)} = \frac{k_{sp}}{(1+\tau s)} \tag{2.11}$$

where U is the control voltage and $k_{sp}=k_a k_2/k_w$, where k_a is the power amplifier gain.

The governing nonlinear equations that describe the fluid flow distribution in the valve can be written as (Merritt, 1967):

for extension ($x_{sp} \geq 0$)

$$q_i = c_d \Delta(x_{sp}) \sqrt{\frac{2}{\rho}(p_s - p_i)} \qquad q_o = c_d \Delta(x_{sp}) \sqrt{\frac{2}{\rho}(p_o - p_e)} \tag{2.12a}$$

for retraction ($x_{sp} < 0$)

$$q_i = c_d \Delta(x_{sp}) \sqrt{\frac{2}{\rho}(p_i - p_e)} \qquad q_o = c_d \Delta(x_{sp}) \sqrt{\frac{2}{\rho}(p_s - p_o)} \tag{2.12b}$$

where q_i and q_o represent fluid flows into and out of the valve, respectively. c_d is the orifice coefficient of the discharge, ρ is the mass density of the fluid, p_s is the pump pressure and p_e is the return (exit) pressure. $\Delta(x_{sp})$ represents the relationship between the

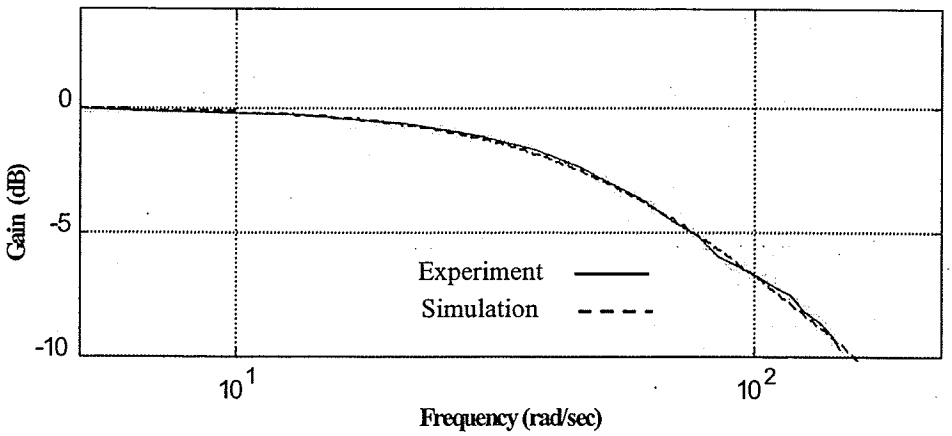

Fig. 2.6: Frequency response for two-stage servovalve.

spool displacement, x_{sp}, and the valve orifice area. For the rectangular port valve in our system, this relationship can be expressed as:

$$\Delta(x_{sp}) = wx_{sp} \tag{2.13}$$

where w is the valve area gradient. The above relation was examined experimentally during steady state runs of the hydraulic actuator and the valve area was calculated indirectly from Eqs. (2.12) for different velocities. The experimental results are shown in Fig. 2.7.

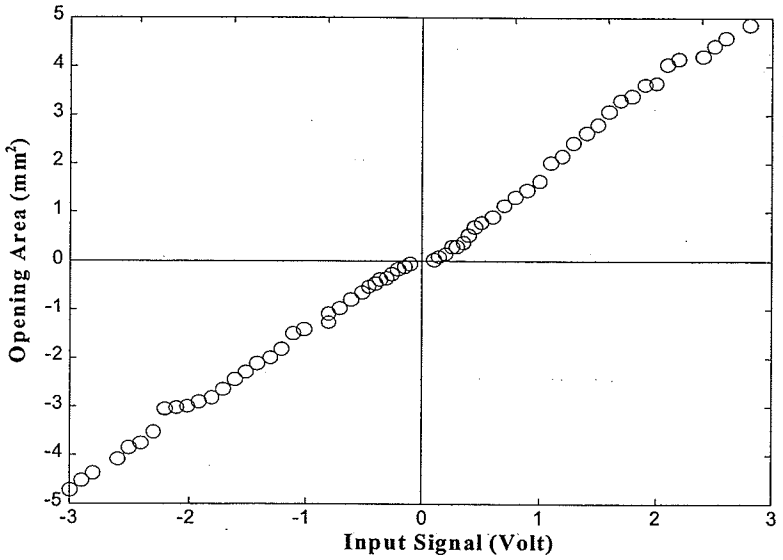

Fig. 2.7: Valve orifice area versus input current.

2.2.3 Cylinder Flow Equations

Neglecting the leakage between cylinder chambers due to effective seals, continuity equations for the oil flow through the cylinder are:

$$q_i = A_i \frac{dx}{dt} + \frac{V_i(x)}{\beta} \frac{dp_i}{dt} \tag{2.14a}$$

$$q_o = A_o \frac{dx}{dt} - \frac{V_o(x)}{\beta} \frac{dp_o}{dt} \tag{2.14b}$$

where β is the effective bulk modulus of the hydraulic fluid, and $V_i(x)$ and $V_o(x)$ are the volumes of the fluid trapped at the sides of the actuator. They are expressed as

$$V_i(x) = \overline{V}_i + xA_i \tag{2.15a}$$

$$V_o(x) = \overline{V}_o - xA_o \tag{2.15b}$$

where $\overline{V}_i$ and $\overline{V}_o$ are the initial fluid volumes trapped in the blind and the rod side of the actuator.

The pump pressure output is adjustable through a relief valve mounted on the pump manifold. Sudden velocity changes in the actuator, however, result in flow demands in the hydraulic supply, which can cause changes in the supply pressure as shown in Fig. 2.8. This may impair the performance of the system. Because of the many variables and nonlinearities involved, prediction of the pressure changes is virtually impossible. Hence, in this study the supply pump pressure is considered as an uncertain value.

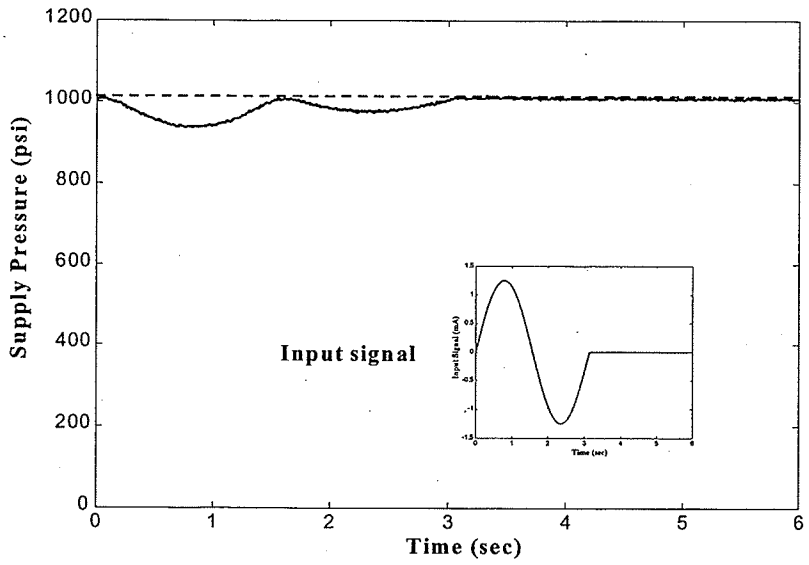

Fig. 2.8: Drop in supply pressure caused by a sinusoidal input.

Chapter 3

Controller Design Using QFT

Quantitative Feedback Theory (QFT) is a frequency domain method primarily intended for practical control system design given robust performance specifications. The concept was first introduced by Horowitz in the early 1960's and was later refined by him and others into a technique (Horowitz, 1992; D'Azzo and Houpis, 1995; Yaniv, 1999). QFT emphasizes the fact that feedback is only necessary because of uncertainty and that the amount of feedback should therefore be directly related to the extent of plant uncertainty and unknown external disturbances. The goal of the technique is to design a low bandwidth controller that satisfies performance specifications, despite system uncertainties and disturbances. A low bandwidth controller is a key issue in any practical design to avoid problems with noise amplification, resonance and unmodeled dynamics. In this chapter a brief outline of the classical QFT problem is presented.

3.1 QFT Configuration

Figure 3.1 shows a typical two degree-of-freedom system in QFT technique when only output Y and command input R can be measured independently. Plant P contains system uncertainties and is exposed to unknown disturbances D_1 and D_2. G represents the controller, which can help reduce the variation of the plant output due to uncertainties and disturbances, while F is used merely as a filter to tailor the response to meet the control system's specifications. The uncertain plant is described as

$$P(s,\alpha) = P_1(s,\alpha)P_2(s,\alpha) = \frac{p_{1m}(\alpha)s^m + \ldots + p_{10}(\alpha)}{p_{0n}(\alpha)s^n + \ldots + p_{00}(\alpha)}, \quad m \le n \qquad (3.1)$$

where $\alpha \in \Omega \subset R^p$ is an uncertain parameter vector. Ω is a compact set of parameter variations and can be given as

$$\Omega = \{\alpha : \alpha_i \in [\underline{\alpha}_i, \overline{\alpha}_i], i = 1, \ldots, p\}$$

where each uncertain parameter α_i ($i=1,\ldots,p$) varies independently within an interval $[\underline{\alpha}_i, \overline{\alpha}_i]$. Choosing a reference parameter vector, α_0, yields the nominal plant $P_0(s)=P(s,\alpha_0)$. Many problems of practical interest can be expressed by the above plant model (3.1) with parametric uncertainty.

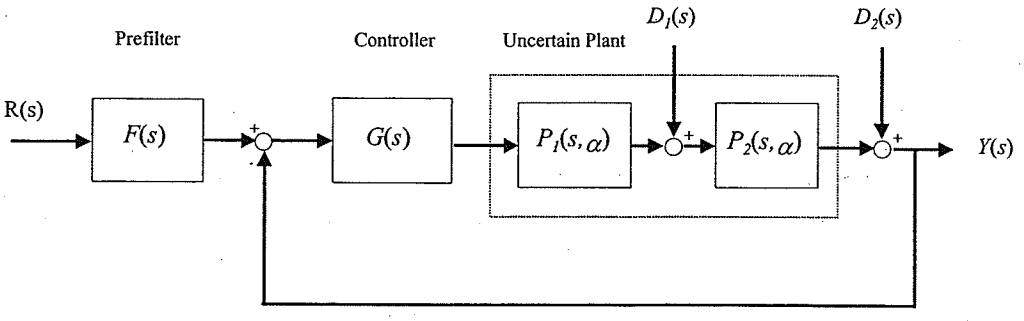

Fig. 3.1: Diagram of a two-degree-of-freedom QFT control system.

3.2 QFT Design Problem

The QFT design problem is to synthesize a pair of strictly proper*, rational, stable functions $G(s)$ and $F(s)$, such that the following specifications are satisfied while the bandwidth of the controller is kept as low as possible.

(*i*) Closed-loop robust stability

QFT stability theorem: the uncertain plant family (3.1) is robustly stable if and only if:

(a) there are no closed right half plane pole-zero cancellations in $G(s)P(s,\alpha)$,

(b) there is an α_0 such that $G(s)$ stabilizes the nominal plant $P_0(s)=P(s,\alpha_0)$, and

(c) $L_0(j\omega)=P_0(j\omega)G(j\omega)\neq -\dfrac{P_0(j\omega)}{P(j\omega,\alpha)}$, for all $\omega\in[0,\infty)$.

Conditions (a) and (b) can be satisfied during the loop shaping process (refer to Section 3.3) in QFT. The third condition is equivalent to placing a magnitude constraint on the closed-loop gain as follows:

$$|T(j\omega,\alpha)|=\left|\frac{L(j\omega,\alpha)}{1+L(j\omega,\alpha)}\right|\leq M \qquad \forall\omega\in[0,\infty) \tag{3.2}$$

where $L(s,\alpha)=P(s,\alpha)G(s)$ is the open-loop transfer function and $T(s,\alpha)$ is the closed-loop transfer function. Parameter M imposes a gain margin (according to $GM\geq 1+\dfrac{1}{M}$) on the closed-loop system stability.

(*ii*) Robust reference input tracking

For tracking performance requirement, the controller should satisfy the following inequality:

$$T_l(\omega) \le \left|F(j\omega)T(j\omega,\alpha)\right| \le T_u(\omega) \qquad \forall \omega \in [0,\infty) \tag{3.3}$$

where T_u and T_l are the upper and lower tracking bounds, respectively. Typical frequency and time domain plots of these bounds are shown in Figs. 3.2a and 3.2b. They are built from the time domain figures of merit for step responses as outlined by D'Azzo and Houpis (1995).

(*iii*) Disturbance rejection, D_1

The requirement for disturbance rejection is expressed as

$$\max_{\alpha\in\Omega}\left|T_D(j\omega,\alpha)\right| \le M_{D_1}(\omega) \qquad \forall \omega \in [0,\omega_1] \tag{3.4}$$

where $T_D(s,\alpha) = \dfrac{p_2(s,\alpha)}{1+L(s,\alpha)}$ is the transfer function from the disturbance to the output and $M_{D_1}(\omega)$ is the magnitude of disturbance rejection.

(*iv*) Disturbance rejection at plant output, D_2 (sensitivity reduction)

For disturbance rejection at plant output, a frequency tolerance is imposed on the sensitivity function as follows:

$$\max_{\alpha\in\Omega}\left|S(j\omega,\alpha)\right| \le M_{D_2}(\omega) \qquad \forall \omega \in [0,\omega_2] \tag{3.5}$$

where $S(s,\alpha) = \dfrac{1}{1+L(s,\alpha)}$ is the sensitivity function and $M_{D_2}(\omega)$ is the magnitude of disturbance rejection.

♣ A transfer function is called *strictly proper* if its denominator degree is greater than its nominator degree.

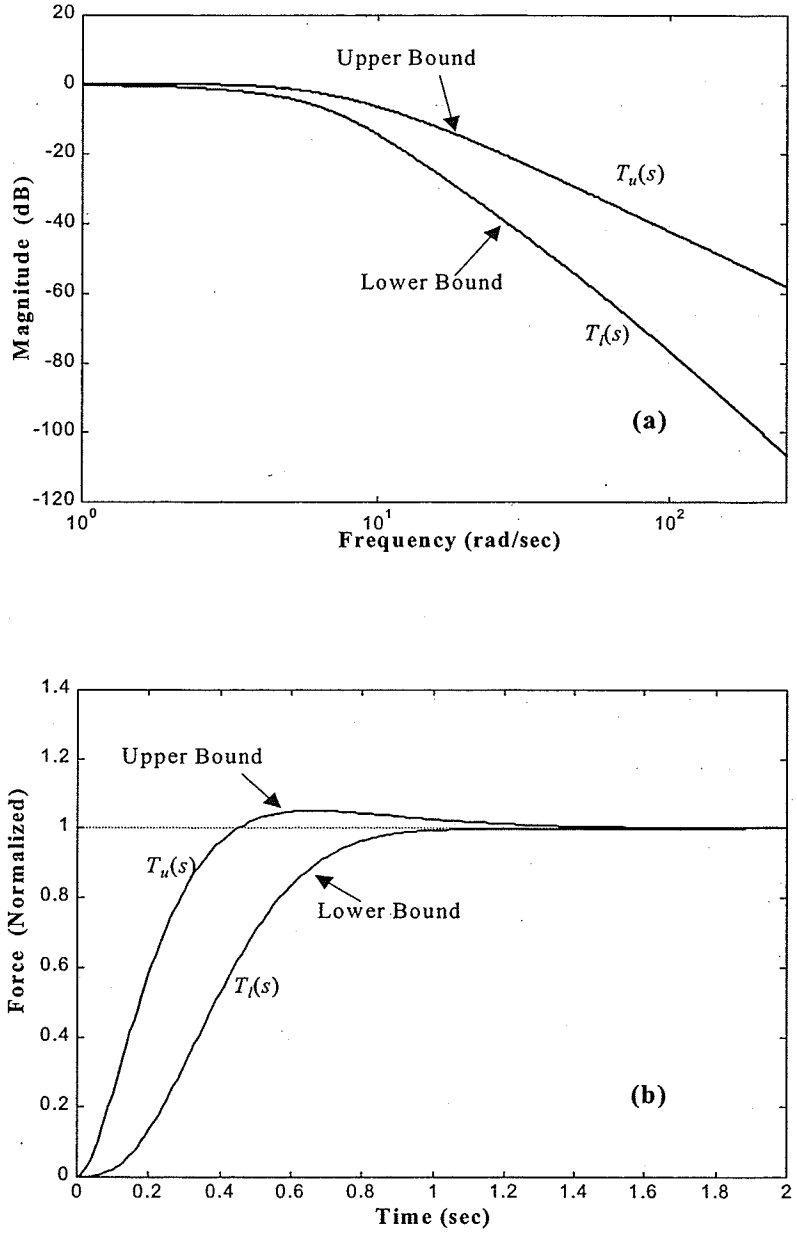

Fig. 3.2: Typical frequency and time domain tracking bounds.

3.3 QFT Design Procedure

The design procedure involves the following steps:

1) Generating the plant template: The region in the Nichols chart occupied by the complex values of $P(j\omega,\alpha)$ at each frequency is called the plant template (see Fig. 3.3). This essentially characterizes the plant uncertainty by capturing the gain and phase variations of the plant at a given frequency. The templates are used to generate bounds on the Nichols chart for the controller design.

2) Generating performance bounds: The design specifications outlined in Section 3.2 should be translated into certain bounds on the nominal open-loop transfer function, $L_0(s) = P_0(s)G(s)$, to reveal the tradeoffs between performance specifications and robustness at each frequency. These bounds are derived either by moving the plant template between the closed-loop magnitude contours on the Nichols chart or by a computer search. At any desired frequency, along a phase angle grid line on the Nichols chart, the computer may be programmed to find the magnitude of $L_0(j\omega)$ that satisfies the equalities in the design specifications. This magnitude could be marked as a boundary point on the Nichols chart. This procedure is repeated on sufficient angle grid lines on the Nichols chart to permit joining the resulting boundary points by a continuous curve. Examples of bounds are shown in Fig. 3.3. These bounds are used in the next step as a guide for loop shaping the nominal open-loop transfer function.

3) Loop shaping: Once the QFT bounds are determined, the nominal loop transfer function, $L_0(s)$, should be designed, by adding proper poles and zeroes, to yield a stable nominal closed-loop, while at the same time satisfying all bounds. A typical

plot of $L_0(s)$ is given in Fig. 3.3. An optimum $L_0(s)$ is one which satisfies the bounds and decreases in magnitude as rapidly as possible with frequency in order to keep the controller bandwidth small. During this stage, the designer should effect a tradeoff between conflicting specifications, controller complexity and the cost of the feedback in the bandwidth. Once a satisfactory $L_0(s)$ is arrived at, the controller can be extracted from $L_0(s)$ by dividing it by the nominal plant transfer function $P_0(s)$.

4) Design of prefilter: Design of a proper $L_0(s)$ only guarantees that the variation in the closed-loop transfer function, $T(s,\alpha)$, is less than or equal to that allowed. Therefore, a prefilter is required to bring the response within the lower and upper tolerances, $T_l(\omega)$ and $T_u(\omega)$. The prefilter magnitude bound at each frequency is calculated from the robust tracking specification. A detailed calculation of $F(s)$ will be presented in a later chapter when an actual controller will be designed.

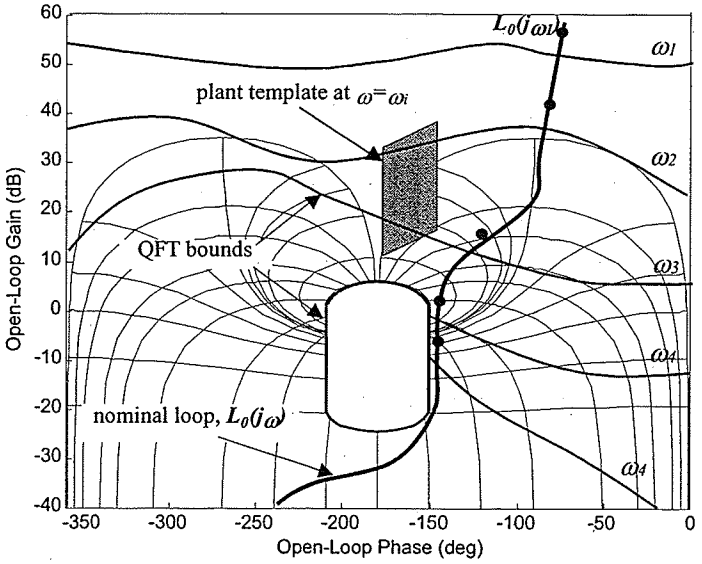

Fig. 3.3: Typical bounds and nominal loop function in Nichols chart.

Chapter 4

Design of the QFT Force Controller

In this chapter, two different approaches, namely linear and nonlinear approaches, will be utilized to design a robust force controller. In the linear approach, nonlinear equations of the system are linearized about an operating point to obtain a linear transfer function. In this approach, the variation of the operating point dependent parameters are included in the model as uncertainty.

The nonlinear approach is based on the identification of linear time-invariant equivalent models that can precisely represent the nonlinear plant under a wide range of operation. Thus, the nonlinear approach is not simply a linearization of the nonlinear plant about an equilibrium point. With this approach, many nonlinearities such as nonlinear valve orifice area openings or variations in the trapped fluid volume, are incorporated into the design procedure. These nonlinearities are normally overlooked in conventional linearized methods.

4.1 Linear Approach ♣

The nonlinear equations derived in Chapter 2 are linearized about an operating point to obtain a linear transfer function. The objective is to utilize this model within the QFT technique.

4.1.1 Linearized Model

In this section the derivation procedure is followed step-by-step to highlight the assumptions and simplifications that are made.

The linearized flow relationships from (2.12) are

$$q_i = K_s^i x_{sp} - K_p^i p_i \tag{4.1a}$$

$$q_o = K_s^o x_{sp} + K_p^o p_o \tag{4.1b}$$

where K_s^i (K_s^o) and K_p^i (K_p^o) represent flow and pressure sensitivity gains of the valve, respectively. They are given as follows:

for extension ($x_{sp} \geq 0$)	*for retraction ($x_{sp} < 0$)*
$K_s^i = c_d w\sqrt{\frac{2}{\rho}(p_s - p_i)}$	$K_s^i = c_d w\sqrt{\frac{2}{\rho}(p_i - p_e)}$
$K_s^o = c_d w\sqrt{\frac{2}{\rho}(p_o - p_e)}$	$K_s^o = c_d w\sqrt{\frac{2}{\rho}(p_s - p_o)}$
$K_p^i = \frac{c_d w x_{sp}}{\sqrt{2\rho(p_s - p_i)}}$	$K_p^i = \frac{-c_d w x_{sp}}{\sqrt{2\rho(p_i - p_e)}}$
$K_p^o = \frac{c_d w x_{sp}}{\sqrt{2\rho(p_o - p_e)}}$	$K_p^o = \frac{-c_d w x_{sp}}{\sqrt{2\rho(p_s - p_o)}}$

♣ A version of this section has been published in *IEEE Control Systems Magazine*, Vol. 2, pp. 66-77, 2001, "Designing Robust Force Control of Hydraulic Actuators Despite System and Environmental Uncertainties"; N. Niksefat and N. Sepehri.

As is seen, K_s^i (K_s^o) and K_p^i (K_p^o) are load- and pressure-dependent variables; hence in this study, they are considered uncertain but bounded parameters. Assuming small piston displacements within the vicinity of the mid-stroke, the following approximation can be made:

$$\frac{V_i(x)}{\beta} \approx \frac{V_o(x)}{\beta} \approx \frac{1}{\beta}\left(\frac{\overline{V}_i + \overline{V}_o}{2}\right) = C \tag{4.2}$$

Thus, Eqs. (2.14) can be written in the Laplace domain as follows:

$$Q_i = A_i sX + CsP_i \tag{4.3a}$$

$$Q_o = A_o sX - CsP_o \tag{4.3b}$$

Substituting Eqs. (4.1) into (4.3), and rearranging for line pressures:

$$P_i = -\frac{A_i s}{Cs + K_p^i} X + \frac{K_s^i}{Cs + K_p^i} X_{sp} \tag{4.4}$$

$$P_o = \frac{A_o s}{Cs + K_p^o} X - \frac{K_s^o}{Cs + K_p^o} X_{sp} \tag{4.5}$$

Eqs. (2.1) to (2.3) can be represented in Laplace form as:

$$[m_a s^2 + (d + d_s)s + k_s]X - (d_s s + k_s)X_s = P_i A_i - P_o A - F_d \tag{4.6}$$

$$[m_e s^2 + (d_e + d_s)s + k_s + k_e]X_s = (d_s s + k_s)X \tag{4.7}$$

From (4.6) we have,

$$\frac{X(s)}{F_m(s)} = \frac{1}{k_s}\frac{m_e s^2 + (d_e + d_s)s + k_s + k_e}{m_e s^2 + d_e s + k_e} \tag{4.8}$$

where $F_m(s) = k_s(X - X_s)$ is the measured force by the sensor (see Fig. 2.3). Substituting (4.4), (4.5), and (4.8) into (4.6) and rearranging it, the controlled force is derived as:

$$F_m(s) = \left\{\frac{F_m(s)}{X_{sp}(s)}\right\}_{F_d=0} X_{sp} - \left\{\frac{F_m(s)}{-F_d(s)}\right\}_{X_{sp}=0} F_d \tag{4.9}$$

where $\left\{\frac{F_m(s)}{X_{sp}(s)}\right\}$ and $\left\{\frac{F_m(s)}{-F_d(s)}\right\}$ are the transfer functions relating the measured force, F_m, to the spool displacement and disturbance force, F_d, respectively:

$$\left\{\frac{F_m(s)}{X_{sp}(s)}\right\} = \frac{k_s(m_e s^2 + d_e s + k_e)(K_s^i A_i (K_p^i + Cs) + K_s^o A_o (K_p^o + Cs))}{\Delta(s)} \tag{4.10}$$

$$\left\{\frac{F_m(s)}{-F_d(s)}\right\} = \frac{k_s(m_e s^2 + d_e s + k_e)(K_p^i + Cs)(K_p^o + Cs)}{\Delta(s)} \tag{4.11}$$

where

$$\Delta(s) = (K_p^i + Cs)(K_p^o + Cs)(\psi(s)\varphi(s) + \zeta(s)\varphi(s) + \psi(s)\zeta(s)) + (A_i^{\,2} s(K_p^i + Cs) + A_o^{\,2} s(K_p^o + Cs))(\varphi(s) + \zeta(s))$$

$$\varphi(s) = m_e s^2 + d_e s + k_e$$

$$\psi(s) = m_a s^2 + d$$

and

$$\zeta(s) = d_s s + k_s$$

In order to simplify the above transfer functions, K_s^i (K_s^o) and K_p^i (K_p^o) are simply replaced by K_s and K_p. Hence, transfer functions (4.10) and (4.11) are reduced to the following:

$$\left\{\frac{F_m(s)}{X_{sp}(s)}\right\} = \frac{k_s K_s (A_i + A_o)(m_e s^2 + d_e s + k_e)}{(K_p + Cs)((\psi(s)\varphi(s) + \zeta(s)\varphi(s) + \psi(s)\zeta(s)) + (A_i^{\,2} s + A_o^{\,2} s)(\varphi(s) + \zeta(s))} \tag{4.12}$$

$$\left\{\frac{F_m(s)}{-F_d(s)}\right\} = \frac{k_s(m_e s^2 + d_e s + k_e)(Cs + K_p)}{(K_p + Cs)((\psi(s)\varphi(s) + \zeta(s)\varphi(s) + \psi(s)\zeta(s)) + (A_i^{\,2} s + A_o^{\,2} s)(\varphi(s) + \zeta(s))} \tag{4.13}$$

Any variation or approximation in K_s^i (K_s^o) and K_p^i (K_p^o) are now included as uncertainty in K_s and K_p, respectively. The above relations are further simplified if the stiffness of the force sensor and the piston rod are high, in comparison with the environmental stiffness and the hydraulic compliance. Hence, their dynamics are not excited during contact, and can be lumped together as a rigid body (Wu et al., 1998). Based on this assumption, Eqs. (4.12) and (4.13) are then rewritten as follows:

$$\left\{\frac{F_m(s)}{X_{sp}(s)}\right\} = \frac{K_s(A_i + A_o)(m_e s^2 + d_e s + k_e)}{(K_p + Cs)(m_a s^2 + (d + d_e)s + k_e) + (A_i^2 s + A_o^2 s)} \tag{4.14}$$

$$\left\{\frac{F_m(s)}{-F_d(s)}\right\} = \frac{(m_e s^2 + d_e s + k_e)(Cs + K_p)}{(K_p + Cs)(m_a s^2 + (d + d_e)s + k_e) + (A_i^2 s + A_o^2 s)} \tag{4.15}$$

Further, we assume that the dynamics of the environment are dominated by a pure stiffness, k_e. This type of environment has enjoyed popularity among many researchers (Seraji and Colbaugh, 1997). The system transfer functions are finally written in their simplest forms as:

$$\left\{\frac{F_m(s)}{X_{sp}(s)}\right\} = \frac{K_s k_e(A_i + A_o)}{(K_p + Cs)(m_a s^2 + ds + k_e) + (A_i^2 s + A_o^2 s)} \tag{4.16}$$

$$\left\{\frac{F_m(s)}{-F_d(s)}\right\} = \frac{k_e(K_p + Cs)}{(K_p + Cs)(m_a s^2 + ds + k_e) + (A_i^2 s + A_o^2 s)} \tag{4.17}$$

Including the dynamics of the valve from Eq. (2.11), the transfer function between measured contact force, $F_m(s)$, and control voltage, $U(s)$, is written as:

$$\left\{\frac{F_m(s)}{U(s)}\right\} = \left\{\frac{F_m(s)}{X_{sp}(s)}\right\}\frac{k_{sp}}{\tau s + 1} = \frac{k_{sp}}{(\tau s + 1)}\left[\frac{K_s k_e(A_i + A_o)}{(K_p + Cs)(m_a s^2 + ds + k_e) + (A_i^2 s + A_o^2 s)}\right] \tag{4.18}$$

Equation (4.18) is now considered as a parametrically uncertain system. For example, the uncertainty ranges in K_s and K_p reflect variations in the operating point, supply pressure and, in part, the orifice area gradient. The variations in the environmental stiffness and damping of the system are included in parameters k_e and d, respectively. Furthermore, the uncertainty in C represents the changes in the fluid bulk modulus and the volumes of fluid trapped at the sides of the actuator. The uncertainty in the valve characteristic is captured in variations of τ and k_{sp}. All these parameters are known to have an effect on the system's stability. Table 4.1 lists the nominal values of all parameters in Eqs. (4.17) and (4.18), and their corresponding uncertainty ranges. The Bode plot of the open-loop transfer functions of the system describing by Eq. (4.18) is shown in Fig. 4.1. The uncertain parameters are grouped into a vector, denoted as α. Thus, the system's open-loop transfer function can be shown as

$$P(s,\alpha) = \left\{ \frac{F_m(s)}{U(s)} \right\} \tag{4.19}$$

$$P_2(s,\alpha) = -\left\{ \frac{F_m(s)}{-F_d(s)} \right\} \tag{4.20}$$

The plant evaluated at its nominal operating point is referred to here as *nominal plant* and is shown as:

$$P_0(s) = P(s,\alpha_o) \tag{4.21}$$

where α_o is the vector containing all nominal values of the plant transfer function.

Table 4.1: Operating values and parameter ranges pertaining to the linear transfer function.

Parameter	Nominal Value		Range
k_e	70	(kN/m)	30-100
d	400	(N/m/sec)	300-500
m_a	10	(kg)	9.9-10.1
A_i	$1.14(10)^{-3}$	(m^2)	$1.11(10)^{-3}$-$1.17(10)^{-3}$
A_o	$0.63(10)^{-3}$	(m^2)	$0.61(10)^{-3}$-$0.65(10)^{-3}$
k_{sp}	$1.45(10)^{-4}$	(m/V)	$1.3(10)^{-4}$-$1.6(10)^{-4}$
τ	30	(msec)	20-40
K_s	0.45	(m^3/Pa.sec)	0.3-0.5
K_p	$2.0(10)^{-12}$	(m^2/sec)	$0\text{-}4(10)^{-12}$
C	$1.5(10)^{-11}$	(m^3/Pa)	$1(10)^{-11}$-$3(10)^{-11}$

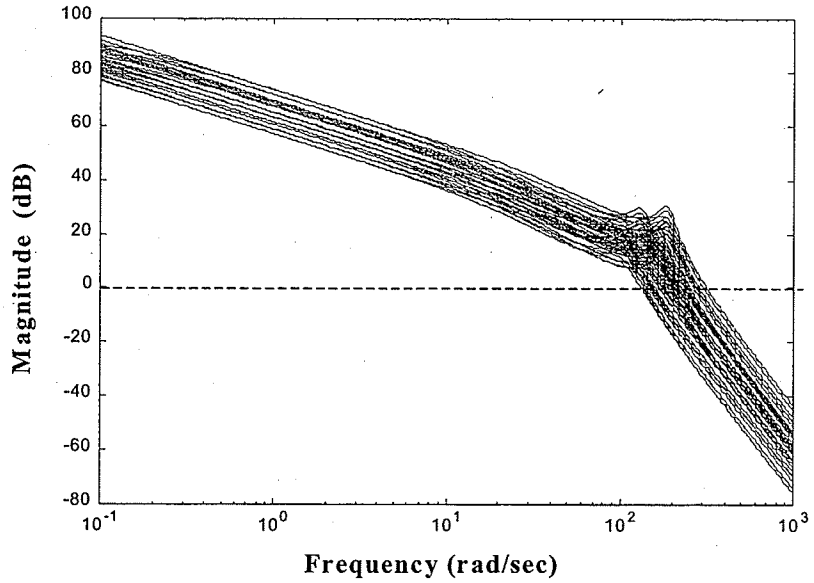

Fig. 4.1: Bode plot of open-loop transfer functions.

4.1.2 Controller Synthesis

The uncertain transfer functions (4.19) and (4.20) are now used to design a robust force controller. A strictly proper controller, $G(s)$, and a strictly proper prefilter, $F(s)$, are to be designed such that the constraints (3.2) to (3.5) be satisfied. The upper and lower bounds, shown in (3.3) are chosen as follows:

$$T_u(s) = \frac{(\frac{s}{2.8}+1)}{(\frac{s}{4}+1)(\frac{s}{7}+1)(\frac{s}{8}+1)} \tag{4.22a}$$

$$T_l(s) = \frac{1}{(\frac{s}{4.8}+1)(\frac{s}{80}+1)(\frac{s^2}{50}+\frac{9.6s}{50}+1)} \tag{4.22b}$$

These bounds are built from the time domain figures of merit for step responses such as peak overshoot, peak time, and settling time (D'Azzo and Houpis, 1995, pp. 586-589). In this work, the desired lower tracking bound, $T_l(s)$, is built to have an overdamped response with ~1 sec settling time. For this purpose, a model with a real pole at s = -4.8, and a pair of complex poles are chosen. The real pole must be more dominant than the complex poles (D'Azzo and Houpis, 1995). Moreover, a high frequency pole at s = -80 is inserted in $T_l(s)$ which does not affect the desired performance specification but widens the range between $T_u(s)$ and $T_l(s)$ in the high frequency band. The figures of merit for upper bound, $T_l(s)$, are a 5% peak overshoot and ~1 *sec* settling time. $T_u(s)$ is selected with three real poles and a zero. The zero is closer to origin than the poles, in order to have an underdamped response.

As well, M in Eq. (3.2) is chosen as M=1.4, implying an approximate gain margin of 3 dB (according to $GM \geq 1+\frac{1}{M}$) for the closed-loop system stability. For disturbance

rejection it is desired that the output decays to 2% of the maximum value at t_s=0.1 sec. The desired specification for the disturbance rejection is satisfied by choosing M_{D_1} in (3.4) as (D'Azzo and Houpis, 1995, pp. 418-422),

$$M_{D_1}(\omega) = \left| \frac{750 j\omega}{(j\omega + 100)^2} \right| \tag{4.23}$$

The time domain for this bound is shown in Fig. 4.4b. Also, a constant upper bound for the sensitivity function in (3.5) is considered (i.e., $M_{D_2}(\omega)$ =1.2) to limit the peak value of the disturbance amplification.

Design frequencies are selected as ω = { 0.01,0.05,0.1,1,5,7,10,30,50,70,100 } rad/sec. The bounds generated by constraints (3.2) to (3.5) are shown in Fig. 4.2a with the uncompensated plant. The nominal open-loop transfer function, L_0, must be shaped to satisfy all these bounds at each frequency. For low frequencies, L_0 should lie on or above the bounds to satisfy the constraints; however, for higher frequencies in the range, e.g., ω = 50, 70 and 100 rad/sec, the constraints generate closed boundaries which L_0 should not enter. For the industrial hydraulic actuator under investigation, the valve dead-band produces a steady-state error in the system response in the absence of an integrator. For a zero steady-state error, L_0 must contain an integrator. Thus, a possible loop can be obtained by cascading an integrator. Further, a gain of 0.052 is required to bring the open-loop transfer function within the specification bounds. Two zeroes should be added to the structure of the controller to satisfy the bounds and to force the nominal loop, L_0, to the right hand side of the closed boundaries. After several iterations the controller zeroes were chosen to be s=-3.8 and s=-39. At this stage, L_0 closely follows the bounds up to ω= 70 rad/sec. The next step is to add two high frequency poles to allow for a quick descent

of the nominal loop to decrease the cost of feedback. Fig. 4.2b shows the final loop shaping of the system. The controller that satisfies the specifications is:

$$G(s) = \frac{0.052(\frac{s}{3.8}+1)(\frac{s}{39}+1)}{s(\frac{s}{100}+1)(\frac{s}{300}+1)} \tag{4.24}$$

To satisfy the tracking specification, a prefilter, $F(s)$, is required to place the closed-loop frequency response in the specified range, between $T_l(s)$ and $T_u(s)$. Fig 4.3a shows the frequency response of the closed-loop system without a prefilter where the designed controller (4.24) only guarantees that the variation in the system's magnitude will be less than or equal to that allowed. The prefilter is synthesized by calculating its magnitude bound at each frequency. For example, in Fig. 4.3a, consider the frequency response of the control system at $\omega = 20$ rad/sec. The maximum magnitude variation, δ, is about 9 dB = 3-(-6), which is less than the amount allowed for this frequency, i.e. $\delta_{all} = |T_u(j20)|-|T_l(j20)|$= -15-(-30) = 15 dB. The acceptable magnitude of the prefilter at this frequency is then found to be, -30-(-6) ≤ $|F(j20)|$ ≤ -15-(3). By applying the above procedure for the design frequency range, a suitable prefilter is found to be:

$$F(s) = \frac{1}{(\frac{s}{6.5}+1)(\frac{s}{6.7}+1)} \tag{4.25}$$

The closed-loop Bode plots of the plant for extreme parameter conditions are given in Fig. 4.3b. The corresponding closed-loop simulated time responses to a step input of 1000 N and a step disturbance of 1000 N are shown in Fig. 4.4.

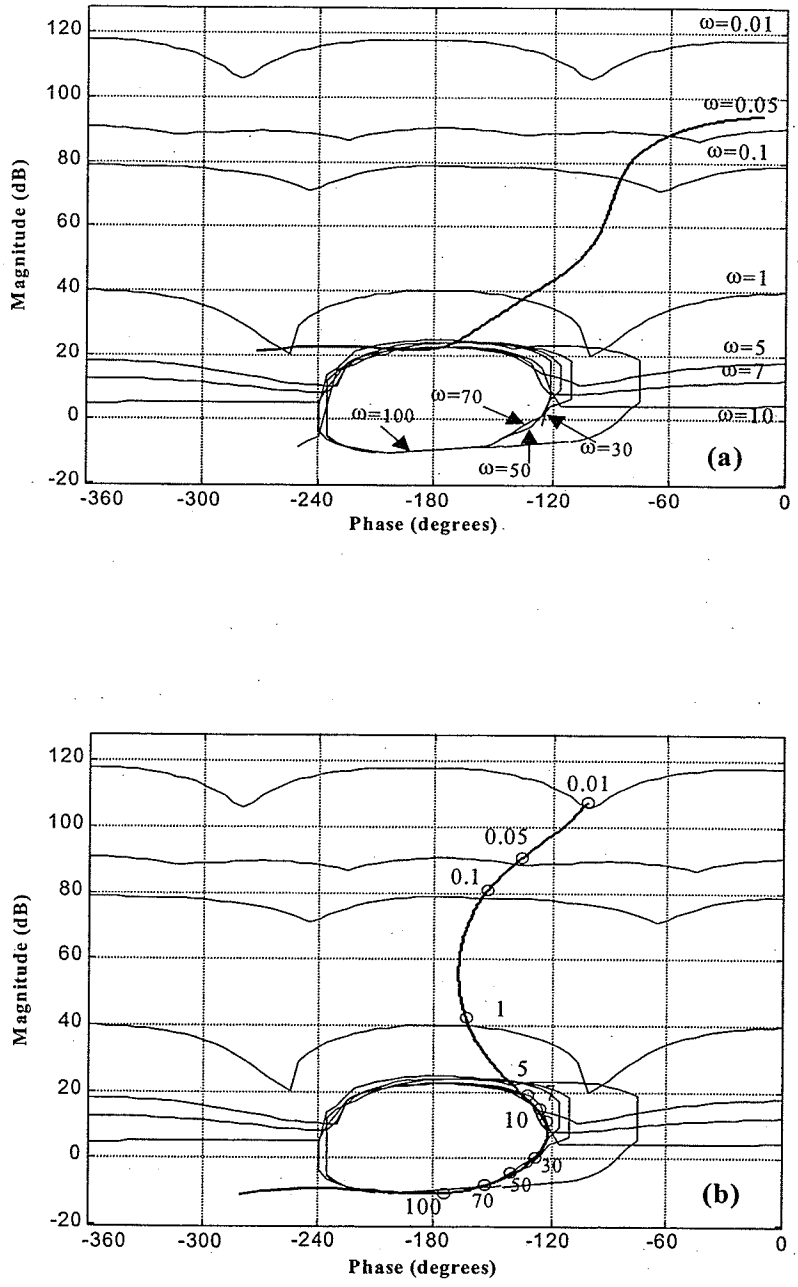

Fig. 4.2: QFT bounds on Nichols chart with: **(a)** uncompensated plant; **(b)** nominal loop.

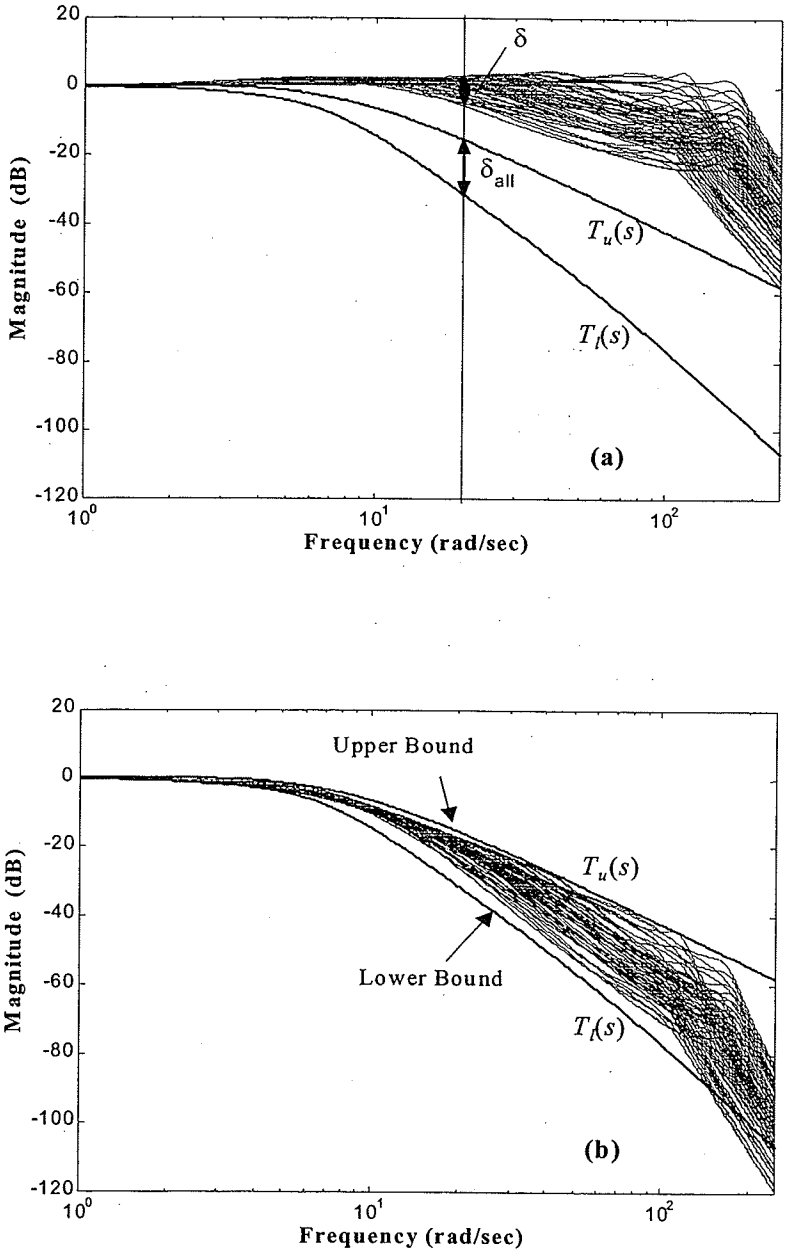

Fig. 4.3: Closed-loop frequency responses over range of parametric uncertainty: **(a)** without prefilter; **(b)** with prefilter.

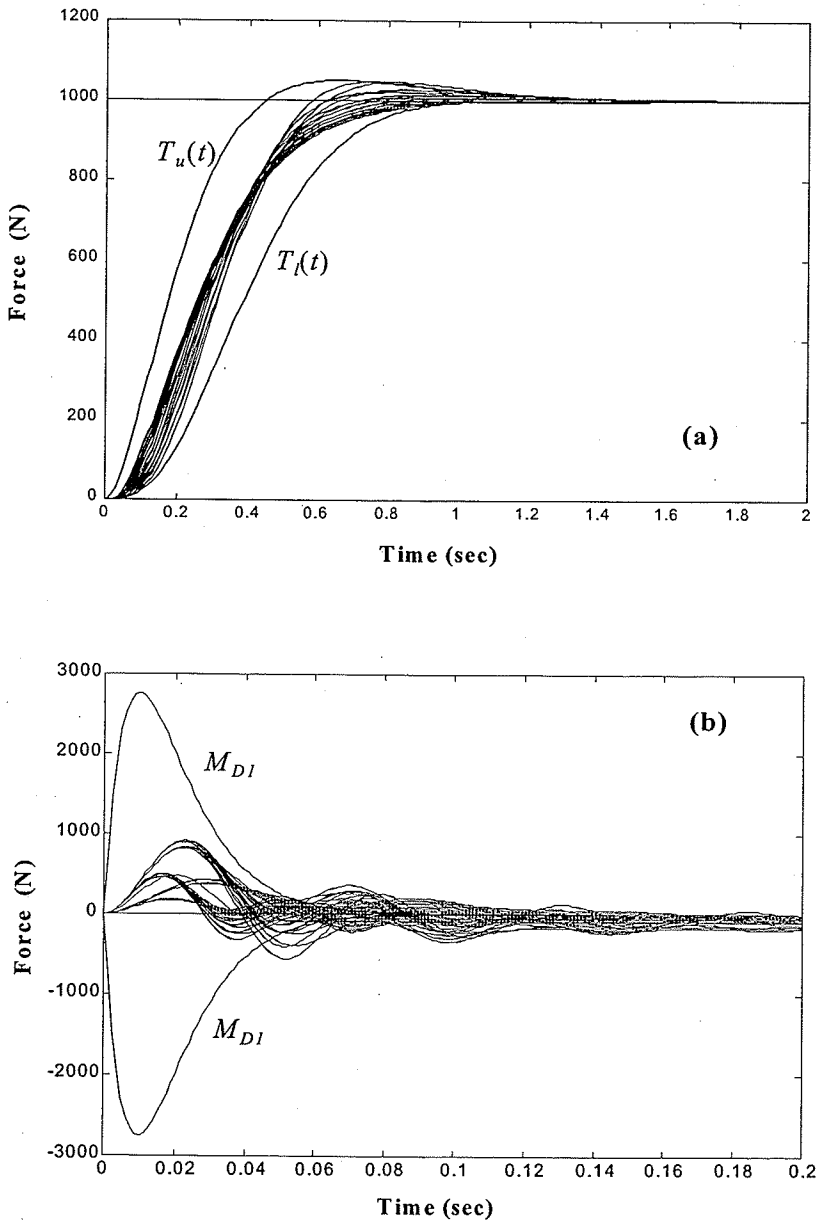

Fig. 4.4: System responses over range of parametric uncertainty: **(a)** step input; **(b)** step disturbance (d_l(t)=1000 N).

4.1.3 Experimental Results

The controller described by transfer function (4.24) was discretized and implemented on the experimental test stand using the Tustin method in Matlab environment. The maximum achievable sampling frequency, 200 Hz, was used for the controller. The effects of variation in environmental stiffness, supply pressure and force set-point were experimentally studied. First the variation of environmental stiffness was studied by utilizing different springs. Two different springs with stiffnesses of 35 kN/m and 100 kN/m were used for this purpose. The results are shown in Fig. 4.5. As is seen, the controller was capable of handling the changes in the environmental stiffness and the steady-state errors are small. With reference to Fig. 4.5, responses exhibit initial delays mainly due to small dead-band and dry friction in the servovalve used in this experiment. The effect of valve dead-band was not incorporated into the QFT design procedure and was only handled by cascading an integrator in the controller. The corresponding pump pressure for this experiment is shown in Fig. 4.6.

Fig. 4.7 compares the test results for three different reference forces (500 N, 750 N and 1000 N) and with similar environmental stiffness (75 kN/m). As shown in this figure, despite changing the loading condition, the system's rise time did not change considerably. The ability of the controller to cope with pump pressure variations was also tested. Typical results are shown in Fig. 4.8, where the pump pressure was varied 100%. The control signal is shown in Fig. 4.9.

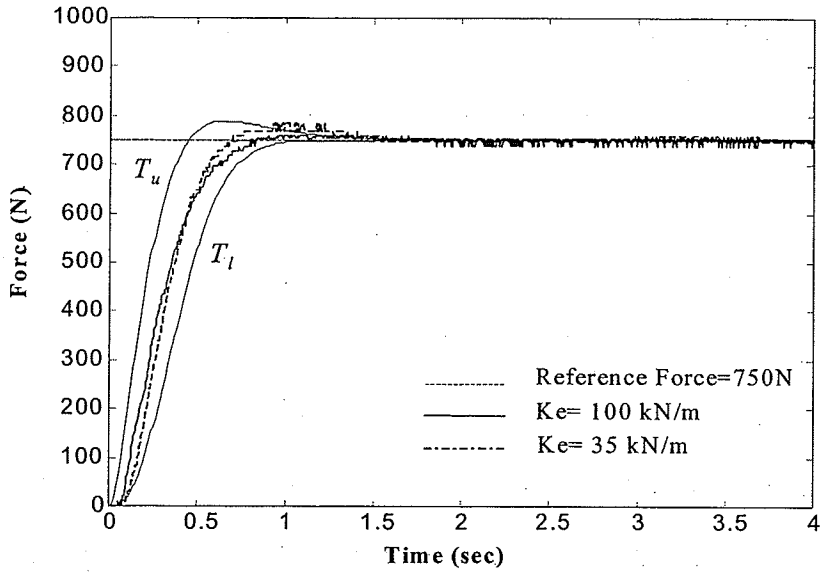

Fig. 4.5: Step force responses with different environmental stiffnesses.

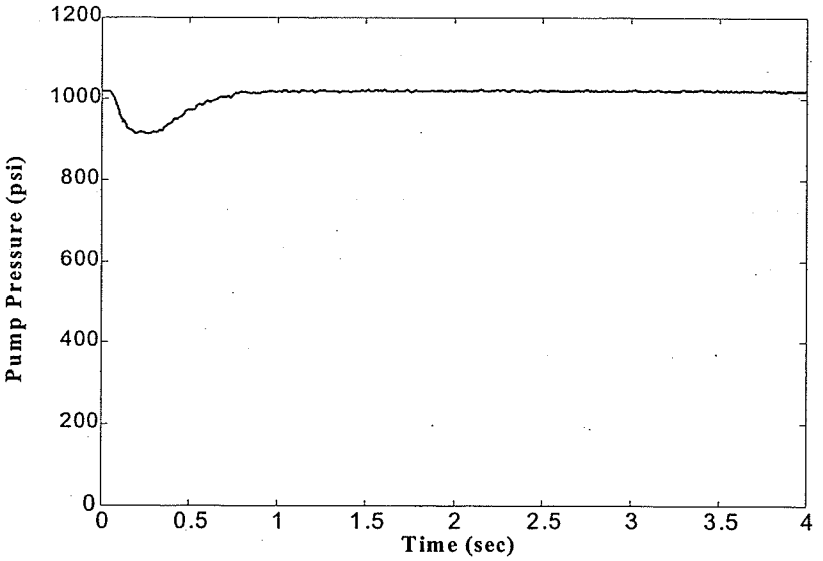

Fig. 4.6: Pump pressure pertaining to experiment in Fig. 4.5.

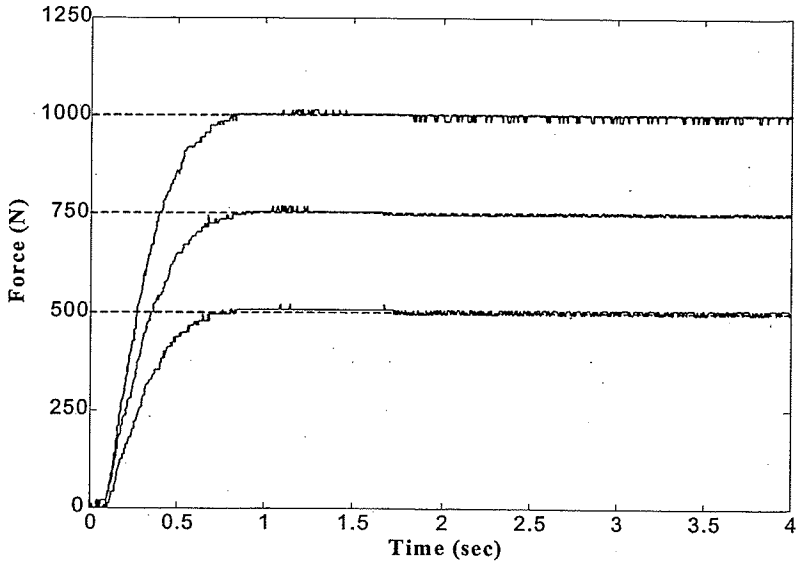

Fig. 4.7: Step force responses for different reference forces.

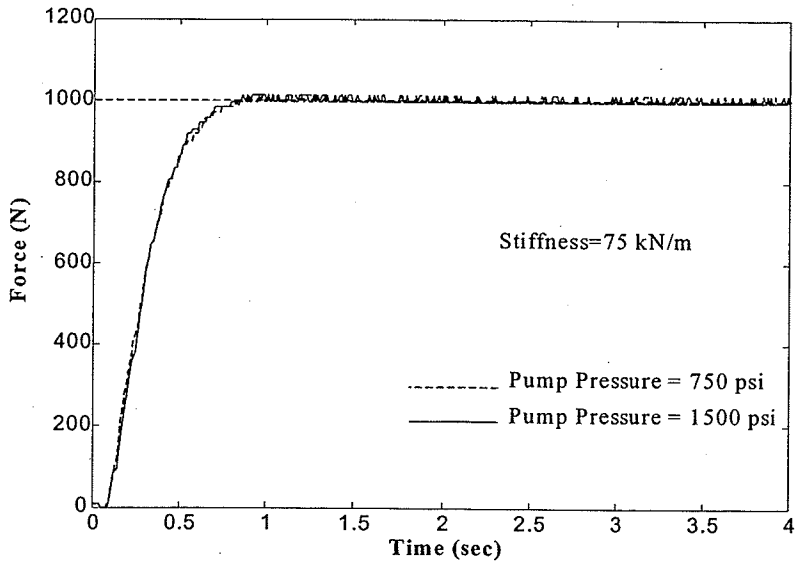

Fig. 4.8: Step force responses for different supply pressures.

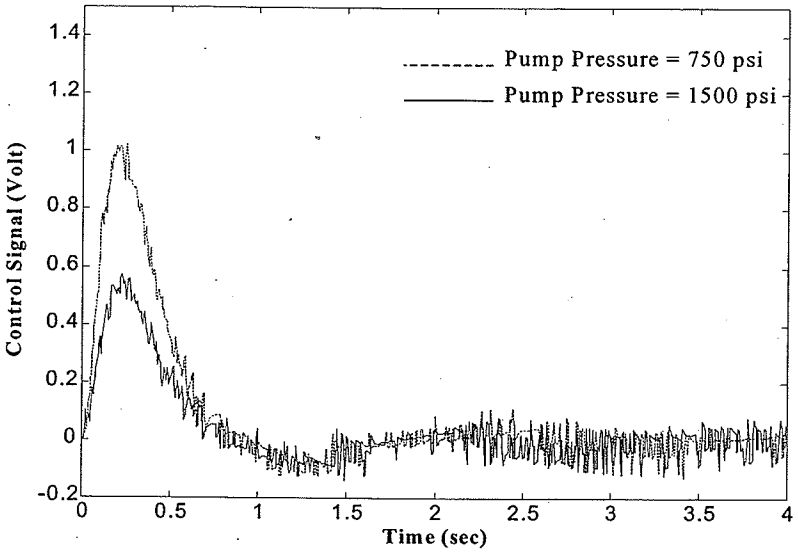

Fig. 4.9: Control signal pertaining to experiment in Fig. 4.8.

4.2 Nonlinear Approach *

The approach taken in this section is to first identify linear time-invariant equivalent models that can precisely represent the nonlinear plant under a wide range of operation. Two methods are employed to find the equivalent models. The first method utilizes experimental input-output data obtained directly from acceptable performance of the actual system. Generally this method is applicable to linear or nonlinear plants for which no analytical model is available (Horowitz, 1992). For example, this method has been applied to design a controller to automate a welding process and the input-output data set was generated by experienced welders (Bentley, 1992). This method is also suitable for implementation on complex hydraulic systems, such as excavator machines, for which the derivation of mathematical models and the determination of many parameters are difficult and time-consuming. The second method is model-based and employs the general nonlinear mathematical model of the system. The acceptable input-output set is derived analytically or through numerical simulations. This method has been successfully applied to design robust flight controllers based on a nonlinear model of the aircraft (Miller et al., 1992). In this work, a nonlinear mathematical model of the hydraulic actuator interacting with an environment, derived in Chapter 2, is employed. The input-output data set obtained from either the experimental or model-based method is then used within an algorithm proposed by Golubev and Horowitz (1982) to derive the equivalent time-invariant plant models. Once the equivalent time-invariant plant models are derived,

* A version of this section has been published in *IFAC Journal of Control Engineering Practice*, Vol. 8, pp. 1335-1345, 2000, "Design and Experimental Evaluation of a Robust Force Controller for an Electro-Hydraulic Actuator via Quantitative Feedback Theory"; N. Niksefat and N. Sepehri.

a robust controller is designed to provide desirable performance for the entire set of members.

4.2.1 Controller Design

In Fig. 4.10, the controller $G(s)$, and the prefilter $F(s)$, are to be designed to meet frequency bound specifications, where $w \in \mathscr{W}$ describes any member of the nonlinear and/or time-varying plant. Let set $\mathscr{Y}$ contain all acceptable plant outputs, y_a. The linear time-invariant equivalent of $\mathscr{W}$ is defined as

$$\mathscr{P} = \left\{ p_{eq} \mid p_{eq} = \frac{\mathscr{L}[y_a]}{\mathscr{L}[x_a]}, y_a \in \mathscr{Y}, x_a = w^{-1}(y_a), w \in \mathscr{W} \right\} \tag{4.26}$$

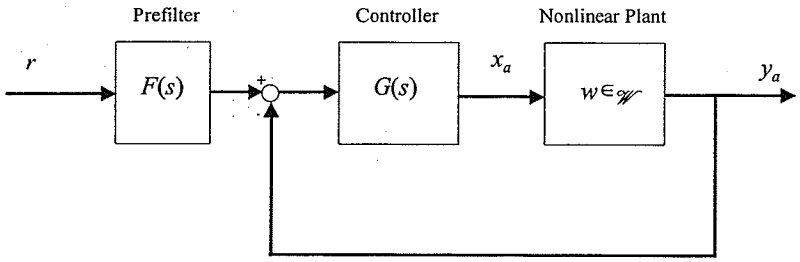

Fig. 4.10: Two-degree-of-freedom QFT control system.

where $\mathscr{L}[..]$ denotes the Laplace transform. If it is possible to solve the resulting linear time-invariant equivalent problem, then the same $F(s)$ and $G(s)$ guarantee the solution of the original nonlinear problem. The following is a brief outline of the proof.

For any x_a and $w \in \mathscr{W}$, define a mapping on $\mathscr{Y}_s = \{\mathscr{L}[y_a];\ y_a \in \mathscr{Y}\}$:

$$\Phi(Y_a) = \frac{R(s)F(s)G(s)\dfrac{Y_a(s)}{X_a(s)}}{1 + G(s)\dfrac{Y_a(s)}{X_a(s)}} \tag{4.27}$$

If Φ maps $\mathscr{Y}_S$ onto itself and is continuous, then, based on Schauder's fixed point theorem (Horowitz, 1992, pp. 308-312), there exists a fixed point,

$$Y_a^* = \frac{R(s)F(s)G(s)\dfrac{Y_a^*(s)}{X_a^*(s)}}{1+G(s)\dfrac{Y_a^*(s)}{X_a^*(s)}} \tag{4.28}$$

where

$$X_a^* = G(s)(R(s)F(s) - Y_a^*(s))$$

which clearly gives a solution Y_a^* to the original nonlinear problem of Fig. 4.10 with $Y_a^* \in \mathscr{Y}_S$, the acceptable plant output set. The most important condition in the proof is that in Eq. (4.28), Φ maps $\mathscr{Y}_S$ onto itself and this is achieved (given the same F and G) for all $w \in \mathscr{W}$. Recall the definition of $\mathscr{P}$, and it is seen that this condition is precisely the condition for which the linear time-invariant equivalent problem is solved.

Once the acceptable plant input-output set is determined, experimentally or numerically, Golubev's method is applied. Golubev's method takes the time histories of input-output signal pairs and determines a linear transfer function relating the two. To demonstrate this, consider an input-output pair, $(x_T(t), y_T(t))$ on $t \in [0,T]$. Let $\mathscr{X}_t=\{x(t)\}$ and $\mathscr{Y}_t=\{y(t)\}$ be the sets of all extensions of $x(t)$ and $y(t)$ to $[0,\infty)$ such that $\mathscr{L}[x(t)]=X(s)$ and $\mathscr{L}[y(t)]=Y(s)$ exist with $\mathscr{X}_S=\{X(s)\}$ and $\mathscr{Y}_S=\{Y(s)\}$. Also, let $\mathscr{F}_S=\{F(s)=Y(s)/X(s);\ X(s)\in \mathscr{X}_S,\ Y(s)\in \mathscr{Y}_S\}$. $R(s)$ is a rational function, whose coefficients should be determined, in the form of:

$$R(s) = \frac{P_m(s)}{Q_n(s)} = \frac{\sum_{k=0}^{m} p_k s^k}{\sum_{k=0}^{n} q_k s^k} \tag{4.29}$$

The distance between $R(s)$ and $\mathcal{F}_s$ is defined by:

$$d(R,\mathcal{F}_s) = \inf_{X\in\mathcal{X}_s \; Y\in\mathcal{Y}_s} \int_{-\infty}^{\infty} \left| \frac{Q_n(j\omega)Y(j\omega) - P_m(j\omega)X(j\omega)}{(j\omega)^n} \right|^2 d\omega \tag{4.30}$$

Applying Eq. (4.29) in (4.30),

$$\begin{aligned} d(R,\mathcal{F}_s) &= \inf_{X\in\mathcal{X}_s \; Y\in\mathcal{Y}_s} \int_{-\infty}^{\infty} \left| \frac{\sum_{k=0}^{n} q_k (j\omega)^k Y(j\omega) - \sum_{k=0}^{m} p_k (j\omega)^k X(j\omega)}{(j\omega)^n} \right|^2 d\omega \\ &= \inf_{X\in\mathcal{X}_s \; Y\in\mathcal{Y}_s} \int_{-\infty}^{\infty} \left| \sum_{k=0}^{n} q_k \frac{Y(j\omega)}{(j\omega)^{n-k}} - \sum_{k=0}^{m} p_k \frac{X(j\omega)}{(j\omega)^{n-k}} \right|^2 d\omega \end{aligned} \tag{4.31}$$

From the Parseval Formula (Golubev and Horowitz, 1982), Eq. (4.31) will be equal to,

$$d(R,\mathcal{F}_s) = \inf_{X\in\mathcal{X}_1 \; Y\in\mathcal{Y}_1} \int_{-\infty}^{\infty} \left| \sum_{k=0}^{n} q_k y^{(k-n)}(t) - \sum_{k=0}^{m} p_k x^{(k-n)}(t) \right|^2 dt \tag{4.32}$$

where

$$y^{(0)}(t) = y(t), \qquad y^{(-n-1)}(t) = \int_0^t y^{(-n)}(\tau) d\tau$$

Denoting the expression under the integral in Eq. (4.32) by $I(R,x,y)$, we have

$$d(R,\mathcal{F}_s) = \inf_{X\in\mathcal{X}_1 \; Y\in\mathcal{Y}_1} \left[\int_{-\infty}^{0} I(R,x,y)dt + \int_0^T I(R,x,y)dt + \int_T^{\infty} I(R,x,y)dt \right] = \inf \left[I_1 + I_2 + I_3 \right] \tag{4.33}$$

where $I_1=0$ because $x,y=0$ for $t<0$. Since x and y are arbitrarily defined for $t>T$, therefore for any P_m and Q_n there exist x and y such that $I_3=0$. This means that for an arbitrary $x(t)$ for $t>T$, and for arbitrary P_m and Q_n, $y(t)$ is the solution to the equation

$$\sum_{k=0}^{n} q_k y^{(k)}(t) = \sum_{k=0}^{m} p_k x^{(k)}(t) \tag{4.34}$$

with initial values $y^{(k)}(T)$ known from $y\in[0,T]$ calculated from the rational function approximation. Hence, $d(R,\mathcal{F}_s)=\inf I_2=I_2$, because I_2 does not depend on the choices of

the extensions of x and y in (T,∞). Replacing the integral I_2 in Eq. (4.33) by the corresponding sum

$$I_2 = h\sum_{i=1}^{N}\left[\sum_{k=0}^{n} q_k y^{(k-n)}(ih) - \sum_{k=0}^{m} p_k x^{(k-n)}(ih)\right]^2 \tag{4.35}$$

where $x(t)$ and $y(t)$ are given at points $t=0,h,2h,...,Nh=T$. Next p_k and q_k should be determined as coefficients of linear regression by the least square method. For this purpose, in this thesis, a computer program in Matlab has been written to solve this regression problem.

Golubev's method is powerful as compared to other existing methods (e.g, Graupe, 1972; Eykhoff, 1973) since: (*i*) it can work when plant input-output data are available only over finite time intervals, i.e. [0, T], (*ii*) it determines the transfer function directly, without calculating the Laplace transforms of the input and output signals separately, and (*iii*) it involves only integration of the data and is therefore highly immune to noise.

4.2.2 Derivation of Linear Time-Invariant Equivalent Models

- ***Experimental method***

In this section the equivalent linear time-invariant models are derived based on the experimental data obtained from the test stand shown in Fig. 2.1. The input is the voltage applied to the servovalve and the output is the reading of the force sensor. To extract the acceptable plant outputs, we apply a proportional controller and a second-order prefilter, similar to the configuration shown in Fig. 4.10. The prefilter is inserted to shape the reference input and to prevent the control signal from saturation. For each operating condition, the proportional controller gain is adjusted by trial-and-error to produce responses with acceptable design specifications. The design specifications are to have

settling time of ~1 sec and maximum percent overshoot less than 5% for the compensated system. The acceptable input-output signals are recorded over the following range of parameter changes:

Environmental stiffness	30 to 100 kN/m
Pump supply pressure	500 to 1500 psi
Desired contact force	500 to 1000 N

For practical cases, a limited number of combinations is sufficient. However, these combinations should include the extreme working conditions. Typical experimental responses are shown in Fig. 4.11. For each input-output pair, Golubev's method is applied to directly derive the plant rational transfer function. Using this method, the hydraulic actuator in contact with the environment can be represented by a family of second-order transfer functions having the following form:

$$P_{eq}(s,\alpha) = \frac{\alpha_1}{(s+\alpha_2)(s+\alpha_3)} \tag{4.36}$$

where $\alpha_1 \in 10^4[2.1, 21.5]$, $\alpha_2 \in [0.01, 0.5]$ and $\alpha_3 \in [15.6, 44]$. Bode plots of the above transfer functions are shown in Fig. 4.12.

- ***Nonlinear model-based method***

This method, unlike the experimental one, is based on the mathematical model of the system. A numerical algorithm is presented which, given the desired output, calculates the required input. First a set of acceptable output responses is generated. Then a numerical algorithm is developed, based on the mathematical nonlinear model, to determine the corresponding input set. A simple means for generating acceptable plant responses, $y_a(t)=f_{des}(t)$, is to set

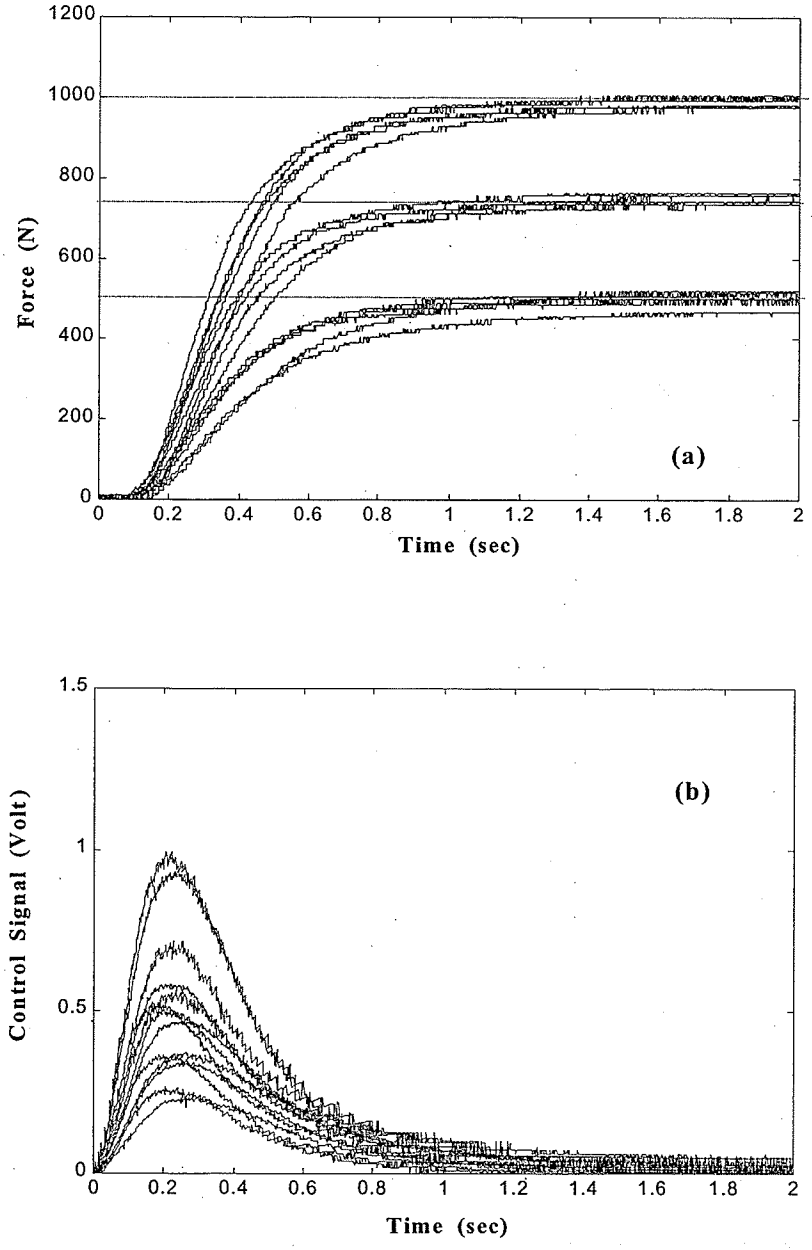

Fig. 4.11: Experimental input-output responses.

$$Y_a(s) = \mathcal{L}[y_a(t)] = \frac{k}{s}T(s) \qquad k \in [500,1000] \tag{4.37}$$

where

$$T(s) = \frac{1}{(1+\frac{s}{a})(1+\frac{9.6}{50}s+\frac{s^2}{50})} \qquad a \in [5,25] \tag{4.38}$$

Note that the acceptable responses generated by (4.37) satisfy the specifications previously set (i.e., 1 sec settling time and 5% maximum overshoot). Fig. 4.13a shows the generated acceptable output derived from (4.37). Assuming a desired contact force trajectory, $f_{des}(t)$, defined by (4.37) on a finite interval $[0,T]$, actuator displacement, $x_{des}(t)$, and the force required by the actuator, $f_a(t)$ can be derived as,

$$x_{des}(t) = \frac{f_{des}(t)}{k_e} = \varphi(t) \tag{4.39}$$

$$f_a(t) = p_i(t)A_i - p_o(t)A_o = m_a\ddot{\varphi}(t) + d\dot{\varphi}(t) + k_e\varphi(t) = \psi(t) \tag{4.40}$$

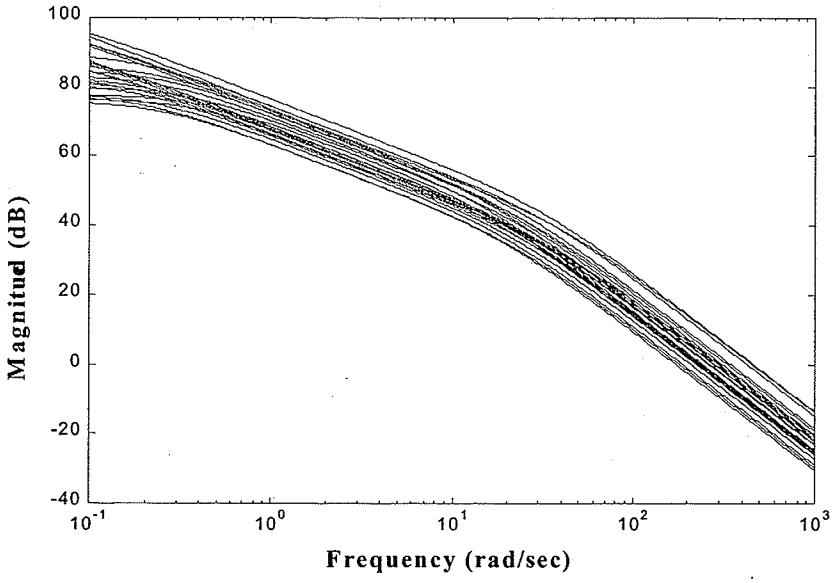

Fig. 4.12: Plant frequency responses obtained from experimental approach.

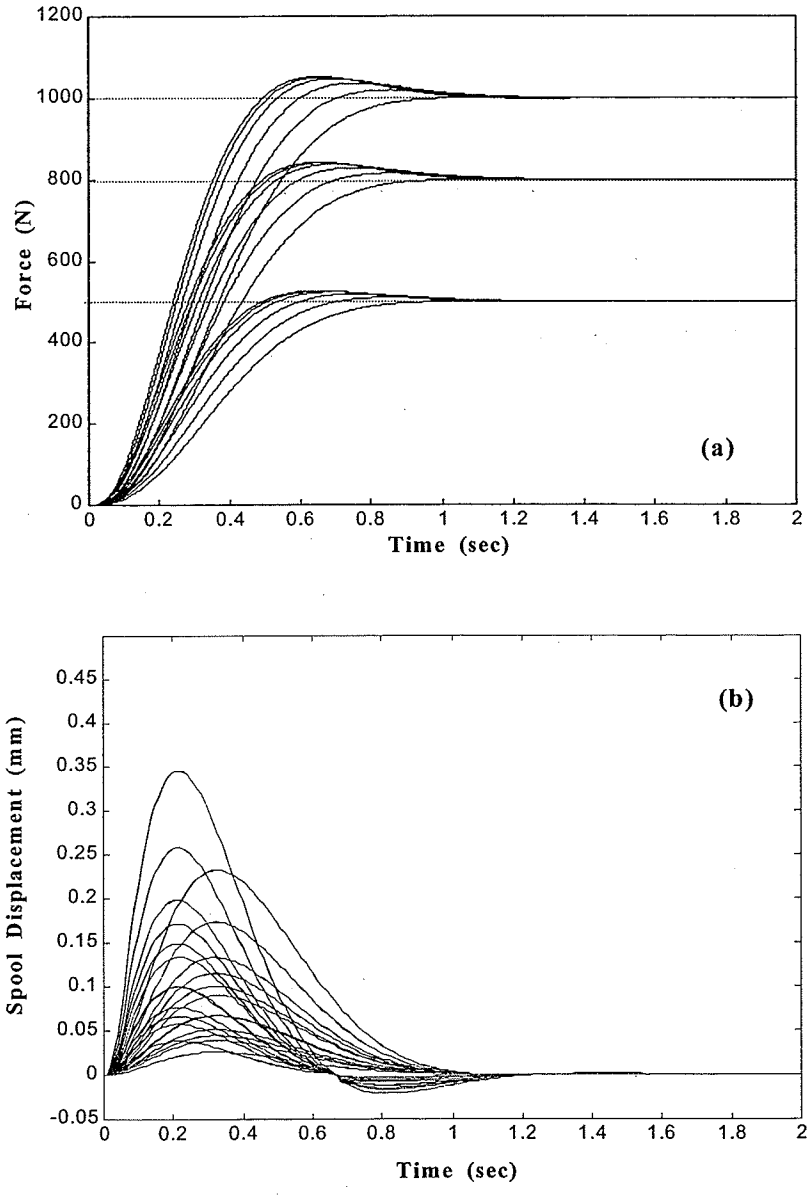

Fig. 4.13: Acceptable plant input-output histories.

Note the above relations hold assuming a pure stiffness environment. From (4.40) one can obtain p_o (dropping t, which denotes the time dependency, for simplicity):

$$p_o = \frac{p_i A_i - \psi}{A_o} \tag{4.41}$$

The relations between q_i and q_o from Eqs. (2.12) are

$$q_i = q_o \frac{\sqrt{(p_s - p_i)}}{\sqrt{(p_o - p_e)}} \qquad (x_{sp} \geq 0) \tag{4.42a}$$

$$q_i = q_o \frac{\sqrt{(p_i - p_e)}}{\sqrt{(p_s - p_o)}} \qquad (x_{sp} < 0) \tag{4.42b}$$

Inserting q_i and q_o from (2.14) into (4.42), substituting p_o with (4.41) and rearranging (4.42) to derive p_i, yields,

$$\begin{aligned} \dot{p}_i &= \frac{\left[\frac{V_o(\varphi)\dot{\psi}}{A_o} + \beta A_o \dot{\varphi}\right]\sqrt{p_s - p_i} - \beta A_i \dot{\varphi}\sqrt{\frac{p_i A_i - \psi}{A_o} - p_e}}{V_i(\varphi)\sqrt{\frac{p_i A_i - \psi}{A_o} - p_e} + \frac{V_o(\varphi) A_i}{A_o}\sqrt{p_s - p_i}} \\ &= \Omega(p_i, \varphi, \dot{\varphi}, \psi, \dot{\psi}) \end{aligned} \qquad (x_{sp} \geq 0) \tag{4.43a}$$

$$\begin{aligned} \dot{p}_i &= \frac{\left[\frac{V_o(\varphi)\dot{\psi}}{A_o} + \beta A_o \dot{\varphi}\right]\sqrt{p_i - p_e} - \beta A_i \dot{\varphi}\sqrt{p_s - \frac{p_i A_i - \psi}{A_o}}}{V_i(\varphi)\sqrt{p_s - \frac{p_i A_i - \psi}{A_o}} + \frac{V_o(\varphi) A_i}{A_o}\sqrt{p_i - p_e}} \\ &= \Omega(p_i, \varphi, \dot{\varphi}, \psi, \dot{\psi}) \end{aligned} \qquad (x_{sp} < 0) \tag{4.43b}$$

Equations (4.43) are solved numerically given any pre-specified contact force trajectory, $f_{des}(t)$. Consequently, p_o, q_i and q_o are obtained from Eqs. (4.41) and (2.14) recursively. The spool displacement is then derived from Eqs. (2.12) as follows:

$$x_{sp} = \frac{q_i}{wc_d\sqrt{\frac{2}{\rho}(p_s - p_i)}} \qquad (x_{sp} \geq 0) \tag{4.44a}$$

$$x_{sp} = \frac{q_i}{wc_d\sqrt{\frac{2}{\rho}(p_i - p_e)}} \qquad (x_{sp} < 0) \tag{4.44b}$$

The required input signal to achieve the desired contact force is determined from Eq. (2.11):

$$u = (\frac{\tau}{k_{sp}})\frac{dx_{sp}}{dt} + (\frac{1}{k_{sp}})x_{sp} \tag{4.45}$$

The above algorithm based on Eqs. (4.43) to (4.45), was examined for different desired output forces, and the uniqueness of the solutions was checked by solving Eqs. (2.1) through (2.15) straightforward. There was excellent agreement between the results of the simulation program and the acceptable plant outputs. Various combinations of the system parameter ranges are shown in Table 4.2.

Table 4.2: Operating values and parameter ranges pertaining to the nonlinear model.

Parameter	Nominal Value		Range
k_e	70	(kN/m)	30-100
d	400	(N/m/sec)	300-500
m_a	10	(kg)	9.9-10.1
A_i	$1.14(10)^{-3}$	(m^2)	$1.11(10)^{-3}$-$1.17(10)^{-3}$
A_o	$0.63(10)^{-3}$	(m^2)	$0.61(10)^{-3}$-$0.65(10)^{-3}$
k_{sp}	$1.45(10)^{-4}$	(m/V)	$1.3(10)^{-4}$-$1.6(10)^{-4}$
τ	30	(msec)	20-40
p_s	1000	(psi)	500-1500
w	$1.0(10)^{-2}$	(m)	$0.95(10)^{-2}$-$1.05(10)^{-2}$
β	$1.0(10)^{9}$	(Pa)	$0.5(10)^{9}$-$1.5(10)^{9}$

Note that the above variations are similar to the experimental approach except that the variation of the fluid bulk modulus is also included. The effective bulk modulus of a hydraulic system could significantly change under various load conditions, oil temperature and air content in the oil (Yu et al., 1994). Acceptable plant inputs, corresponding to acceptable plant outputs generated by Eq. (4.37), are shown in Fig. 4.13b. For each input-output pair, Golubev's method was applied to directly derive a rational transfer function. It was found that the hydraulic actuator in contact with the environment can be represented by a family of second-order transfer functions having the following form:

$$P_{eq}(s,\alpha) = \frac{\alpha_1}{(s+\alpha_2)(s+\alpha_3)} \tag{4.46}$$

where $\alpha_1 \in 10^4[1.7,25.9]$, $\alpha_2 \in [-0.0025,+0.048]$ and $\alpha_3 \in [17.3, 45.6]$. The Bode plots of the family of transfer functions are shown in Fig. 4.14.

For disturbance rejection, D_1, the equivalent models relating the output to disturbance should be derived. In this case, a set of acceptable responses is first defined in the presence of disturbance. The acceptable output is generated as

$$F_{des}(s) = \mathscr{L}[f_{des}(t)] = \frac{k}{s}T(s) \qquad k \in [0,27] \tag{4.47}$$

where

$$T(s) = \frac{s}{(1+\frac{s}{1000})(1+\frac{2\xi}{100}s+\frac{s^2}{100^2})} \qquad \xi \in [1,1.3] \tag{4.48}$$

It is desired that the output due to disturbance to dissipate with a settling time of 0.1 sec. The responses generated by (4.47) are shown in Fig. 4.15. The dynamic equation of the hydraulic actuator will be

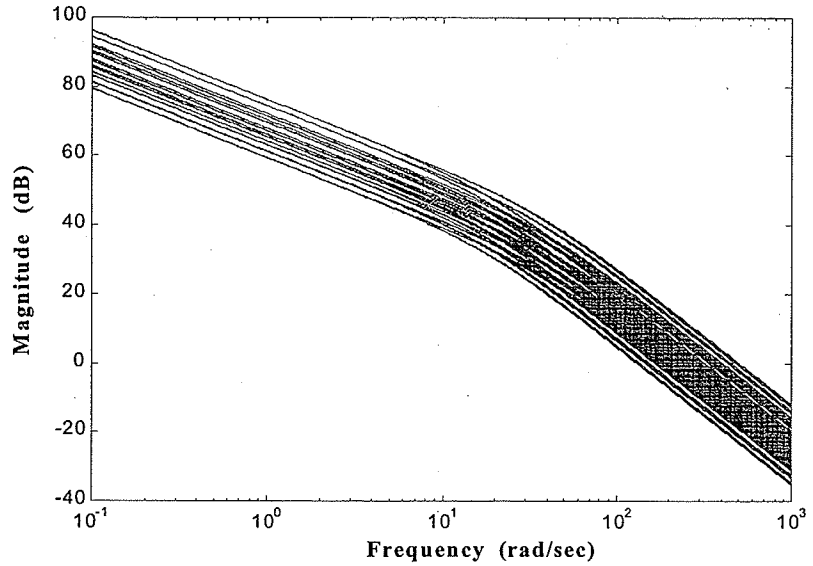

Fig. 4.14: Plant frequency responses obtained from model-based approach.

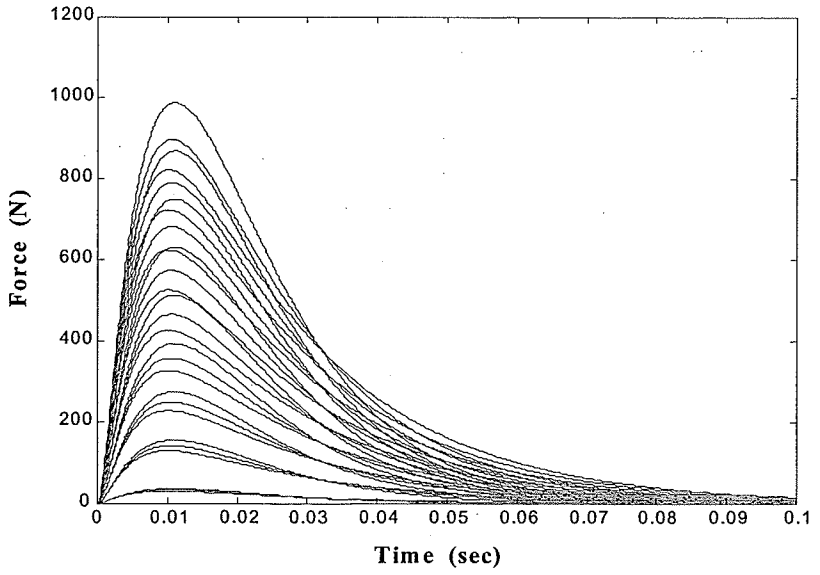

Fig. 4.15: Acceptable responses for disturbance rejection.

$$\bar{f}_a(t) = p_i(t)A_i - p_o(t)A_o - m_a\ddot{x}_{des}(t) - d\dot{x}_{des}(t) - k_e x_{des}(t) \tag{4.49}$$

where

$$x_{des}(t) = \frac{f_{des}(t)}{k_e} \tag{4.50}$$

and $\bar{f}_a$ is the acceptable input force which should be calculated. For the disturbance rejection case, Eqs. (2.14) simplify to (dropping t, which denotes the time dependency, for simplicity):

$$\dot{p}_i = \frac{-\beta A_i}{V_i(x_{des})}\dot{x}_{des} \tag{4.51a}$$

$$\dot{p}_o = \frac{\beta A_o}{V_o(x_{des})}\dot{x}_{des} \tag{4.51b}$$

By substituting (4.51) in (4.49), we have

$$\bar{f}_a = -[\int \frac{\beta A_i^{\,2}}{V_i(x_{des})}\dot{x}_{des}dt - \int \frac{\beta A_o^{\,2}}{V_o(x_{des})}\dot{x}_{des}dt + m_a\ddot{x}_{des} + d\dot{x}_{des} + k_e x_{des}] \tag{4.52}$$

The above equation can be solved numerically for different acceptable outputs, $f_{des}(t)$, and different parameter listed in Table 4.2. For each input-output pair, Golubev's method is applied to directly derive a rational transfer function relating the output to the disturbance input. The equivalent models for this case are found to be

$$P_{d\,eq}(s,\alpha) = \frac{\alpha_1}{s^2 + \alpha_2 s + \alpha_3} \tag{4.53}$$

where $\alpha_1 \in 10^3[3,10]$, $\alpha_2 \in [30,50]$ and $\alpha_3 \in 10^3[8.7, 27.2]$.

We conclude this section with some observations about the results obtained for the equivalent plant sets, based on the two methods. With reference to Eqs. (4.36) and (4.46), both methods have produced similar transfer functions. The range of the open-loop poles,

α, found by the model-based approach, however, includes small positive values. These unstable poles were found when Golubev's method was applied to high velocity responses with overshoots (see Fig. 4.13a). Note that high velocity responses did not appear in our experiments due to the utilization of a proportional controller and the limitation for its adjustment. In the next section, the family of transfer functions found by the model-based approach is used for the controller synthesis.

4.2.3 Controller Synthesis

A strictly proper controller, $G(s)$, and a strictly proper prefilter, $F(s)$, are to be designed such that the constraints (3.2) to (3.5) be satisfied. In Eq. (3.2), M=1.4 which implies an approximate gain margin of 3 dB (according to $GM \geq 1+\frac{1}{M}$) for the closed-loop system stability. The upper and lower bounds shown in Eq. (3.3) are chosen to be the same as the linear method, i.e., Eqs. (4.22). The frequency domain plots of these bounds are given in Fig. 4.17. For the disturbance rejection criteria, the specification is selected to be similar to the linear approach, i.e., Eq. (4.23). In addition, we consider a constant upper bound for disturbance attenuation in Eq. (3.5), $M_{D_2}(\omega)=1.2$, to limit the peak value of the disturbance amplification. The bounds generated by constraints (3.2) to (3.5) are shown in Fig. 4.16, for selected frequencies. The nominal open-loop transfer function, $L_0(s)$, must be shaped to satisfy all of these bounds at each frequency. Furthermore, for the industrial hydraulic actuator under investigation, valve dead-band produces steady-state errors in the system responses in the absence of an integrator factor. To remove the steady-state errors, L_0 should contain an integrator. Hence, a possible loop

can be obtained by cascading an integrator. The final loop shaping of the system (without violating the bounds) is shown in Fig. 4.16. The following controller is proposed:

$$G(s) = \frac{0.04(\frac{s}{3.8}+1)(\frac{s}{38}+1)}{s(\frac{s^2}{185^2}+\frac{2}{185}s+1)} \tag{4.54}$$

The prefilter is designed such that the closed-loop frequency responses lie between the tracking boundaries, $T_l(s)$ and $T_u(s)$. The suitable prefilter is determined as

$$F(s) = \frac{1}{(\frac{s}{6.5}+1)(\frac{s}{6.7}+1)} \tag{4.55}$$

Figure 4.17 shows the closed-loop frequency responses for the equivalent transfer function family. The magnitudes of the disturbance transfer functions are also compared to their corresponding bounds in Figs. 4.18 and 4.19. Note that the closed-loop frequency responses all satisfy the design specifications for the equivalent transfer function family. To evaluate the controller, it should be implemented on the original nonlinear system. The following experimental tests are then performed for this purpose.

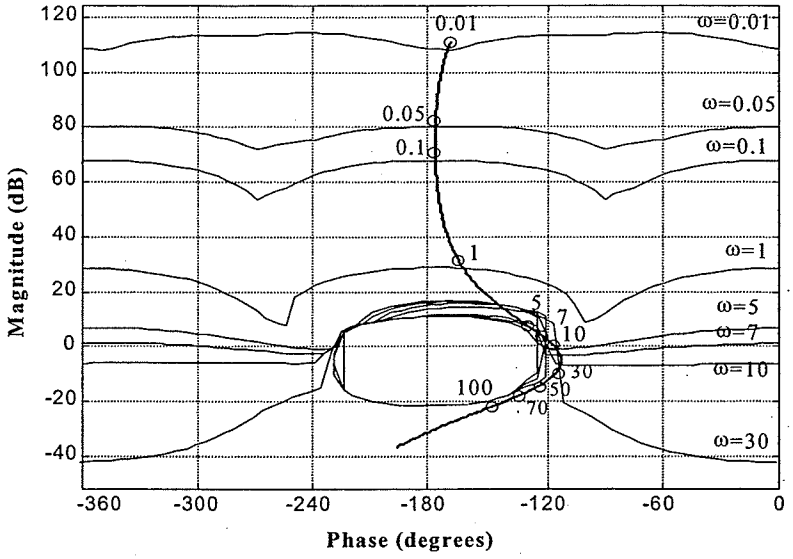

Fig. 4.16: QFT bounds on Nichols chart and nominal loop.

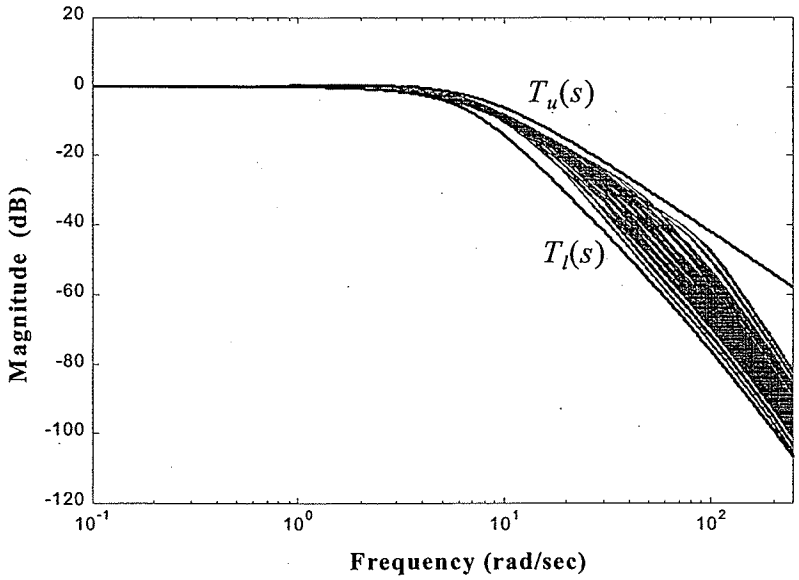

Fig. 4.17: Closed-loop frequency responses over a range of parameter uncertainties.

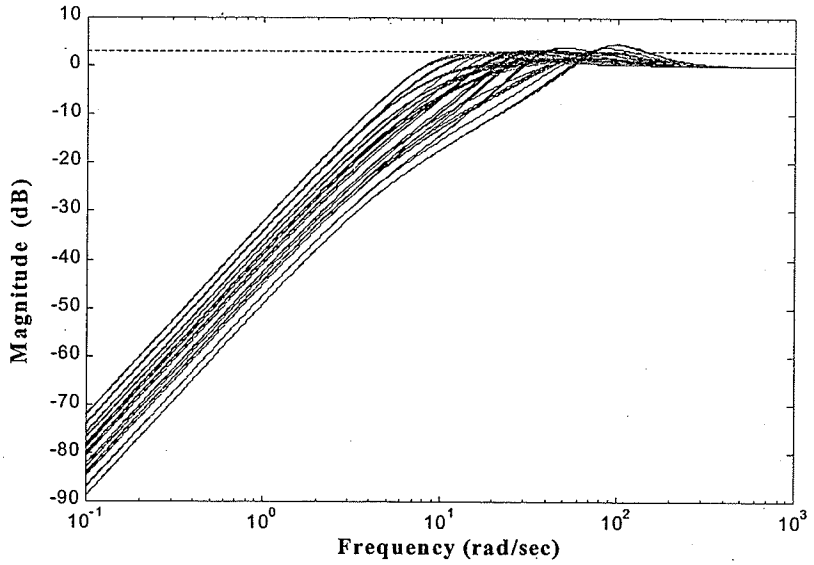

Fig. 4.18: Closed-loop disturbance transfer function and bound, D_2.

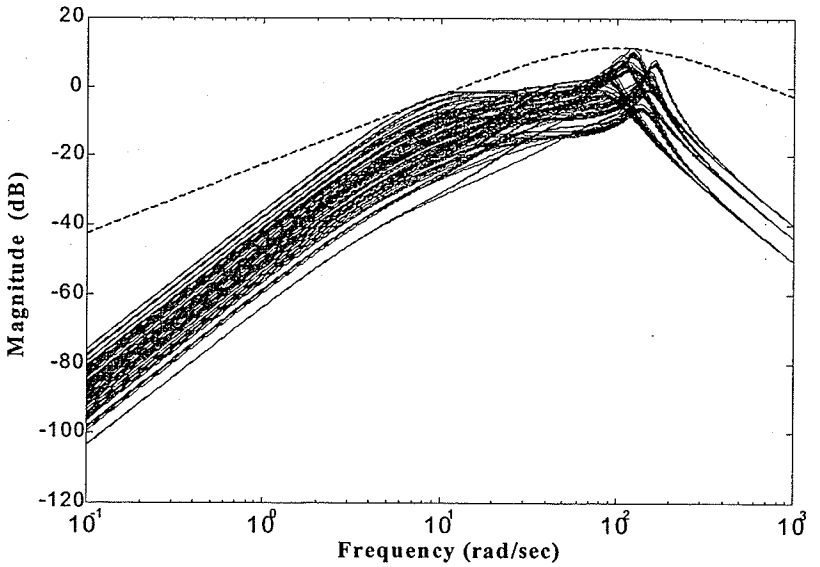

Fig. 4.19: Closed-loop disturbance transfer function and bound, D_1.

4.2.4 Experimental Results

The controller described by (4.54) was implemented on the experimental test rig described in Chapter 2. The effects of variation of environmental stiffness, pump pressure and loading were particularly evaluated. First, the variation of environmental stiffness was tested. Two different environmental stiffnesses of 35 and 100 kN/m were used. The test results are shown in Fig 4.20. In spite of environmental stiffness variation of about 300%, the system responses remained insensitive and the steady-state errors were small. With reference to Fig. 4.20, the experimental results exhibit initial delays mainly due to the valve dead-band and friction. The actuator displacement and the control signal for such a trial are shown in Figs. 4.21 and 4.22, respectively. The control signal is smooth, however it contains high frequency oscillations originating from the noise in the force sensor.

Figure 4.23 compares the test results given three different set-point forces (500 N, 750 N and 1000 N). In spite of changing the loading condition by 100%, the system's performances, i.e. rise time and overshoot, did not change considerably as depicted in Fig. 4.23. The ability of the controller to cope with pump pressure variations was also tested. Typical results are shown in Fig. 4.24, where the pump pressure was varied by 100%. As is seen in Fig. 4.25, control effort is reduced for higher pump pressure.

A test was arranged to investigate the repeatability of the controller and the effect of long term system operation on the response. A 1000 N step response was performed first, and once again after the machine had been in continuous operation for more than one hour. With reference to Fig. 4.26 and Fig. 4.27, there is no noticeable difference between the two responses. Finally, the ability of the control system to follow a step input square

wave function was investigated. With reference to Fig. 4.28, the system displays good tracking performance. It is, however, seen that the response contains slightly higher overshoots in retraction strokes. This phenomenon is mainly due to different piston cross sectional areas, which results in different plant gains for extension and retraction strokes. Note that the design procedure, as outlined here, made no allowance for such a large retraction stroke in the square wave step input. The control signal for this experiment is shown in Fig. 4.29.

4.3 Summary and Comparison

In this chapter, two QFT force controllers were designed based on linear and nonlinear approaches. Both controllers were successfully implemented on the experimental test station and the results were discussed. In the following, these two approaches are further discussed and are compared:

(*i*) In both approaches, a family of transfer functions were derived to describe the system over the uncertainty range. The Bode plots of open-loop transfer functions of the system are shown in Figs. 4.1 and 4.14. Both approaches ended up with similar transfer functions; however, the transfer functions derived from the linear approach include a set of high frequency complex poles. These complex poles were not detected during the system identification based on the nonlinear approach. Indeed, the high frequency complex poles were quite above the system's bandwidth, so that they had no significant effect on the identification results. Consequently, in the nonlinear approach (model-based or experimental), only the part of the system dynamics which had an effect on the design was included in the model. Because of

this, the design procedure became simpler and required less computational effort, especially during the loop shaping, in the nonlinear approach.

(*ii*) The Bode plot of the controllers derived from the linear and nonlinear approaches, i.e., (4.24) and (4.54), are shown in Fig. 4.30. Except for a small gain difference between the two controllers at low frequencies, both controllers matched well at the high frequency range. Higher controller gain based on the linear approach was mainly due to the overestimation of the system gains that form parameters K_s and K_p in Eq. (4.18).

(*iii*) In the nonlinear approach, the nonlinearities and variation in the operating point were incorporated directly into the design procedure. However, in the linear approach, the nonlinearities and the variation in the operating point were considered through uncertainty ranges in parameter K_s and K_p. Therefore, the accuracy and validity of the design in the linear approach are highly dependent on the selection of these parameters. Unfortunately, the identification of these parameters over the large range of variation of operating point is a difficult and time consuming task which needs experience and some design trial-and-error.

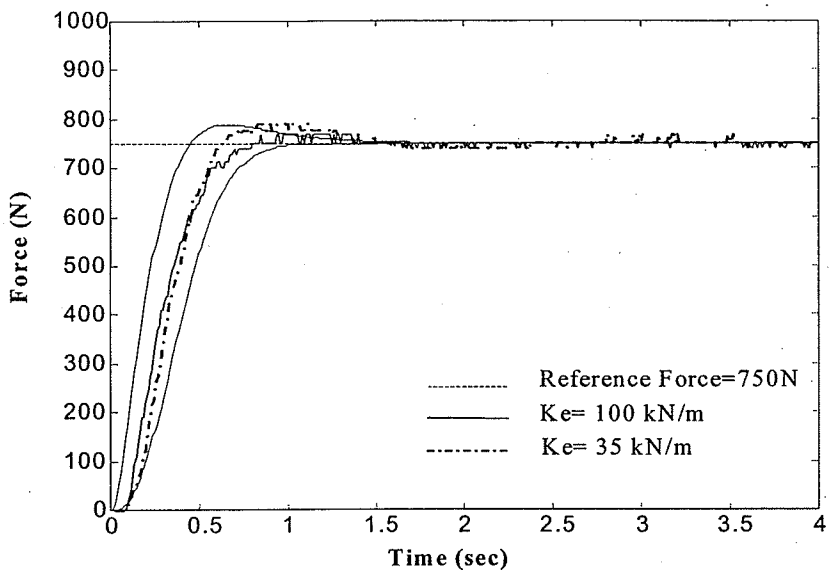

Fig. 4.20: Step responses with different environmental stiffnesses.

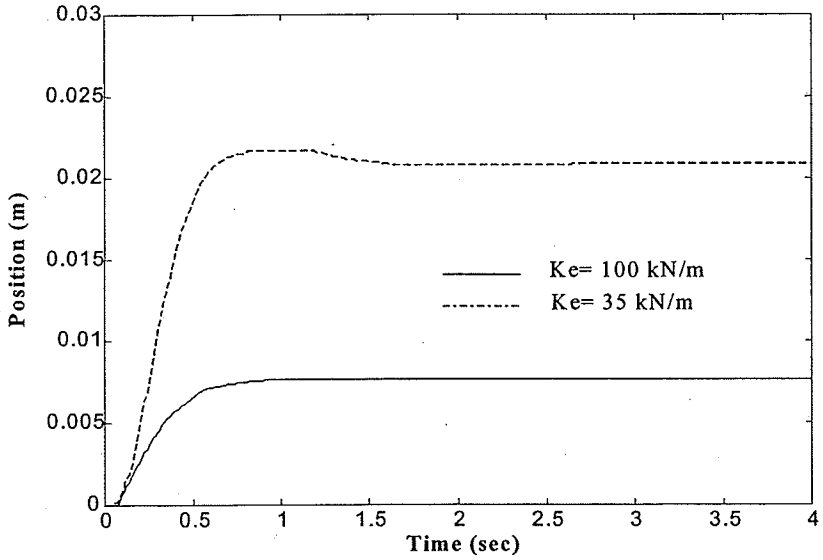

Fig. 4.21: Actuator position pertaining to experiment in Fig. 4.20.

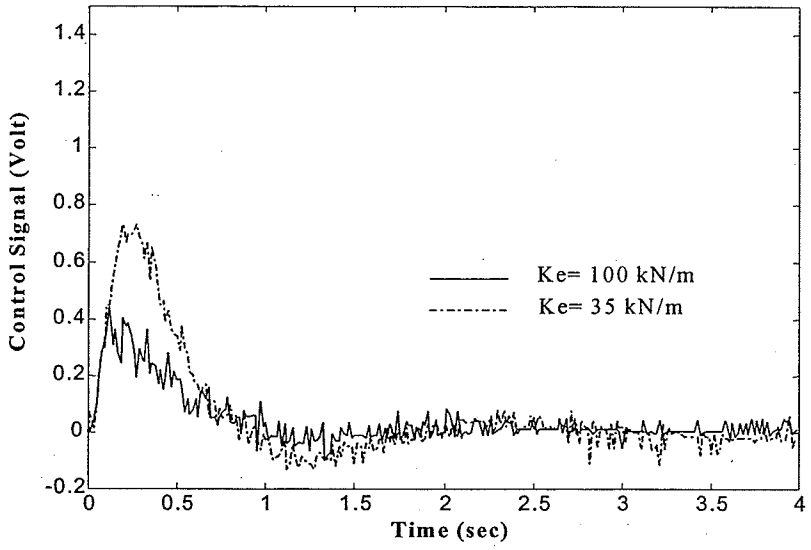

Fig. 4.22: Control signal pertaining to experiment in Fig. 4.20.

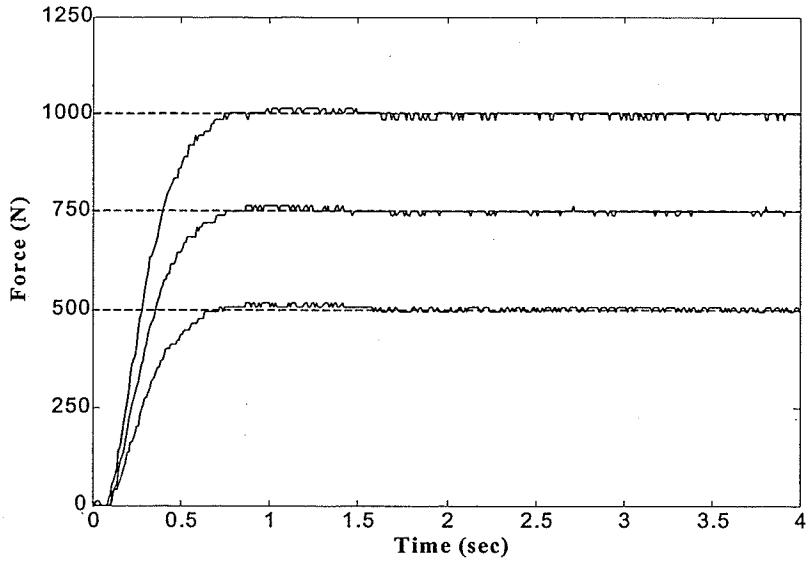

Fig. 4.23: Step force responses for different reference forces.

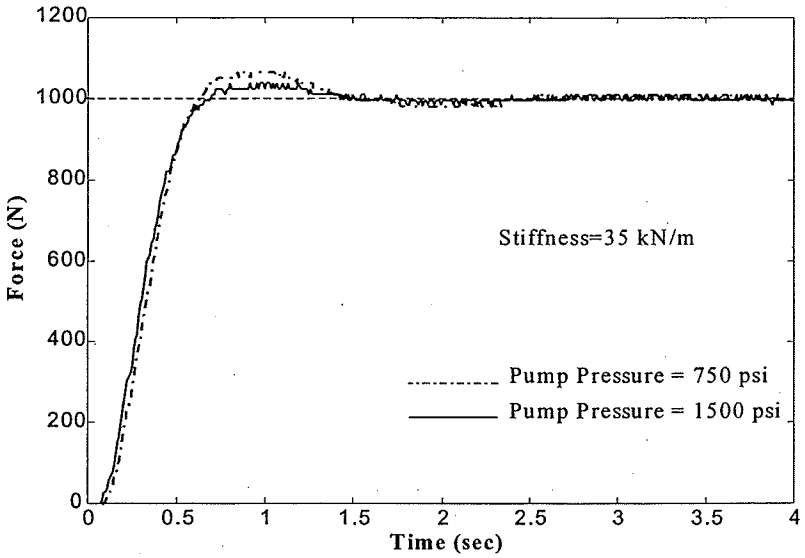

Fig. 4.24: Step force responses for different supply pressures.

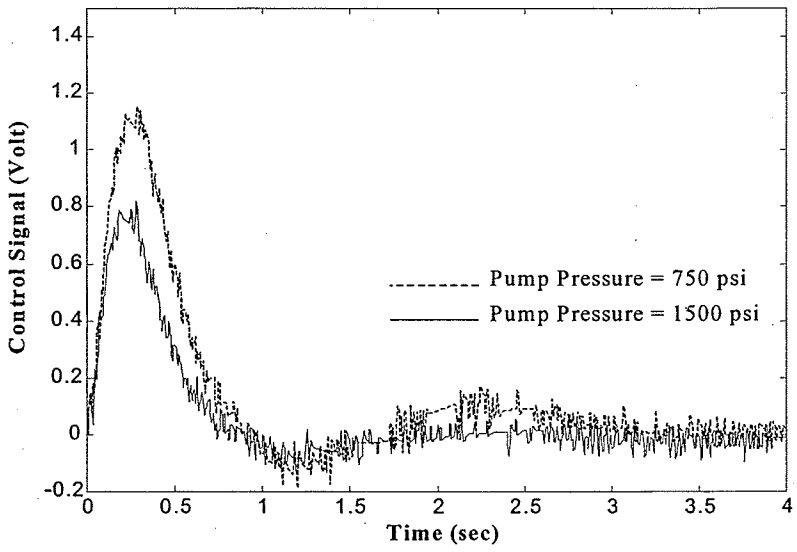

Fig. 4.25: Control signal pertaining to experiment in Fig. 4.24.

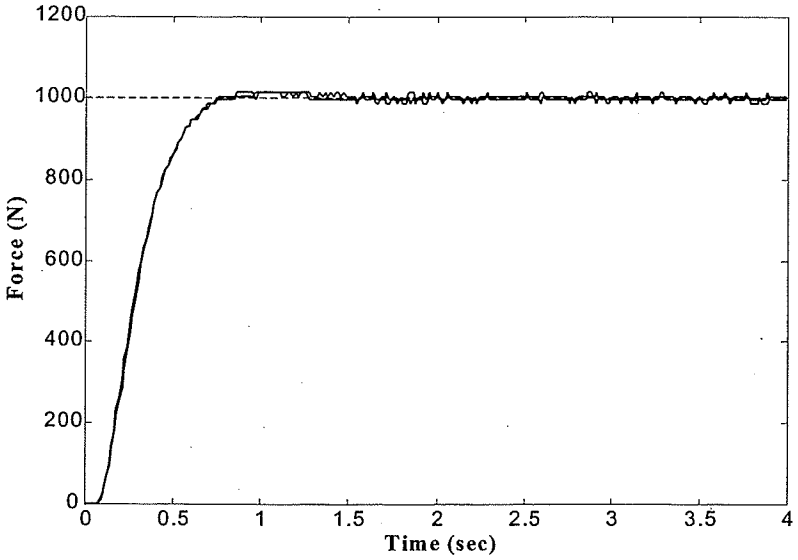

Fig. 4.26: Repeatability test.

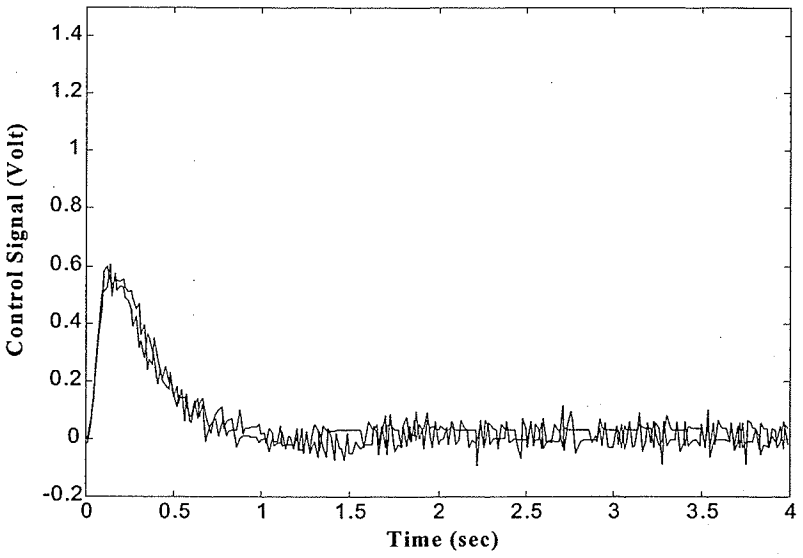

Fig. 4.27: Control signal pertaining to experiment in Fig. 4.26.

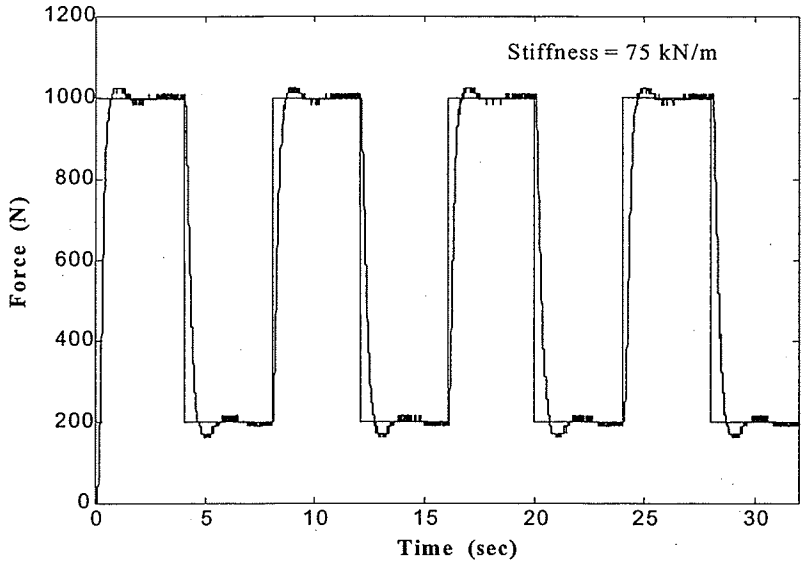

Fig. 4.28: System response to square wave force set-point .

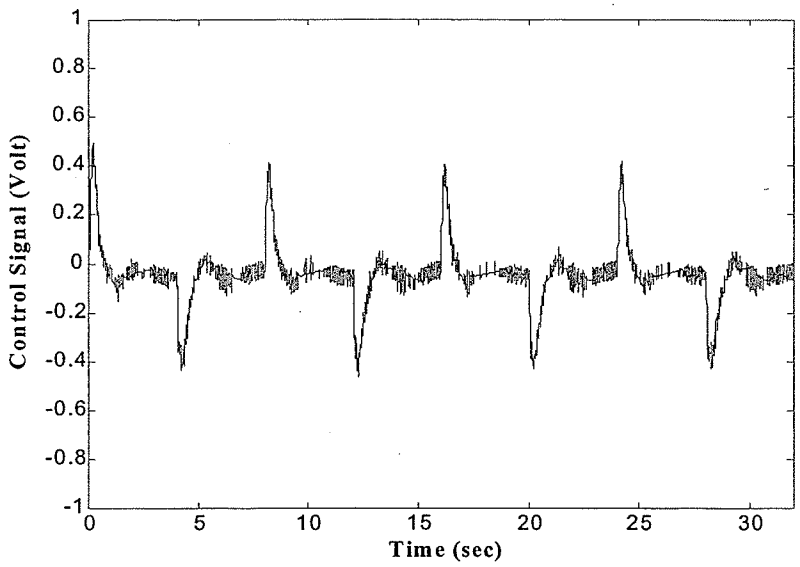

Fig. 4.29: Control signal pertaining to experiment in Fig. 4.28.

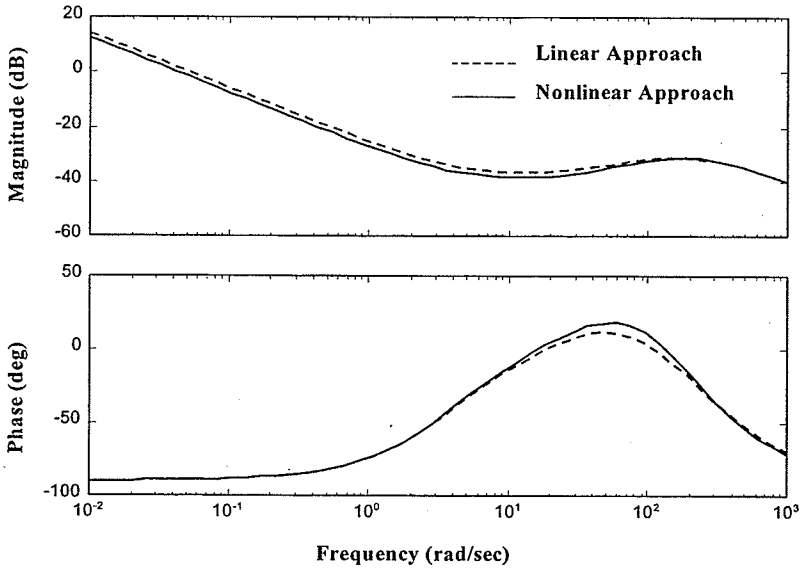

Fig. 4.30: Bode plots of the designed controllers.

Chapter 5

Design of the QFT Position Controller

In this chapter, a QFT position controller will be designed for the hydraulic actuator to manipulate it in free space motion. The nonlinear approach, used for force controller design in Section 4.2, is adapted here for position control design.

5.1 Derivation of the Linear Time-Invariant Equivalent Models

The first step is to generate a set of acceptable input-output pairs, based on the nonlinear mathematical model of the system. An acceptable output response is to have 1 sec settling time and 5% maximum overshoot. A simple means to generate the output response, $x_{des}(t)$, is to set

$$X_{des}(s) = \mathscr{L}[x_{des}(t)] = \frac{k}{s} T(s) \qquad k \in [0.001, 0.05] \tag{5.1}$$

where

$$T(s) = \frac{1}{(1+\frac{s}{a})(1+\frac{9.6}{50}s+\frac{s^2}{50})} \qquad a \in [5,25] \tag{5.2}$$

To calculate the acceptable input set, a numerical algorithm is developed similar to one arrived at in Section 4.2.2. For free space motion of the actuator the dynamic equation of the system can be written as (assuming f_d=0 in Eq. (2.1))

$$m_a \ddot{x}_{des}(t) + d\dot{x}_{des}(t) = p_i(t)A_i - p_o(t)A_o = \psi(t) \tag{5.3}$$

Inserting $x_{des}(t)$ in the above equation and rearranging it to derive p_o (dropping t, which denotes the time dependency, for simplicity) yields:

$$p_o = \frac{p_i A_i - m_a \ddot{x}_{des} - d\dot{x}_{des}}{A_o} \tag{5.4}$$

The relations between q_i and q_o from Eqs. (2.12) are

$$q_i = q_o \frac{\sqrt{(p_s - p_i)}}{\sqrt{(p_o - p_e)}} \qquad (x_{sp} \geq 0) \tag{5.5a}$$

$$q_i = q_o \frac{\sqrt{(p_i - p_e)}}{\sqrt{(p_s - p_o)}} \qquad (x_{sp} < 0) \tag{5.5b}$$

Inserting q_i and q_o from (2.14) into (5.5), substituting p_o with (5.4) and rearranging (5.5) to derive p_i yields

$$\dot{p}_i = \frac{\left[\frac{V_o(x_{des})\dot{\psi}}{A_o} + \beta A_o \dot{x}_{des}\right]\sqrt{p_s - p_i} - \beta A_i \dot{x}_{des}\sqrt{\frac{p_i A_i - \psi}{A_o} - p_e}}{V_i(x_{des})\sqrt{\frac{p_i A_i - \psi}{A_o} - p_e} + \frac{V_o(x_{des})A_i}{A_o}\sqrt{p_s - p_i}} \qquad (x_{sp} \geq 0) \tag{5.6a}$$

$$= \Omega(p_i, x_{des})$$

$$\dot{p}_i = \frac{\left[\frac{V_o(x_{dex})\dot{x}_{des}}{A_o} + \beta A_o \dot{x}_{des}\right]\sqrt{p_i - p_e} - \beta A_i \dot{x}_{des}\sqrt{p_s - \frac{p_i A_i - \psi}{A_o}}}{V_i(x_{dex})\sqrt{p_s - \frac{p_i A_i - \psi}{A_o}} + \frac{V_o(x_{dex})A_i}{A_o}\sqrt{p_i - p_e}} \qquad (x_{sp} < 0) \tag{5.6b}$$

$$= \Omega(p_i, x_{dex})$$

Equations (5.6) can be solved numerically given any pre-specified trajectory, $x_{des}(t)$. Consequently, p_o, q_i and q_o are obtained from Eqs. (5.4) and (2.14) recursively. The spool displacement is then derived from Eqs. (2.12) as follows:

$$x_{sp} = \frac{q_i}{wc_d\sqrt{\frac{2}{\rho}(p_s - p_i)}} \qquad (x_{sp} \geq 0) \tag{5.7a}$$

$$x_{sp} = \frac{q_i}{wc_d\sqrt{\frac{2}{\rho}(p_i - p_e)}} \qquad (x_{sp} < 0) \tag{5.7b}$$

The required input signal to achieve the desired contact force is then determined from Eq. (2.11):

$$u = (\frac{\tau}{k_{sp}})\frac{dx_{sp}}{dt} + (\frac{1}{k_{sp}})x_{sp} \tag{5.8}$$

Equations (5.6) to (5.8) were solved numerically for various combinations of the system parameters listed in Table 5.1. Typical acceptable responses, generated by the proposed algorithm, are shown in Fig. 5.1. For each input-output pair, Golubev's method was applied to directly derive a rational transfer function. It was found that the hydraulic actuator during free space motion could be represented by the following transfer functions:

$$P_{eq}(s,\alpha) = \frac{\alpha_1}{(s+\alpha_2)(s+\alpha_3)} \tag{5.9}$$

where $\alpha_1 \in [0.77, 4.1]$, $\alpha_2 \in [-0.0076, +0.027]$ and $\alpha_3 \in [16.7, 44.3]$. The Bode plots of the family of transfer functions are shown in Fig. 5.2.

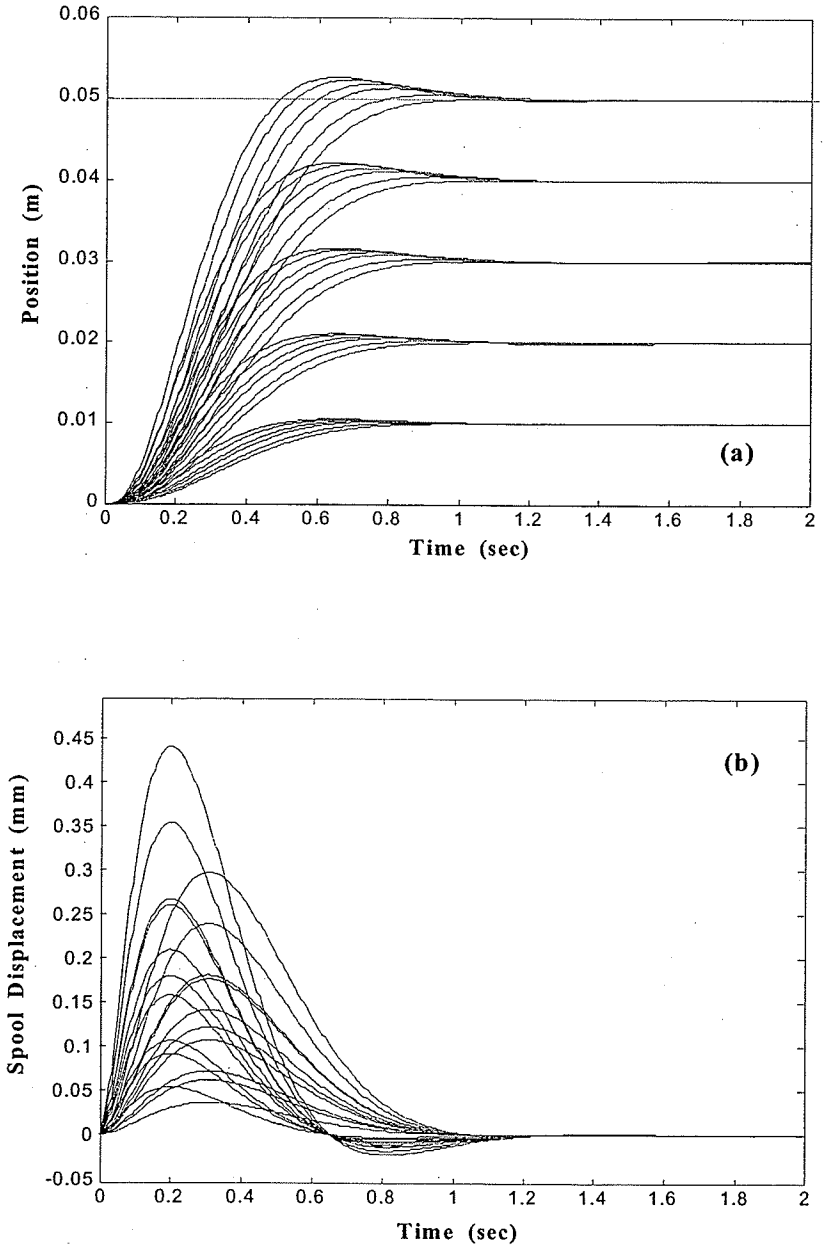

Fig. 5.1: Acceptable plant input-output histories for position controller design.

Table 5.1: Operating values and parameter ranges.

Parameter	Nominal Value		Range
d	400	(N/m/sec)	300-500
m_a	10	(kg)	9.9-10.1
A_i	$1.14(10)^{-3}$	(m^2)	$1.11(10)^{-3}$-$1.17(10)^{-3}$
A_o	$0.63(10)^{-3}$	(m^2)	$0.61(10)^{-3}$-$0.65(10)^{-3}$
k_{sp}	$1.45(10)^{-4}$	(m/V)	$1.3(10)^{-4}$-$1.6(10)^{-4}$
τ	30	(msec)	20-40
p_s	1000	(psi)	500-1500
w	$1.0(10)^{-2}$	(m)	$0.9(10)^{-2}$-$1.1(10)^{-2}$
β	$1.0(10)^{9}$	(Pa)	$0.5(10)^{9}$-$1.5(10)^{9}$

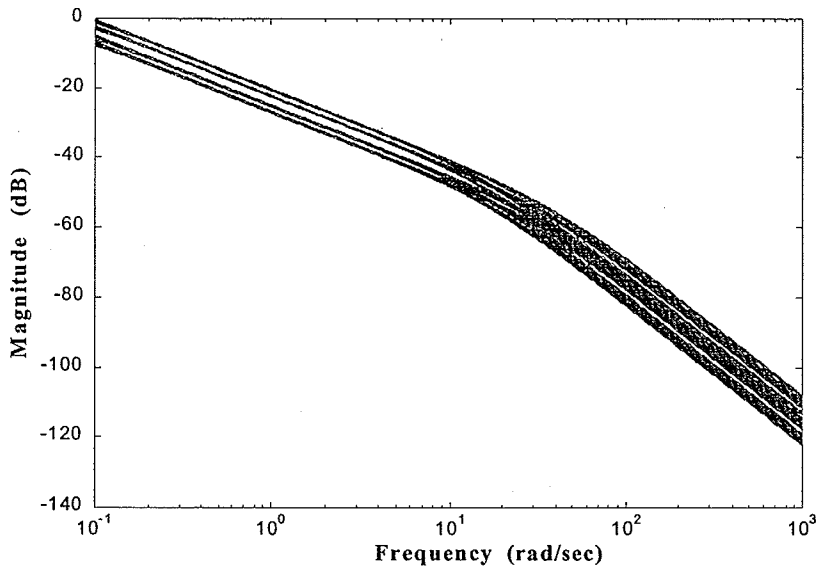

Fig. 5.2: Plant frequency domain responses.

For the disturbance rejection, the equivalent models relating the output to disturbance should be derived. In this case, a set of acceptable responses is first defined in the presence of disturbance. The acceptable output is generated as

$$X_{des}(s) = \mathcal{L}[x_{des}(t)] = \frac{k}{s}T(s) \qquad k \in [-1.6, 1.6] \tag{5.10}$$

and

$$T(s) = \frac{10^{-4}s}{(1+\frac{s}{1000})(1+\frac{2\xi}{50}s+\frac{s^2}{50^2})} \qquad \xi \in [1.3, 1.7] \tag{5.11}$$

It is desired that the system's response to disturbance is dissipated within a settling time of 0.25 sec. The dynamic equation of the hydraulic actuator will be (f=0 in Eq. (2.1)),

$$\bar{f}_a(t) = p_i(t)A_i - p_o(t)A_o - m_a\ddot{x}_{des}(t) - d\dot{x}_{des}(t) \tag{5.12}$$

where $\bar{f}_a$ is the input force which should be calculated. For the disturbance rejection case, the Eqs. (2.14) simplify to (dropping t, which denotes the time dependency, for simplicity)

$$\dot{p}_i = \frac{-\beta A_i}{V_i(x_{des})}\dot{x}_{des} \tag{5.13a}$$

$$\dot{p}_o = \frac{\beta A_o}{V_o(x_{des})}\dot{x}_{des} \tag{5.13b}$$

By substituting (5.13) in (5.12) we have,

$$\bar{f}_a = -[\int \frac{\beta A_i^2}{V_i(x_{des})}\dot{x}_{des}dt - \int \frac{\beta A_o^2}{V_o(x_{des})}\dot{x}_{des}dt + m_a\ddot{x}_{des} + d\dot{x}_{des}] \tag{5.14}$$

The above equation is solved numerically for different acceptable outputs, $x_{des}(t)$, and different parameters listed in Table 5.1. For each input-output pair, Golubev's method is

applied to directly derive a rational transfer function relating the output to the disturbance input. The equivalent models for this case are found to be

$$P_{deq}(s,\alpha) = \frac{0.1}{s^2 + \alpha_1 s + \alpha_2} \tag{5.15}$$

where $\alpha_1 \in [30,50]$ and $\alpha_2 \in 10^3[\,5.7,17.2\,]$.

5.2 Controller Design

A position controller, $G(s)$, and a prefilter, $F(s)$, should be designed to satisfy the following specifications

(*i*) Closed-loop robust stability

$$|T(j\omega,\alpha)| = \left|\frac{L(j\omega,\alpha)}{1+L(j\omega,\alpha)}\right| \le 1.4 \qquad \forall \omega \in [0,\infty) \tag{5.16}$$

where $L(s,\alpha) = P_{eq}(s,\alpha)G(s)$ is the open-loop transfer function.

(*ii*) Robust reference input

For tracking performance requirement, the controller should satisfy the following inequality:

$$\left|\frac{1}{(\frac{j\omega}{4.8}+1)(\frac{j\omega}{80}+1)(\frac{(j\omega)^2}{50}+\frac{9.6j\omega}{50}+1)}\right| \le |F(j\omega)T(j\omega,\alpha)| \le \left|\frac{(\frac{j\omega}{2.8}+1)}{(\frac{j\omega}{4}+1)(\frac{j\omega}{7}+1)(\frac{j\omega}{8}+1)}\right| \quad \forall \omega \in [0,\infty) \tag{5.17}$$

The upper and lower tracking bounds impose 5% maximum percentage of overshoot and about 1 sec settling time.

(*iii*) Disturbance rejection, D_I

It is desired that the output decays to 2 percent of the maximum value in less than 0.25 sec. Therefore, the requirement for disturbance rejection is expressed as

$$\max_{\alpha\in\Omega}|T_D(j\omega,\alpha)| \le \left|\frac{8.75\times10^{-3}\,j\omega}{(j\omega)^2+3.4(j\omega)+1}\right| \qquad \forall\omega\in[0,\infty) \tag{5.18}$$

where $T_D(s,\alpha)=\dfrac{P_{deq}(s,\alpha)}{1+L(s,\alpha)}$ is the transfer function from the disturbance to the output.

(*vi*) Disturbance rejection at plant output, D_2

For sensitivity reduction over the specified bandwidth, an upper bound is imposed on the sensitivity function as follows:

$$\max_{\alpha\in\Omega}|S(j\omega,\alpha)| = \left|\frac{1}{1+L(j\omega,\alpha)}\right| \le 1.2 \qquad \forall\omega\in[0,10] \tag{5.19}$$

The bounds generated by constraints (5.16) to (5.19) are shown in Fig. 5.3 for selected frequencies. The nominal open-loop transfer function, L_0(s), must shape to satisfy all of these bounds at each frequency. Furthermore, for the industrial hydraulic actuator under investigation, valve dead-band produces steady-state errors in the system responses in the absence of an integrator factor. To remove the steady-state errors, L_0 should contain an integrator. Hence, a possible loop can be obtained by cascading an integrator. The final loop shaping of the system (without violating the bounds) is shown in Fig. 5.3. The following controller is proposed:

$$G(s)=\frac{470(\frac{s}{2.9}+1)(\frac{s}{38}+1)}{s(\frac{s^2}{60^2}+\frac{0.9}{60}s+1)} \tag{5.20}$$

The prefilter is designed such that the closed-loop frequency responses lie between the tracking boundaries, $T_l(s)$ and $T_u(s)$. The suitable prefilter is determined as

$$F(s)=\frac{(\frac{s}{65}+1)}{(\frac{s}{3.8}+1)(\frac{s}{25}+1)} \tag{5.21}$$

Figure 5.4 shows the closed-loop frequency responses for the equivalent transfer function family. The magnitudes of the disturbance transfer functions are also compared to their corresponding bounds in Fig. 5.5 and Fig. 5.6. To evaluate the controller, the following experimental tests are then performed on the original nonlinear system.

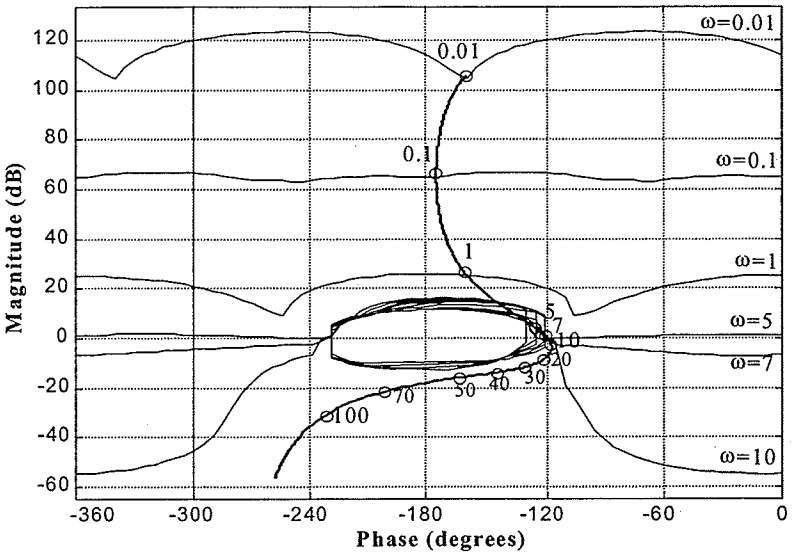

Fig. 5.3: QFT bounds on Nichols chart and nominal loop for position controller design.

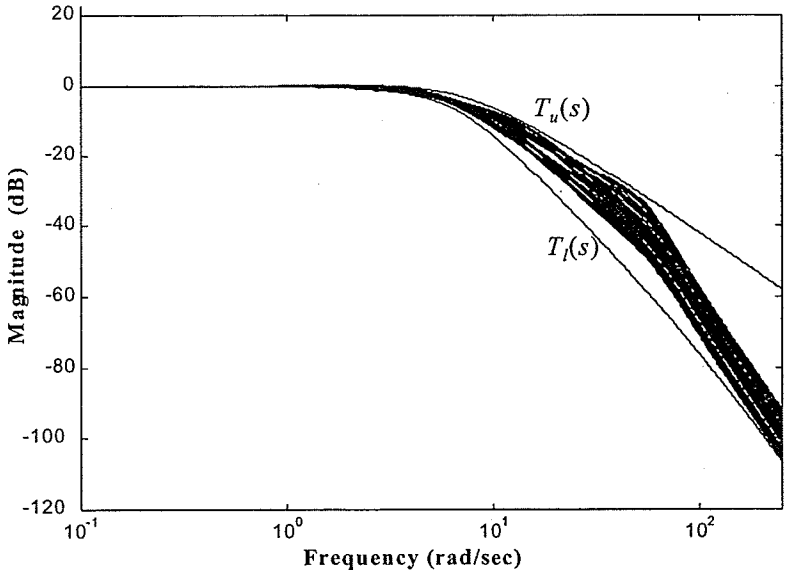

Fig. 5.4: Closed-loop frequency responses over range of parameter uncertainties.

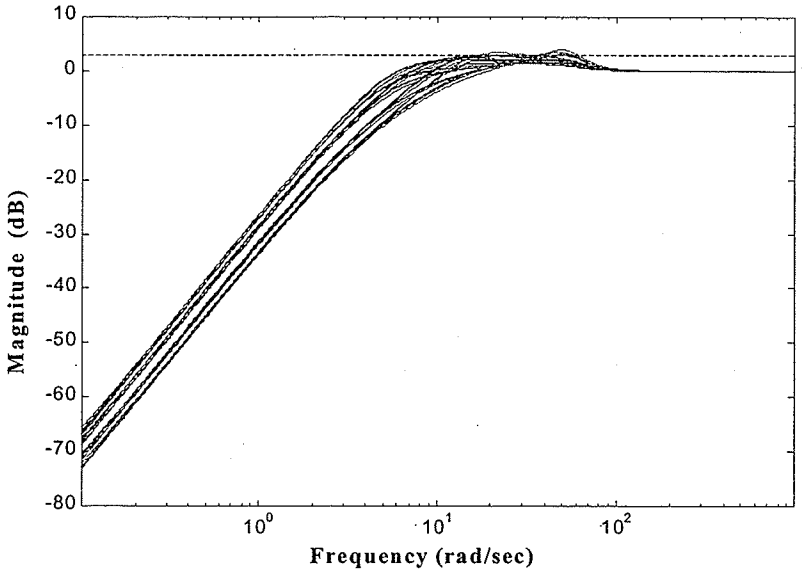

Fig. 5.5: Closed-loop disturbance transfer function and bound, D_2.

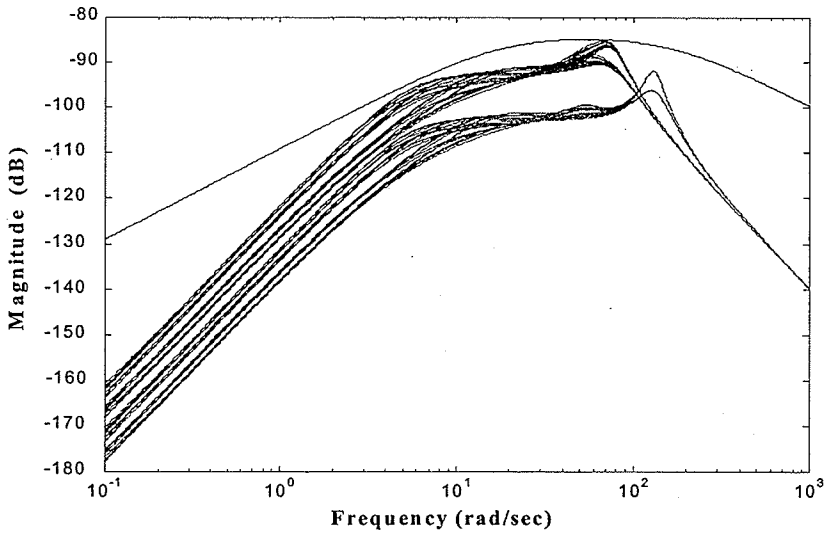

Fig. 5.6: Closed-loop disturbance transfer function and bound, D_1.

5.3 Experimental Results

Figure 5.7 shows the step response of the QFT controller when a position command of 30 mm was applied. Both the upper and lower tracking bounds are shown in dotted lines. The desired settling time and maximum percentage of overshoot are achieved with the robust controller. The velocity of the actuator is shown in Fig. 5.8, which has a maximum of 75 mm/sec. The control signal during the experiment, depicted in Fig. 5.9, is far below the saturation limit. Pump pressure during this experiment is depicted in Fig. 5.10.

Experiments were also run for different levels of command inputs. As is clearly observed in Fig 5.11, the wide range of command inputs have little effect on the transient responses and, at the same time, there are no visible steady state errors on the responses. The performance of the controller was further examined during variation in pump pressure. As shown in Fig 5.12, the variation of the pressure from 1500 psi to 750 psi has no effect on the responses. However, its effect can be seen from the control signals (Fig. 5.13)

Figure 5.14 shows the case when a load disturbance was applied to the actuator. In this experiment, the disturbance force is generated by a spring mounted under the ram. The disturbance load of cycling type (see Fig. 5.15) varies between 600 N to 1400 N. Considering the steady-state accuracy as well as the transient response, the actuator is sufficiently robust to external disturbance. Its control signal is shown in Fig. 5.16.

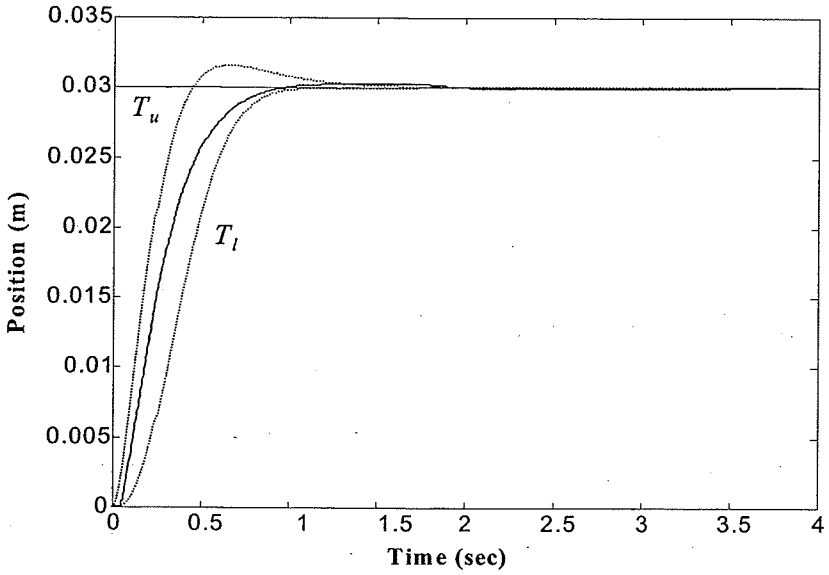

Fig. 5.7: Step response of QFT position controller.

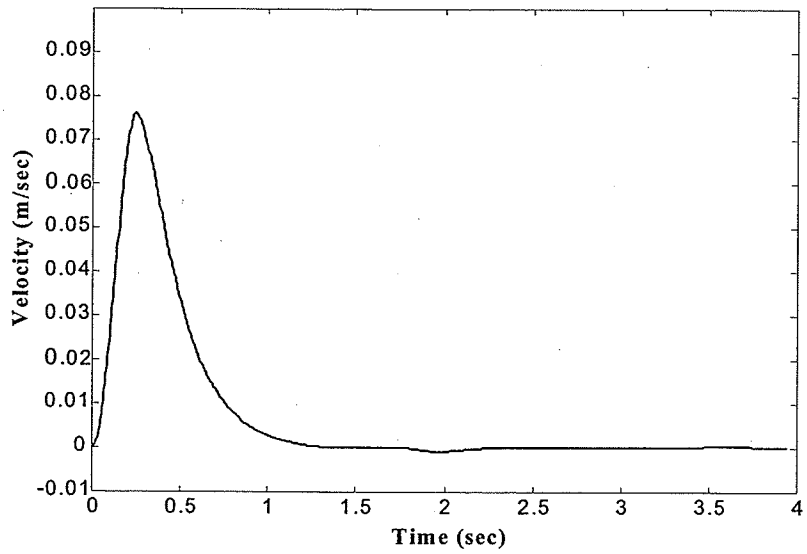

Fig. 5.8: Actuator velocity pertaining to experiment in Fig. 5.7.

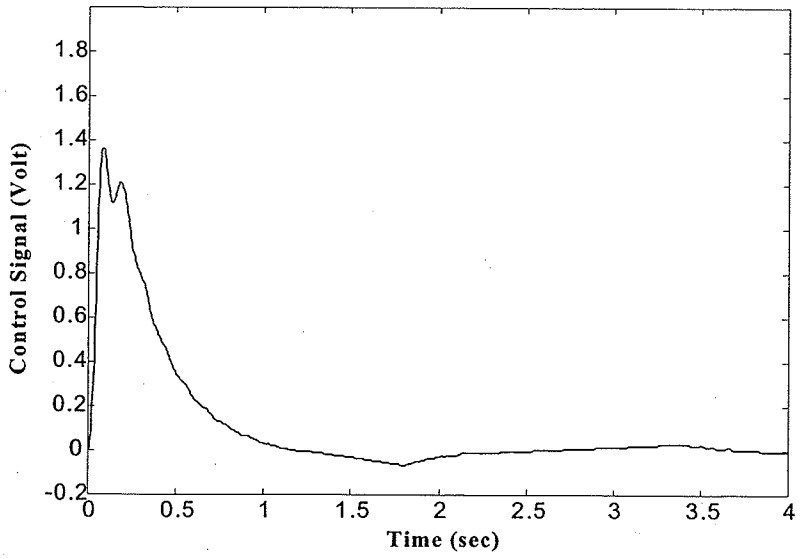

Fig. 5.9: Control signal pertaining to experiment in Fig. 5.7.

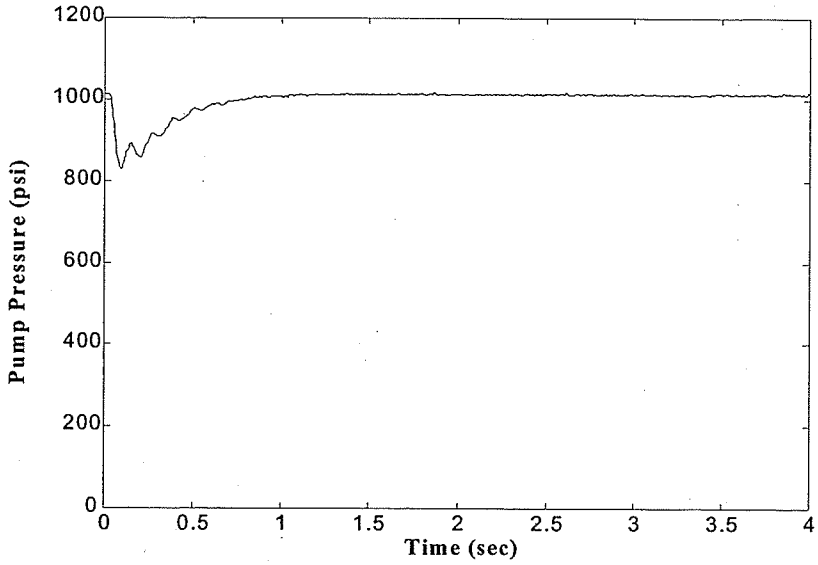

Fig. 5.10: Pump pressure pertaining to experiment in Fig. 5.7.

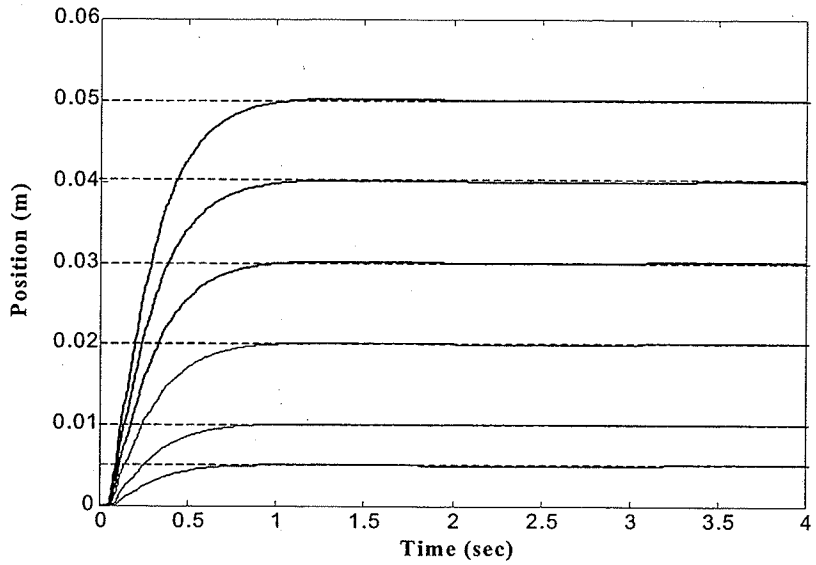

Fig. 5.11: Step responses with different command inputs.

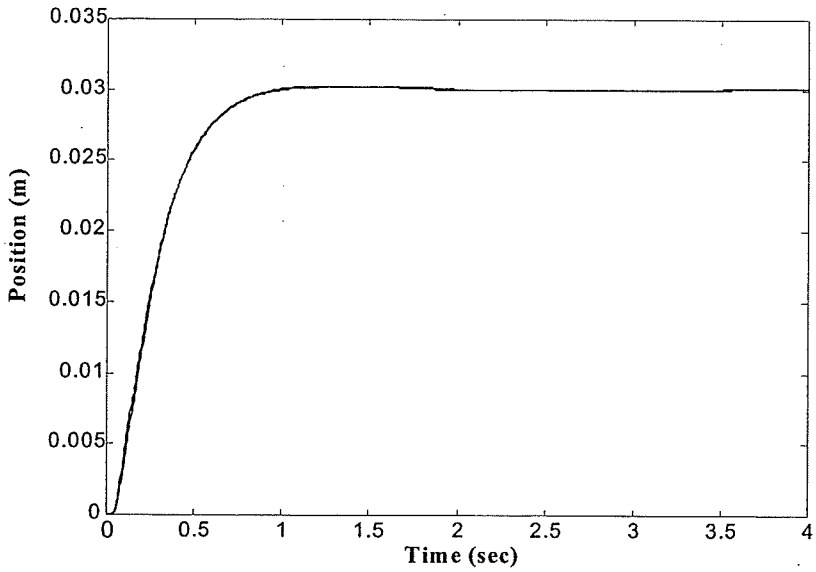

Fig. 5.12: Step responses when pump pressure variations exist.

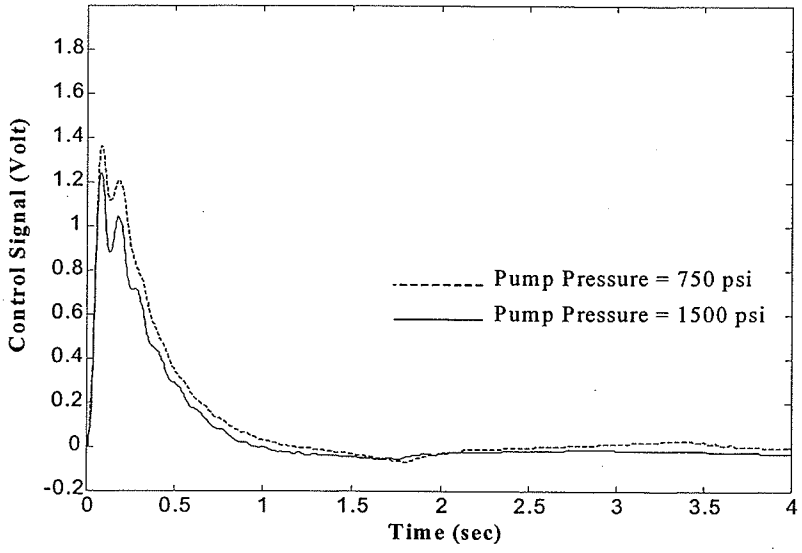

Fig. 5.13: Control signal pertaining to experiment in Fig. 5.12.

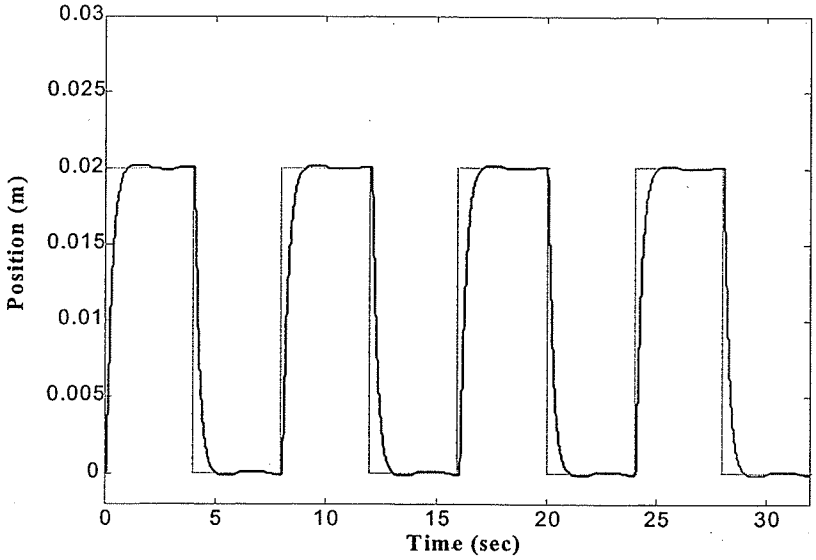

Fig. 5.14: System response under disturbance load.

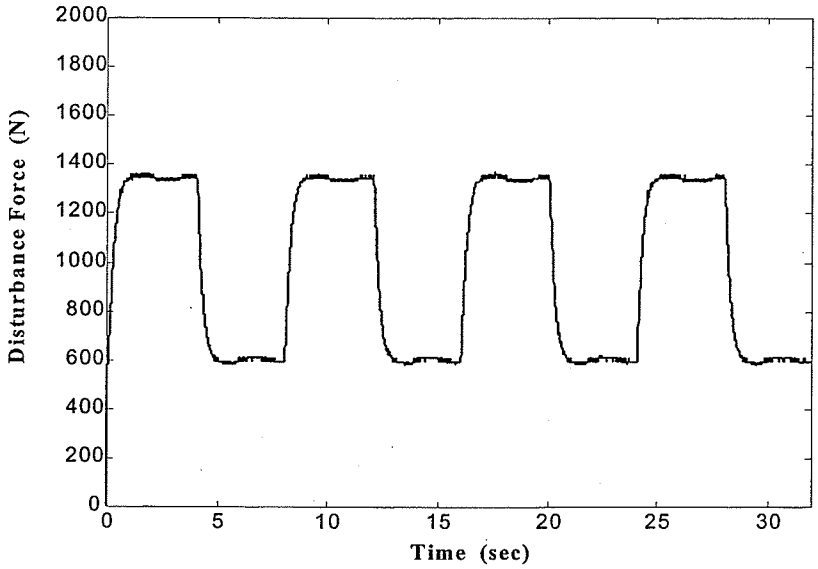

Fig. 5.15: Disturbance force pertaining to experiment in Fig. 5.14.

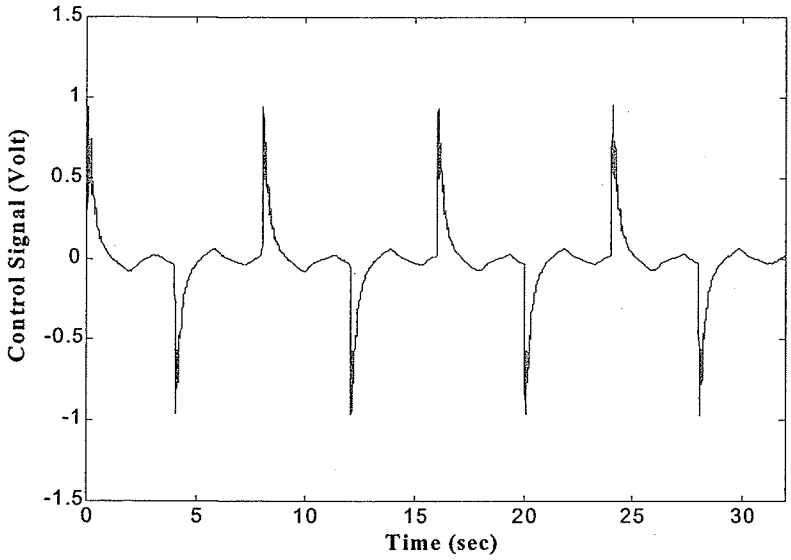

Fig. 5.16: Control signal pertaining to experiment in Fig. 5.14.

Chapter 6

QFT Contact Task Controller

The goal of this chapter is to combine the position controller and the force controller designed previously to construct a contact task controller. Therefore, a switching control law is proposed to move the actuator in both free space and constrained space and simultaneously be robust to system and environmental uncertainties.

6.1 Construction of the Contact Controller

The objective is to construct a controller (*i*) to be robust in the presence of uncertainties and satisfy the performance requirements, and (*ii*) to guarantee the stability of contact during the transition phase. The robustness and performance of the designed position and force controllers were shown previously. The following simple strategy is proposed for the transition between free space and constrained motion: while in free space, use the position control law given in (5.20). Upon the contact, switch to the force control law given by (4.54) in the constrained space:

$$G_c(s) = \begin{cases} G_p(s) = \dfrac{470(\frac{s}{2.9}+1)(\frac{s}{38}+1)}{s(\frac{s^2}{60^2}+\frac{0.9}{60}s+1)} \\ G_f(s) = \dfrac{0.04(\frac{s}{3.8}+1)(\frac{s}{38}+1)}{s(\frac{s^2}{185^2}+\frac{2}{185}s+1)} \end{cases} \tag{6.1}$$

The prefilter is constructed from (5.21) and (4.55):

$$F_c(s) = \begin{cases} F_p(s) = \dfrac{(\frac{s}{65}+1)}{(\frac{s}{3.8}+1)(\frac{s}{25}+1)} \\ F_f(s) = \dfrac{1}{(\frac{s}{6.5}+1)(\frac{s}{6.7}+1)} \end{cases} \tag{6.2}$$

where subscript c denotes contact, and subscripts p and f denote position and force, respectively.

Contact detection utilizes the measurement of interaction forces. When the force measurement, f_c, is greater than or equal to f_{sw}, the controller is switched to force control; otherwise, the controller is maintained in position control. The minimum detectable force, f_{sw}, is dependent upon the sensitivity of the force sensor used in the experiment. The schematic diagram of the switching system is shown in Fig. 6.1.

6.2 Stability Analysis of the Contact Controller

The stability of the QFT force and position control systems are satisfied separately based on the Fixed Point theorem (Horowitz, 1978; Banos and Bailey, 1996). For the contact task controller, however, the discontinuity arising from the switching controller causes the dynamic system under investigation to become non-smooth. This non-ideal phenomenon hampers utilization of any conventional stability theory. In this thesis, the method used by Niksefat et al. (2001b) is adopted for stability analysis. This method is based on an extended version of Lyapunov's second method for stability analysis of non-smooth systems, under the condition of existence and uniqueness of Filippov's solution (Wu and Sepehri, 2001). In this section, state space equations of the system under investigation are first derived. Next, the proof of the existence and uniqueness of Filippov's solution for the system is outlined. Finally, the stability of the system is discussed based on the extended version of Lyapunov's theorem.

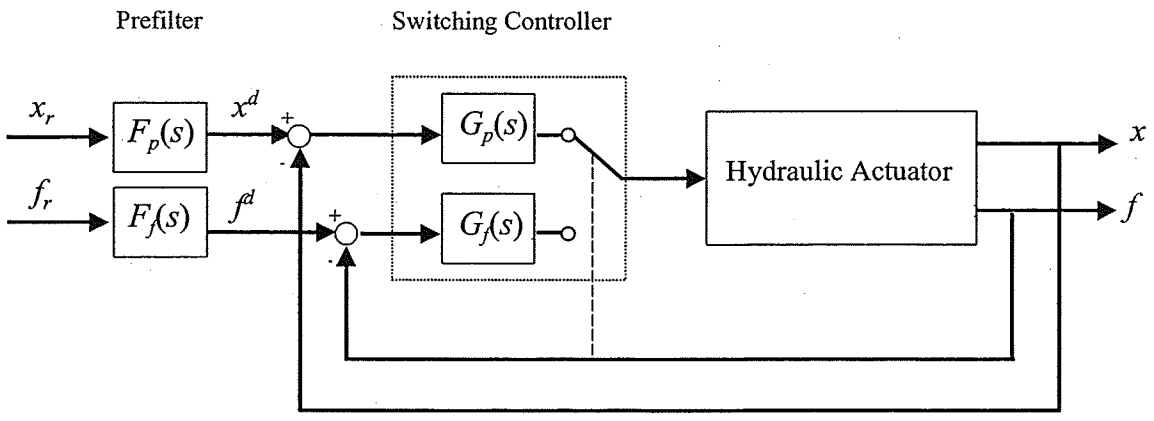

Fig. 6.1: Block diagram of QFT contact controller.

6.2.1 State Space Equations

The nonlinear equations arrived at in Chapter 2 are rearranged here in state space form to be suitable for stability analysis.

• **Non-contact State**

The differential equations during the non-contact state are:

$$\begin{cases} \ddot{x} = \dfrac{A_i}{m} p_i - \dfrac{A_o}{m} p_o - \dfrac{d}{m}\dot{x} \\ \dot{p}_i = -\dfrac{\beta A_i}{V_i(x)}\dot{x} + \dfrac{\beta c_d w}{V_i(x)}\Delta_i(p_i)x_{sp} \\ \dot{p}_o = \dfrac{\beta A_o}{V_o(x)}\dot{x} - \dfrac{\beta c_d w}{V_o(x)}\Delta_o(p_o)x_{sp} \\ \dot{x}_{sp} = \dfrac{k_{sp}}{\tau}u_p - \dfrac{1}{\tau}x_{sp} \end{cases} \tag{6.3}$$

where

$$\Delta_i(p_i) = \begin{cases} \sqrt{\dfrac{2}{\rho}(p_s - p_i)} & x_{sp} \geq 0 \\ \sqrt{\dfrac{2}{\rho}(p_i - p_e)} & x_{sp} < 0 \end{cases}$$

and

$$\Delta_o(p_o) = \begin{cases} \sqrt{\dfrac{2}{\rho}(p_o - p_e)} & x_{sp} \geq 0 \\ \sqrt{\dfrac{2}{\rho}(p_s - p_o)} & x_{sp} < 0 \end{cases}$$

the term u_p in (6.3) is the position control signal

$$\frac{U_p}{-X + \bar{X}^d} = \frac{U_p}{-\bar{E}_1} = \frac{\bar{\lambda}_1 + \bar{\lambda}_2 s + \bar{\lambda}_3 s^2}{s(\bar{\alpha}_1 + \bar{\alpha}_2 s + s^2)}$$

which represents the position controller shown in Eq. (5.20). $\bar{x}^d$ is the desired position in free space and includes the prefilter action. The following state errors are now defined:

$$\bar{e}_1 = x - \bar{x}^d \qquad \bar{e}_2 = \dot{\bar{e}}_1$$

$$\bar{e}_3 = p_i - \bar{p}_i^d \qquad \bar{e}_4 = p_o - \bar{p}_o^d$$

$$e_5 = x_{sp} \qquad \bar{e}_6 = -\bar{\lambda}_1 \int (x - \bar{x}^d) dt = -\bar{\lambda}_1 \int \bar{e}_1 dt$$

$$\bar{e}_7 = -\bar{\lambda}_1 \int (x - \bar{x}^d) dt - \bar{\lambda}_2 (x - \bar{x}^d) - \bar{\alpha}_1 u_p \qquad \bar{e}_8 = u_p$$

where $\bar{p}_i^d$ and $\bar{p}_o^d$ are the line pressures pertaining to the desired position, $\bar{x}^d$. By substituting the above errors in (6.3), we arrive at the following state space model:

$$\dot{\bar{e}} = f_1(\bar{e}, t) = \begin{cases} \dot{\bar{e}}_1 = \bar{e}_2 \\ \dot{\bar{e}}_2 = \dfrac{A_i}{m}\bar{e}_3 - \dfrac{A_o}{m}\bar{e}_4 - \dfrac{d}{m}\bar{e}_2 \\ \dot{\bar{e}}_3 = -\dfrac{\beta A_i}{V_i(\bar{e}_1 + \bar{x}^d)}\bar{e}_2 + \dfrac{\beta c_d w}{V_i(\bar{e}_1 + \bar{x}^d)}\Delta_i(\bar{e}_3 + \bar{p}_i^d)e_5 \\ \dot{\bar{e}}_4 = \dfrac{\beta A_o}{V_o(\bar{e}_1 + \bar{x}^d)}\bar{e}_2 - \dfrac{\beta c_d w}{V_o(\bar{e}_1 + \bar{x}^d)}\Delta_o(\bar{e}_4 + \bar{p}_o^d)e_5 \\ \dot{e}_5 = \dfrac{k_{sp}}{\tau}\bar{e}_8 - \dfrac{1}{\tau}e_5 \\ \dot{\bar{e}}_6 = -\lambda_1 \bar{e}_1 \\ \dot{\bar{e}}_7 = \bar{e}_6 - \bar{\alpha}_1 \bar{e}_8 - \bar{\lambda}_2 \bar{e}_1 \\ \dot{\bar{e}}_8 = \bar{e}_7 - \bar{\alpha}_2 \bar{e}_8 - \bar{\lambda}_3 \bar{e}_1 \end{cases} \tag{6.4}$$

- **Contact State**

The differential equations during the contact state are:

$$\begin{cases} \ddot{x} = \dfrac{A_i}{m}p_i - \dfrac{A_o}{m}p_o - \dfrac{d}{m}\dot{x} - \dfrac{k_e}{m}x \\ \dot{p}_i = -\dfrac{\beta A_i}{V_i(x)}\dot{x} + \dfrac{\beta c_d w}{V_i(x)}\Delta_i(p_i)x_{sp} \\ \dot{p}_o = \dfrac{\beta A_o}{V_o(x)}\dot{x} - \dfrac{\beta c_d w}{V_o(x)}\Delta_o(p_o)x_{sp} \\ \dot{x}_{sp} = \dfrac{k_{sp}}{\tau}u - \dfrac{1}{\tau}x_{sp} \end{cases} \tag{6.5}$$

where

$$\Delta_i(p_i)=\begin{cases}\sqrt{\frac{2}{\rho}(p_s-p_i)} & x_{sp}\geq 0\\ \sqrt{\frac{2}{\rho}(p_i-p_e)} & x_{sp}<0\end{cases}$$

and

$$\Delta_o(p_o)=\begin{cases}\sqrt{\frac{2}{\rho}(p_o-p_e)} & x_{sp}\geq 0\\ \sqrt{\frac{2}{\rho}(p_s-p_o)} & x_{sp}<0\end{cases}$$

u in (6.5) is the force control signal

$$\frac{U}{-F+F^d}=\frac{U}{-k_eE_1}=\frac{\lambda_1+\lambda_2 s+\lambda_3 s^2}{s(\alpha_1+\alpha_2 s+s^2)}$$

which is actually the one shown in Eq. (4.54). f^d is the desired force during the contact phase. The following state errors are now defined

$$e_1=x-x^d\ \left(x^d=\frac{f^d}{k_e}\right) \qquad e_2=\dot{e}_1$$

$$e_3=p_i-p_i^d \qquad e_4=p_o-p_o^d$$

$$e_5=x_{sp} \qquad e_6=-\lambda_1 k_e\int(x-x^d)dt=-\lambda_1 k_e\int e_1 dt$$

$$e_7=-\lambda_1 k_e\int(x-x^d)dt-\lambda_2 k_e(x-x^d)-\alpha_1 u \qquad e_8=u$$

where p_i^d, p_o^d and x^d are the line pressures and desired position pertaining to the desired force, f^d, respectively. By substituting the above errors in (6.5), we arrive at the following state space model:

$$\dot{\boldsymbol{e}} = f_2(\boldsymbol{e},t) = \begin{cases} \dot{e}_1 = e_2 \\ \dot{e}_2 = \dfrac{A_i}{m}e_3 - \dfrac{A_o}{m}e_4 - \dfrac{d}{m}e_2 - \dfrac{k_e}{m}e_1 \\ \dot{e}_3 = -\dfrac{\beta A_i}{V_i(e_1 + x^d)}e_2 + \dfrac{\beta c_d w}{V_i(e_1 + x^d)}\Delta_i(e_3 + p_i^d)e_5 \\ \dot{e}_4 = \dfrac{\beta A_o}{V_o(e_1 + x^d)}e_2 - \dfrac{\beta c_d w}{V_o(e_1 + x^d)}\Delta_o(e_4 + p_o^d)e_5 \\ \dot{e}_5 = \dfrac{k_{sp}}{\tau}e_8 - \dfrac{1}{\tau}e_5 \\ \dot{e}_6 = -\lambda_1 k_e e_1 \\ \dot{e}_7 = e_6 - \alpha_1 e_8 - \lambda_2 k_e e_1 \\ \dot{e}_8 = e_7 - \alpha_2 e_8 - \lambda_3 k_e e_1 \end{cases} \tag{6.6}$$

- **Transition State**

The state space model for this phase is described based on (6.4) and (6.6) with respect to the state definition for contact state as follows:

$$\dot{\boldsymbol{e}} = f(\boldsymbol{e},t) = \begin{cases} f_1(\boldsymbol{e},t) & e_1 < x^* - x^d \quad \text{Non - Contact} \\ f_2(\boldsymbol{e},t) & e_1 \geq x^* - x^d \quad \text{Contact} \end{cases} \tag{6.7}$$

where x^* is the initial location of the environment with respect to the actuator. Note that the above state space equation, describing the whole system, is non-smooth due to the discontinuous control signal originating from the switching controller as stated by Eqs. (6.4) and (6.6).

6.2.2 Existence, Continuity and Uniqueness of Filippov's Solution

The dynamic systems presented by the state model (6.7) consists of nonlinear differential equations with discontinuous right-hand sides. The discontinuity occurs during the non-contact to contact transition phase due to the control law switching. These types of systems violate the fundamental assumption of conventional solution theories of

ordinary differential equations, known as the Lipschitz-continuous requirement. With respect to classical solution theories, one cannot even define a solution, much less discuss its existence, uniqueness and stability. Filippov has developed a solution concept for discontinuous differential equations, which was later used by many researchers for solution analysis of many engineering problems including non-smooth systems. For example, Paden and Sastry (1987) utilized Filippov's solution and proposed a variable structure controller for robot manipulators. Southward et al. (1991) developed a nonlinear friction compensator and employed Filippov's solution concept for their solution analysis. In this section, we prove the existence, uniqueness and continuity of Filippov's solution for the dynamic system under investigation.

The discontinuity surface is defined as

$$S := \{e : e_1 = x^* - x^d$$

S divides the solution region, Ω, into two parts as follows:

$$\Omega_s^+ := \{e : e_1 > x^* - x^d$$

$$\Omega_s^- := \{e : e_1 < x^* - x^d$$

Regarding the existence and continuity of Filippov's solution, the right hand side of (6.7) is piecewise continuous and defined everywhere in Ω. The conditions for existence and continuity of Filippov's solution, such as the right-hand sides of equations that are measurable and bounded, are both satisfied. Thus, the existence and continuity of the solution is guaranteed. Regarding the uniqueness of Filippov's solution (see Filippov,

1964), the limiting values of the vector function of the right-hand sides of (6.4) and (6.6), i.e., f^+ and f^-, when S is approached from Ω_s^+ and Ω_s^-, are given as

$$f^+ = \begin{Bmatrix} e_2 \\ \frac{A_i}{m}e_3 - \frac{A_o}{m}e_4 - \frac{d}{m}e_2 - \frac{k_e}{m}e_1 \\ -\frac{\beta A_i}{V_i(e_1+x^d)}e_2 + \frac{\beta c_d w}{V_i(e_1+x^d)}\Delta_i(e_3+p_i^d)e_5 \\ \frac{\beta A_o}{V_o(e_1+x^d)}e_2 - \frac{\beta c_d w}{V_o(e_1+x^d)}\Delta_o(e_4+p_o^d)e_5 \\ \frac{k_{sp}}{\tau}e_8 - \frac{1}{\tau}e_5 \\ -\lambda_1 k_e e_1 \\ e_6 - \alpha_1 e_8 - \lambda_2 k_e e_1 \\ e_7 - \alpha_2 e_8 - \lambda_3 k_e e_1 \end{Bmatrix}$$

$$f^- = \begin{Bmatrix} \bar{e}_2 \\ \frac{A_i}{m}\bar{e}_3 - \frac{A_o}{m}\bar{e}_4 - \frac{d}{m}\bar{e}_2 \\ -\frac{\beta A_i}{V_i(\bar{e}_1+\bar{x}^d)}\bar{e}_2 + \frac{\beta c_d w}{V_i(\bar{e}_1+\bar{x}^d)}\Delta_i(\bar{e}_3+\bar{p}_i^d)e_5 \\ \frac{\beta A_o}{V_o(\bar{e}_1+\bar{x}^d)}\bar{e}_2 - \frac{\beta c_d w}{V_o(\bar{e}_1+\bar{x}^d)}\Delta_o(\bar{e}_4+\bar{p}_o^d)e_5 \\ \frac{k_{sp}}{\tau}\bar{e}_8 - \frac{1}{\tau}e_5 \\ -\lambda_1 \bar{e}_1 \\ \bar{e}_6 - \bar{\alpha}_1 \bar{e}_8 - \bar{\lambda}_2 \bar{e}_1 \\ \bar{e}_7 - \bar{\alpha}_2 \bar{e}_8 - \bar{\lambda}_3 \bar{e}_1 \end{Bmatrix}$$

The projections of f^+ and f^- along the normal to the discontinuity surface, i.e., $N_s = \{1,0,0,0,0,0,0,0\}$, are denoted by f_N^+ and f_N^-:

$$f_N^+ = e_2 = \dot{x} - \dot{x}^d$$

$$f_N^- = \bar{e}_2 = \dot{x} - \dot{\bar{x}}^d$$

Assuming $\dot{x} > \dot{\bar{x}}^d$ on the discontinuity surface S, $f_N^- > 0$, and therefore, the uniqueness of Filippov's solution for the system described by (6.7) is guaranteed according to Theorem 14 of Filippov (Filippov, 1964). For the case $\dot{x} < \dot{\bar{x}}^d$, f_N^- becomes negative and Theorem 14 is not applicable. The uniqueness analysis for this case requires the utilization of other theorems and a heavier mathematical machinery and has not been conducted in this thesis.

6.2.3 Stability Proof

The stability analysis contains two major steps. The first step is based on the existence of Lyapunov functions for free space and constrained motion. The second step includes the construction of a Lyapunov function for the transition phase and the stability proof for this case.

- **Step 1:**

The asymptotic stability of equivalent models is satisfied during the design procedure by assigning the system's poles to the left hand side of the complex plane. The stability of the equivalent models can then be extended to the nonlinear system provided that the validity conditions of the theorem be satisfied (Horowitz, 1978; Banos and Bailey, 1996). These conditions set some restrictions on (*i*) the nonlinear system, such as the invertibility of the system, (*ii*) the acceptable set, and (*iii*) the equivalent models (e.g., having no unstable zeroes). These conditions are generally satisfied during the design procedure. However, the rigorous analysis of these conditions requires heavy mathematical machinery and is beyond the scope of this thesis.

Given the asymptotic stability of equivalent models, the asymptotic stability of the control system during the contact or non-contact phases with the prefilters and the QFT controllers is guaranteed. Therefore, based on the converse Lyapunov theorem (Slotine and Li, 1991, pp. 121), there exists a Lyapunov function V_p in free motion and a Lyapunov function V_f in constrained motion such that:

$$\dot{V}_p < 0$$

$$\dot{V}_f < 0$$

V_f and V_p will be used in the next step to construct a Lyapunov function for the transition phase.

• **Step 2:**

Here, the extension of Lyapunov's stability theory to non-smooth systems by Wu and Sepehri (2001) is used for stability analysis during the transition. This theory uses only extreme points of Clarke's generalized gradient (Clarke, 1983) to estimate the derivatives of a non-smooth Lyapunov function on the discontinuity surface. Based on the existence of Lyapunov functions V_f and V_p, the following positive-definite Lyapunov function candidate is constructed for stability proof:

$$V = \begin{cases} V_1 = V_p + \nu & e \in \Omega_S^- \\ V_2 = V_f & e \in \Omega_S^+ \\ V_3 = V_f & e \in S \end{cases} \tag{6.8}$$

V_3 is the Lyapunov function on the surface S. ν is chosen as the difference between the limit values of V_p and V_f as the state trajectory approaches S, i.e.,

$$\lim_{e \to S} V_1 = V_f \quad e \in \Omega_S^-$$

Note, V is continuous and positive definite in the whole solution region. Next, it is to be proven that the derivative of the above Lyapunov function is continuous and negative semi-definite in the regions that the system is smooth as well as on the discontinuity surface S.

The derivative of the Lyapunov function, when $e \notin S$, is

$$\dot{V} = \begin{cases} \dot{V}_1 = \dot{V}_p & e \in \Omega_S^- \\ \dot{V}_2 = \dot{V}_f & e \in \Omega_S^+ \end{cases} \tag{6.9}$$

where $\dot{V}$ is negative since $\dot{V}_p$ and $\dot{V}_f$ are negative as discussed in step 1. Built upon the approach proposed by Wu and Sepehri (2001), on the discontinuity surface, S, we have

$$\dot{V}(e \in S) = \dot{V}_3 \in \overline{co}[\dot{V}_1^*, \dot{V}_2^*] \tag{6.10}$$

where $\dot{V}_1^*$ and $\dot{V}_2^*$ are the limit values of $\dot{V}_1$ and $\dot{V}_2$ as the solution trajectory approaches S. Since $\dot{V}_1$ and $\dot{V}_2$ are never positive, in Ω_s^+ and Ω_s^-, respectively, we have,

$$\dot{V}_1^* = \lim_{e_1 \to (x^* - x^d)^-} \dot{V}_1 < 0$$

$$\dot{V}_2^* = \lim_{e_1 \to (x^* - x^d)^+} \dot{V}_2 < 0$$

The convex set, described in (6.10), contains only negative elements and $\dot{V}_3 = \dot{V}(e \in S)$ is negative. Therefore $\dot{V}$ is negative definite throughout the region that includes the discontinuity surface, S. Thus, following the extension by Wu and Sepehri (2001), the system is asymptotically stable when transition from non-contact to contact is involved.

6.3 Experimental Results

First, contact task control with an environment with a stiffness of 35 kN/m was examined. The task was to first bring the actuator from free space to contact with the environment and then exert a desired force of 1000 N. Fig. 6.2 shows the actuator stably establishing contact and the generated force reached to the desired value. The position of the actuator and the location of the environment is shown in Fig. 6.2b. Contact was established with an approach velocity of ~0.12 m/sec as shown in Fig. 6.2c where the actuator velocity dropped shortly after contact. Fig. 6.2d clearly shows how the controller switched to the force control law at the contact moment.

The above experiment was repeated with a higher stiffness (k_e=100 kN/m). The experimental results are depicted in Fig. 6.3. As expected, the control system established a stable contact with the environment despite increased environmental stiffness.

To investigate the controller's performance during different control phases, an experiment was conducted as outlined in Table 6.1. With reference to Table 6.1 and Fig. 6.4, the actuator was first commanded to reach a desired position, x^d=0.02 m, in free space. Once the desired position was achieved, the controller was set to bring the actuator to a new desired position at x^d=0.04 m. However, before the actuator reached to its second desired position, it hit the spring coil. The controller then switched to follow a set-point force (f^d =500 N). Next, the controller brought the contact force to a new set-point force level of 1000 N. Finally, the controller was commanded to unload the actuator (f^d =0 N) and bring it to the desired position x^d=0.02 m in free space.

In summary, in this Chapter, a QFT contact task controller was constructed and experimentally evaluated on the hydraulic actuator. The designed contact controller (i) is

capable of regulating a reference position and a reference force in free space and a constrained environment, respectively, (*ii*) is robust against uncertainties and nonlinearities present in hydraulic power systems, and (*iii*) guarantees stability, particularly during the transition phase.

Table 6.1: Controller set-point adjustment in a multi-step contact response test.

Step	Time (sec)	Desired Position (m)	Desired Force (N)	Type of Control
1	0-4	0.02	-	Position
2	4-8	0.04	500	Transition
3	8-12	-	1000	Force
4	12-16	0.02	0	Transition

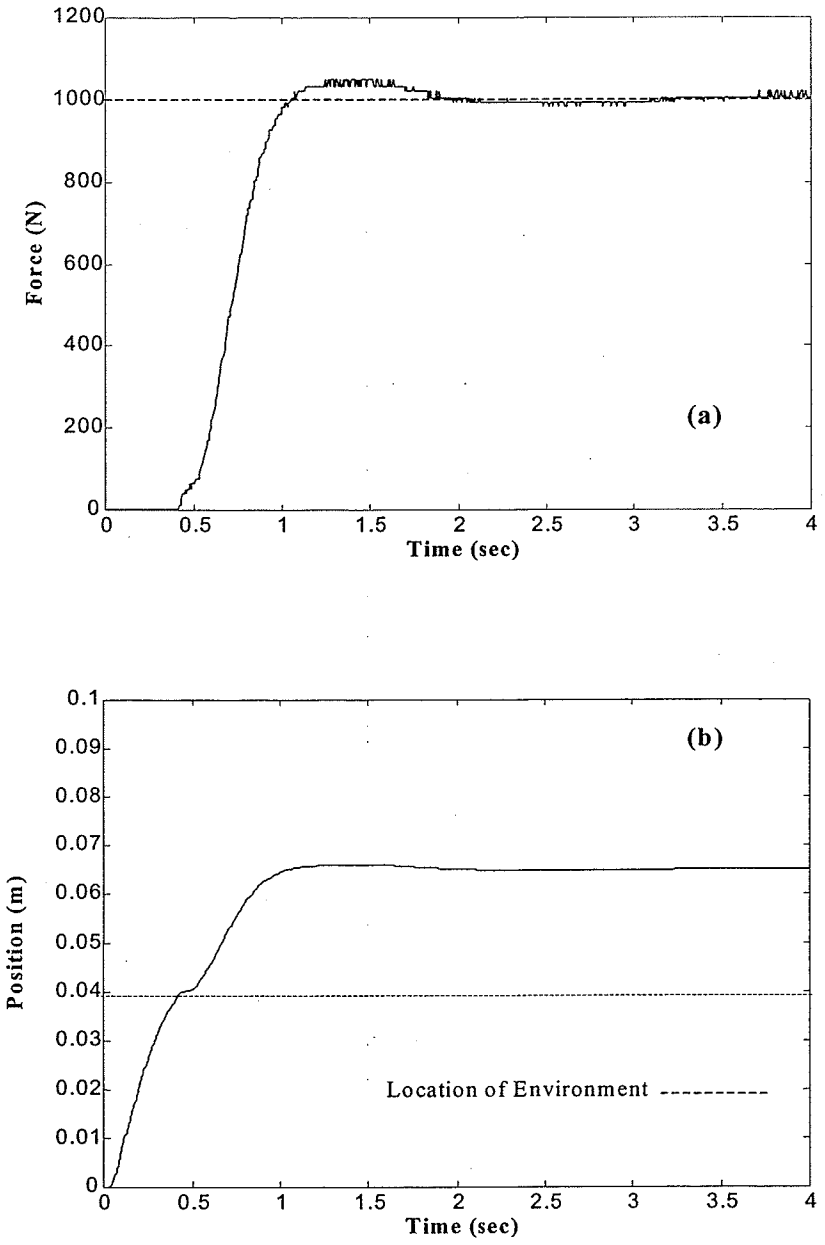

Fig. 6.2: Contact response: **(a)** force; **(b)** position; **(c)** velocity; **(d)** control signal.

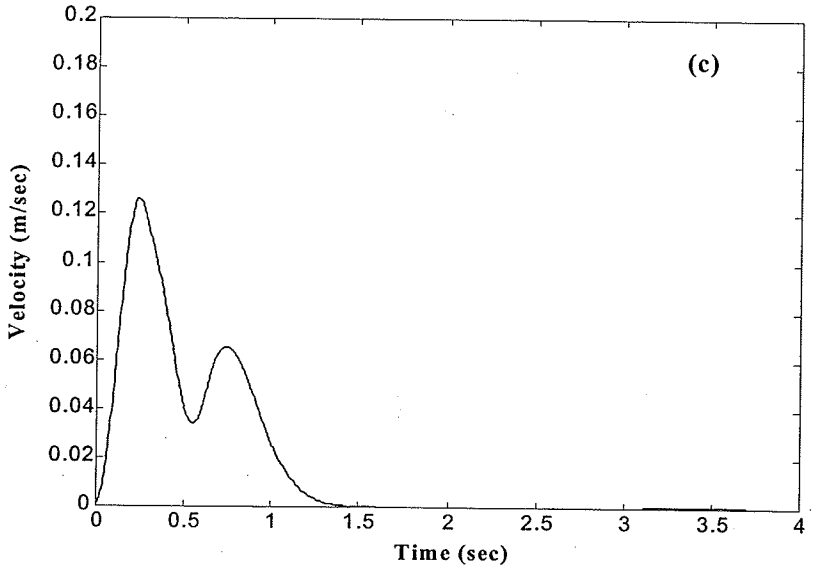

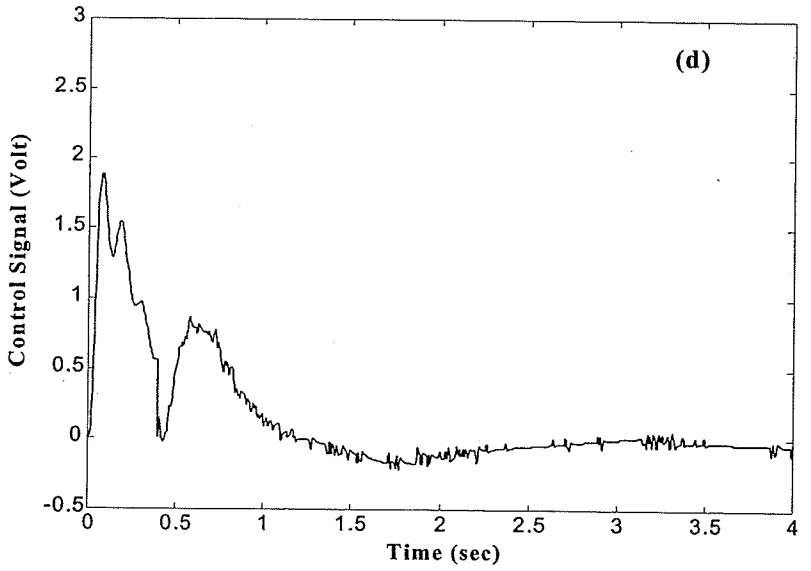

Fig. 6.2: (Continued).

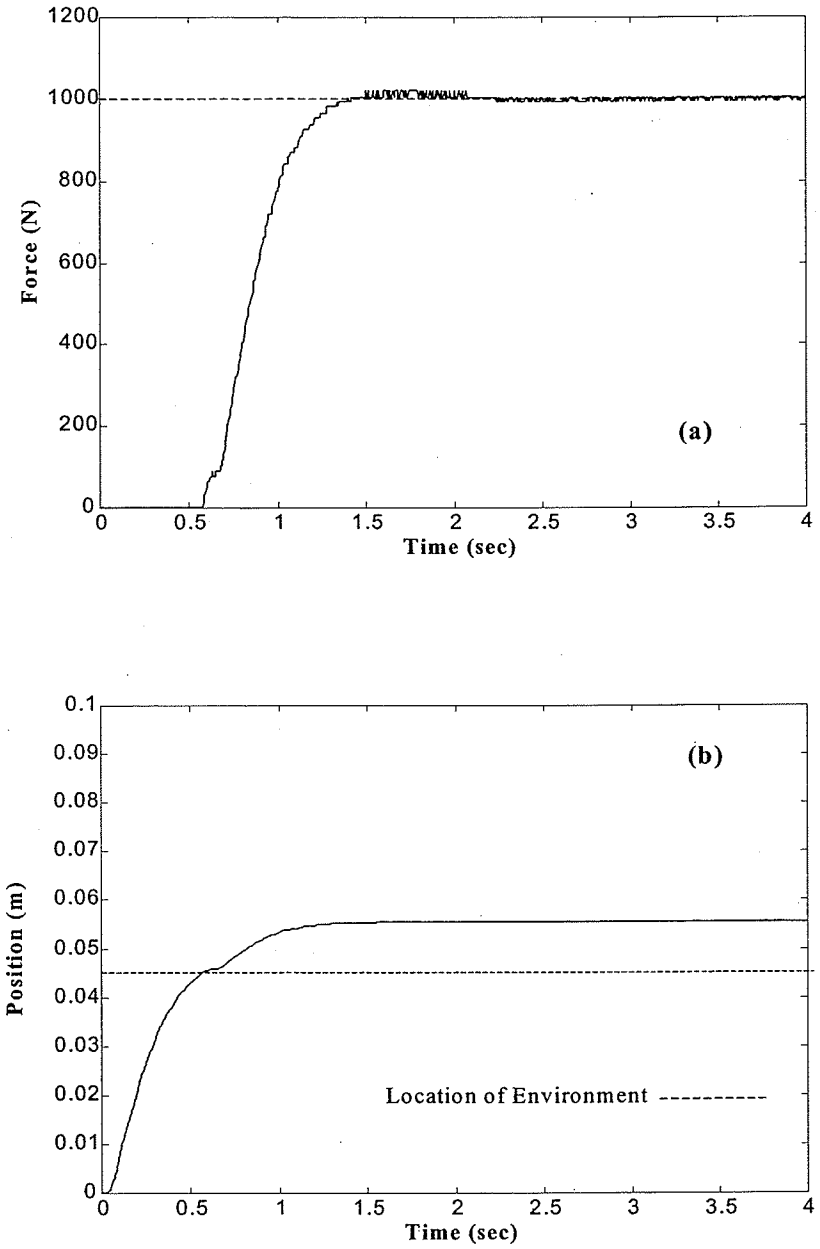

Fig. 6.3: Contact response (high stiffness): **(a)** force; **(b)** position.

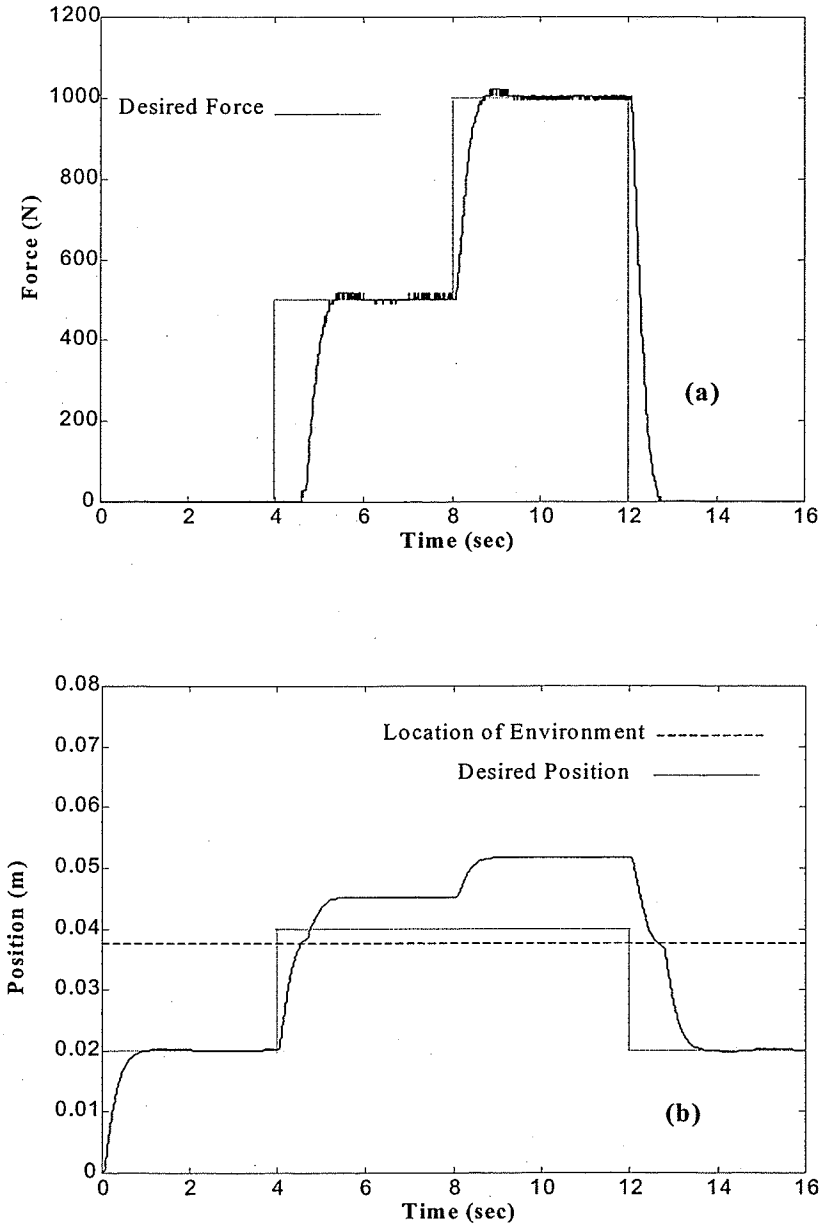

Fig. 6.4: Multi-step contact response test: **(a)** force; **(b)** position.

Chapter 7

Concluding Remarks

This thesis has made an important contribution to the development of stable and robust controllers for hydraulic actuators. In doing this, it investigated, formulated, analyzed, developed, implemented, and experimentally evaluated appropriate control strategies that are suitable for motion tasks, forcing tasks, and contact tasks of hydraulic actuators in a practical setting. In the following the detailed contributions are given. Firstly, a linear parametrically uncertain model was constructed to represent the relation between the control signal and the force acting on the environment. Plant uncertainty was quantified within the linear model to compensate for time-varying dynamics and to allow for variations in environmental stiffness, hydraulic fluid flow and pressure gains, actuator compliance and many other parameters specific to hydraulic components. A robust controller was then designed which, along with a prefilter, maintained a satisfactory force control performance against the environment in spite of the wide range of uncertainties.

A knowledge of the lower and upper bounds of uncertain parameters was the only requirement for the controller design.

The nonlinear approach within the framework of QFT was employed next to design a controller for the nonlinear system under investigation. The design methodology proceeded with the generation of linear time-invariant equivalent models using two methods. The first method was based on experimental input-output measurement of acceptable system responses. Generally, this method is applicable to plants for which no analytical model is available. In the second method, the general nonlinear mathematical model was used for derivation of input-output histories. For this purpose, a numerical algorithm was developed in this study for derivation of the equivalent model. Many plant nonlinearities including valve flow-pressure characteristics, valve opening areas and variations in the trapped fluid volume as well as plant uncertainties such as pump pressure and environmental stiffness were explicitly included in the model. The extension method by Golubev and Horowitz (1982) was employed to determine the family of equivalent linear transfer functions. There was a strong correlation between the results of the two methods, indicating that the mathematical model developed here could accurately represent the system under investigation.

The designed controllers were then implemented successfully on the test stand and several tests were performed under different conditions including: variations of up to 300% in environmental stiffness, 100% in supply pressure and 100% in reference force. The experimental results demonstrated the robustness of the QFT controller to real parameter variations and good performance in spite of significant actuator dynamics. The controllers were of low-order and easy to implement, required very little computational

effort, did not need any on-line tuning or gain scheduling and resulted in responses with good performance in both transient and steady-state periods. Also, the controllers incorporated only measured contact force as feedback, which makes them attractive for industrial implementation. These characteristics make the application of the developed QFT controllers appealing as compared to other existing controllers which involve complex control laws, high order compensators, and/or specific requirements such as precise knowledge of system parameters. Furthermore, until today, to the best of author's knowledge, there is no research aimed at the design of a controller that simultaneously deals with large variation of hydraulic systems properties including environmental stiffness, supply pressure and set-point forces.

The evaluation of control design procedures within the QFT framework was also presented. The linear approach needs less calculation effort and can be easily employed with only some knowledge about the system parameters. The nonlinear approach seems more suitable to apply to the solution of inherently nonlinear problems. Hence, in the nonlinear approach many of the nonlinear aspects of the hydraulic actuator can explicitly be incorporated. Within the nonlinear approach framework, the experimental method is attractive for controller synthesis of complex hydraulic systems in which the derivation of mathematical models is difficult and/or time consuming. Moreover, in this work, the nonlinear QFT approach and Golubev's method were experimentally evaluated on a real industrial problem, which has rarely been reported in the literature.

Based on the nonlinear approach, an explicit position control law was also developed to regulate the actuator in free space. Similar to the QFT force control design, a numerical algorithm was first developed for derivation of the input control signals given

plant outputs during free space motion. The input-output data set obtained from the numerical algorithm was then used within Golubev's method to derive the equivalent time-invariant plant models.

Next, both position and force controllers were used to construct a switching contact controller based on the measured force. The drawback of the proposed switching controller is the existence of discontinuity in the inevitable phase transition when the actuator moves from free space to the constrained environment. The discontinuity causes the dynamic system under investigation to be non-smooth, which violates the requirement of conventional solution theories to ordinary differential equations. Therefore, in this study, the stability of the non-smooth control system is proven by defining a smooth Lyapunov function under the condition of existence and uniqueness of Fillipov's solution.

Implementation of the proposed contact task control law is simple and no knowledge about the location of the environment is required in determining the control signal. The controller was implemented on the test station and different contact scenarios were tested. Experimental results showed that the controller is capable of presenting satisfactory performance during non-contact, contact and transition phases.

The focus of the future work could be placed on the following subjects. Firstly, in this study the environment has been treated as a pure stiffness. This model is accurate enough for the force control and contact task control in many practical situations. However, there exist applications in which a simple spring cannot represent the environment properly. Utilization of a more sophisticated model of the environment, which could accurately represent the contact dynamics, is suggested for the future work. Secondly, in this thesis,

the stability of the position and force controllers has been assumed to exist based on QFT method. A more rigorous method should be developed to address the stability of the contact controller, by taking into account the dynamics of the hydraulic actuator and the environment.

References

Alleyne A., 1996, "Nonlinear Force Control of an Electro-Hydraulic Actuator," *Proc. Japan/USA Symposium on Flexible Automation*, Boston, MA, pp.193-200.

Banos, A., and F.N. Bailey, 1996, "Linear Control of Uncertain Nonlinear Plants," *A post print Volume from the 3rd IFAC Symposium,* **2**, pp. 813-818.

Bentley, A. E., 1992, "Arc Welding Penetration Control Using Quantitative Feedback Theory," *Proc. First QFT Symposium,* Wright-Patterson Air Force Base, OH, pp. 212-263.

Chen, Y.N., C.B. Lee, and C.H. Tseng, 1990, "A Variable-Structure Controller Design for an Electro-Hydraulic Force Control Servo System," *Journal of the Chinese Society of Mechanical Engineers,* **11**, pp. 520-526.

Chin, S.M, C.O. Lee, and P.H. Chang, 1994, "An Experimental Study on the Position Control of an Electro-Hydraulic Servo System Using Time Delay Control," *Control Engineering Practice*, **2**, pp.41-48.

Clarke, F. H., 1983, *Optimization and Nonsmooth Analysis*, John Wiley and Sons, NY.

Conrad, F., and C.J.D. Jensen, 1987, "Design of Hydraulic Force Control Systems with State Estimate Feedback," *Proc. IFAC 10th Triennial Congress*, Munich, FRG, pp. 307-312.

D'Azzo, J.J., and C.H. Houpis, 1995, *Linear Control System Analysis and Design*, McGraw-Hill, NY.

Eykhoff, P., 1973, *Identification and system parameter Estimation*, American Elsevier, NY.

Filippov, A.F., 1964, "Differential Equations with Discontinuous Right Hand Side," *American Mathematical Society Transactions*, **42**, pp. 199-231.

Filippov, A.F., 1979, "Differential Equations with Second Members Discontinuous on Intersecting Surfaces," *Differential'nye Uravneniya*, **15**, pp. 1814-1832.

FitzSimons, P.M., and J.J. Palazzolo, 1996, "Modeling of a One-Degree-of-Freedom Active Hydraulic Mount," *ASME Journal of Dynamic Systems, Measurement, and Control*, **118**, pp. 439-448.

Golubev, B., and I.M. Horowitz, 1982, "Plant Rational Transfer Function Approximation from Input-Output Data," *Int. Journal of Control*, **36**, pp. 711-723.

Graupe, D., 1972, *Identification of systems*, Krienger, Melbourn, FL.

Heinrichs, B., N. Sepehri, and A.B. Thornton-Trump, 1997, "Position-Based Impedance Control of an Industrial Hydraulic Manipulator," *IEEE Control Systems Magazine,* **17**, pp. 46-52.

Hogan, N., 1987, "Stable Execution of Contact Tasks Using Impedance Control," *Proc. IEEE Conference on Robotics and Automation,* Raleigh, NC, pp. 1047-1054.

Horowitz, I.M., 1976, "Synthesis of Feedback Systems with Nonlinear Time-Varying Plants to satisfy Quantitative Performance Specifications," *Proc. IEEE*, **64**, pp. 123-130.

Horowitz, I.M., 1992, *Quantitative Feedback Theory*, QFT Publication, Boulder, CO.

Laval, L., N.K. M'Sirdi, and J. Cadiou, 1996, "H_∞ Force Control of a Hydraulic Servo-Actuator with Environmental Uncertainties," *Proc. IEEE Conference on Robotics and Automation*, Minneapolis, MN, pp. 1566-1571.

Liu, R., and A. Alleyne, 1999, "Nonlinear Force/Pressure Tracking of an Electro-Hydraulic Actuator," *Proc. IFAC 14th Triennial Congress*, Beijing, China, pp. 469-474.

Marth, G., T.J. Tran, and A.K. Bejczy, 1993, "Stable Phase Transition Control for Robot Arm Motion," *Proc. IEEE Conference on Robotics and Automation*, pp. 1566-1571.

Mason, M., 1981, "Compliance and Force Control for Computer Controlled Manipulator," *IEEE Transaction on Systems, Man, and Cybernetics*, **11**, pp. 418-432.

Merritt, H.E., 1967, *Hydraulic Control Systems*, John Wiley and Sons, NY.

Miller, R. B., I.M. Horowitz, C.H. Houpis, and F. Barfield, 1992, "Multi-Input Multi-Output Flight Control System Design for The YF-16 Using Nonlinear QFT and Pilot Compensation," *Proc. First QFT Symposium,* Wright-Patterson Air Force Base, OH, pp. 178-189.

Mills, J., and D. Lokhorst, 1993, "Control of Robotic Manipulators During General Task Execution: A Discontinuous Control Approach," *Int. Journal of Robotics Research*, **12**, pp. 146-163.

Niksefat, N., N. Sepehri, and K. Ziaie, 1999, "Design of a Force Controller for a Hydraulic Actuator in Contact with an Uncertain Environment via Quantitative Feedback Theory," *14th World Congress of IFAC*, Beijing, China, pp. 91-96.

Niksefat, N., and N. Sepehri, 1999a, "Robust Force Controller Design for a Hydraulic Actuator Based on Experimental Input-Output Data," *Proc. American Control Conference,* San Diego, CA, pp. 3718-3722.

Niksefat, N., and N. Sepehri, 1999b, "Robust Force Controller Design for an Electro-Hydraulic Actuator Based on Nonlinear Model," *Proc. IEEE Conference on Robotics and Automation*, Detroit, MI, pp. 200-206.

Niksefat, N., and N. Sepehri, 2000a, "Design and Experimental Evaluation of a Robust Force Controller for an Electro-Hydraulic Actuator via Quantitative Feedback Theory," *IFAC Journal of Control Engineering Practice*, **8**, pp. 1335-1345.

Niksefat, N., Q. Wu, and N. Sepehri, 2000b, "Stable Control of an Electro-Hydraulic Actuator during Contact Tasks: Theory and Experiments," *Proc. American Control Conference*, Chicago, pp. 4114-4118.

Niksefat, N., and N. Sepehri, 2001a, "Robust Force Control of Hydraulic Actuator in spite of System and Environmental Uncertainties," *IEEE Control Systems Magazine,* **21**, pp 66-77.

Niksefat, N., and N. Sepehri, 2001b, "Design of a Lyapunov Controller for an Electro-Hydraulic Actuator During Contact Task," *ASME Journal of Dynamic Systems, Measurement, and Control*, **123**, pp. 299-307.

Pachter, M., C.H. Houpis, and K. Kang, 1997, "Modeling and Control of an Electro-hydrostatic Actuator," *Int. Journal of Robust and Nonlinear Control*, **7**, pp. 591-608.

Paden, B.E., and S.S. Sastry, 1987, "A Calculus for Computing Filippov's Differential Inclusion with Application to the Variable Structure Control of Robot Manipulators," *IEEE Transaction on Circuits and Systems* **34**, pp. 73-82.

Pannett, R.F., P.K. Chawdhry, and C.R. Burrows, 1999, "Alternative Robust Control Strategies for Disturbance Rejection in Fluid Power Systems," *Proc. ACC Conference,* San Diego, CA, pp. 739-743.

Payandeh, S., 1996, "A Method for Controlling Robotic Contact Tasks," *Robotica* **14**, pp. 281-288.

Seraji, H., and R. Colbaugh, 1997, "Force Tracking in Impedance Control," *Int. Journal of Robotics Research* **16**, pp. 97-117.

Slotine, E., and W. Li, 1991, *Applied Nonlinear Control*, Prentice Hall, NJ.

Southward, S.C., C.J. Radcliffe, and C.R. MacCluer, 1991, "Robust Nonlinear Stick-Slip Friction Compensation," *Journal of Dynamics Systems, Measurement, and Control*, **113**, pp. 639-645.

Sun, H., and G.T.C. Chiu, 1999, "Nonlinear Observer Based Force Control of Electro-Hydraulic Actuators," *Proc. ACC Conference,* San Diego, CA, pp. 764-768.

Thompson, D.F., and G.G. Kremer, 1997, "Quantitative Feedback Design for a Variable-Displacement Hydraulic Vane Pump," *Proc. ACC Conference,* Albuquerque, NM, pp. 1061-1064.

Volpe, R., and P. Khosla, 1990, "Theoretical Analysis and Experimental Verification of a Manipulators/Sensor/Environment Model for Force Control," *Proc. IEEE Conf. Systems, Man, Cybernetics,* Los Angles, CA, pp. 784-790.

Volpe, R., and P. Khosla, 1993, "A Theoretical and Experimental Investigation of Impact Control for Manipulators," *Int. Journal of Robotics Research* **12**, pp. 351-365.

Vossoughi, R., and M. Donath, 1995, "Dynamic Feedback Linearization for Electrohydraulically Actuated Control Systems," *ASME Journal of Dynamic Systems, Measurement, and Control*, **117**, pp. 468-477.

Watton, J., 1989, *Fluid Power Systems-Modeling, Simulation, and Microcomputer Control,* Prentice-Hall, NJ.

Watton, J., 1990, "On Linearized Coefficients for an Underlapped Servo-Valve Coupled to a Single-rod Cylinder," *ASME Journal of Dynamic Systems, Measurement, and Control* **112**, pp. 794-796.

Wu, G., N. Sepehri, and K. Ziaei, 1998, "Design of a Hydraulic Force Motion Control system Using a Generalized Predictive Control Algorithm," *IEE Proc. on Control Theory and Applications*, **145**, pp. 428-436.

Wu, Q., and N. Sepehri, 2001, "On Lyapunov's Stability Analysis of Non-Smooth Systems with Application to Control Engineering," *Int. Journal of Nonlinear Mechanics,* **36**, pp. 1153-1161.

Wu, Y., T.J. Tran, N. Xi, and A. Isidori, 1996, "On Robust Control via Positive Acceleration Feedback for Robot Manipulators," *Int. Conference on Robotics and Automation*, Minneapolis, MN, pp. 1891-1896.

Yaniv, O., 1999, *Quantitative Feedback Design of Linear and Nonlinear Control Systems*, Kluwer Norwell, MA.

Yao, B., F. Bu, J. Reedy, and G. Chiu, 1999, "Adaptive Robust Control of Single-Rod Hydraulic Actuators: Theory and Experiments," *Proc. American Control Conference,* San Diego, CA, pp. 759-763.

Yu, J., Z. Chen, and Y. Lu, 1994, "The Variation of Oil Effective Bulk Modulus with Pressure in Hydraulic Systems," *ASME Journal of Dynamic Systems, Measurement, and Control*, **116**, pp. 146-150.

Ziaei, K., and N. Sepehri, 2001, "Design of a Nonlinear Adaptive Control Scheme for the Hydraulic Actuators," *ASME Journal of Dynamic Systems, Measurement, and Control*, Sep 2001.